② LEVEL II

AFWAL-TR-81-1066

PROPERTIES OF HIGH-EFFICIENCY X-BAND IMPATT DIODES

R. K./Mains
G. I./Haddad

Electron Physics Laboratory
Department of Electrical and Computer Engineering
The University of Michigan
Ann Arbor, Michigan 48109

Jun 81

128

TR-147

Interim Report. Sep 79-Jan 81

F33615-77-C-1132

2002

03

DTIC
SELECTED
NOV 6 1981
B

81 10 21

125900

NOTICE

When Government drawings, specifications, or other data are used for any purpose other than in connection with a definitely related Government procurement operation, the United States Government thereby incurs no responsibility nor any obligation whatsoever; and the fact that the government may have formulated, furnished, or in any way supplied the said drawings, specifications, or other data, is not to be regarded by implication or otherwise as in any manner licensing the holder or any other person or corporation, or conveying any rights or permission to manufacture use, or sell any patented invention that may in any way be related thereto.

This report has been reviewed by the Office of Public Affairs (ASD/PA) and is releasable to the National Technical Information Service (NTIS). At NTIS, it will be available to the general public, including foreign nations.

This technical report has been reviewed and is approved for publication.

JON E. GRIGUS, CAPT, USAF
Project Engineer
Microwave Techniques &
   Applications Gp

ALAN R MERTZ, CAPT, USAF
Chief, Microwave Techniques &
   Applications Gp
Avionics Laboratory

FOR THE COMMANDER

DONALD S. REES, Chief
Microwave Technology Branch
Avionics Laboratory

REPORT DOCUMENTATION PAGE		READ INSTRUCTIONS BEFORE COMPLETING FORM
1. REPORT NUMBER AFWAL-TR-81-1066	2. GOVT ACCESSION NO. AD-A107 043	3. RECIPIENT'S CATALOG NUMBER
4. TITLE (and Subtitle) *X-BAND* PROPERTIES OF HIGH-EFFICIENCY GaAs IMPATT DIODES		5. TYPE OF REPORT & PERIOD COVERED Interim Technical September 1979–January 1981
		6. PERFORMING ORG. REPORT NUMBER Technical Report No. 147
7. AUTHOR(s) R. K. Mains and G. I. Haddad		8. CONTRACT OR GRANT NUMBER(s) F33615-77-C-1132
9. PERFORMING ORGANIZATION NAME AND ADDRESS Electron Physics Laboratory The University of Michigan Ann Arbor, MI 48109		10. PROGRAM ELEMENT, PROJECT, TASK AREA & WORK UNIT NUMBERS 20020351
11. CONTROLLING OFFICE NAME AND ADDRESS Avionics Laboratory (AFWAL/AADM-2) Air Force Wright Aeronautical Laboratories, AFSC Wright-Patterson Air Force Base, OH 45433		12. REPORT DATE June 1981
		13. NUMBER OF PAGES 127
14. MONITORING AGENCY NAME & ADDRESS(if different from Controlling Office)		15. SECURITY CLASS. (of this report) Unclassified
		15a. DECLASSIFICATION/DOWNGRADING SCHEDULE N/A

16. DISTRIBUTION STATEMENT (of this Report)

Approved for public release; distribution unlimited.

17. DISTRIBUTION STATEMENT (of the abstract entered in Block 20, if different from Report)

18. SUPPLEMENTARY NOTES

The findings in this report are not to be construed as an official Department of the Air Force position, unless so designated by other authorized comments.

19. KEY WORDS (Continue on reverse side if necessary and identify by block number)

High-efficiency X-band GaAs IMPATT diodes
Single- and double-drift structures
Finite-difference program
Large-signal results

20. ABSTRACT (Continue on reverse side if necessary and identify by block number)

Several different IMPATT diode structures operating in the precollection mode at X-band (9 to 11 GHz) are examined, both using a complete finite-difference program and a simplified analysis which is developed in the report. The details of the precollection mode are examined, and large-signal solutions are presented for each different structure. Both single- and double-drift diodes are considered. Dynamic temperature effects are included and the differences between simulations at constant temperature and those with variable temperature are noted.

DD FORM 1473
1 JAN 73

-i-/-ii-

FOREWORD

TABLE OF CONTENTS

LIST OF ILLUSTRATIONS

LIST OF TABLES

1. Introduction

This report examines the operation of high-efficiency, single- and double-drift GaAs IMPATT diodes. The mechanisms responsible for high efficiency in these devices have already been identified and include depletion-layer width modulation,[1] premature collection of the generated electron pulse,[2] and movement of electrons at velocities higher than the saturated velocity during a portion of the RF cycle.[3] Theoretical analyses of one-sided, high-efficiency GaAs diodes using finite-difference numerical algorithms have been published.[4] Also, theoretical analyses of double-drift GaAs diodes were performed,[5] however, the restrictive assumption was made that the doping profile on the n-side for an optimized double-drift structure is the same as for an optimized single-drift structure. No results have been published which present detailed simulations of the various high-efficiency double-drift structures and which show the effects of depletion-layer width modulation and precollection on efficiency enhancement in these structures.

To simulate these diodes, both simplified analyses and the finite-difference program developed by Bauhahn and Haddad[4] are used in this report. By simulating many different structures for different RF drives and current densities, optimization criteria are developed for GaAs diodes operating near 10 GHz.

The simplified analyses presented here provide an inexpensive method of predicting the large-signal performance of the diodes which

1

agrees well with results of the finite-difference simulation, as far
as frequency of operation and voltage modulation levels are concerned.
The finite-difference program[4] uses explicit upwind drift and implicit
diffusion current terms. It includes the variation of the following
parameters with electric field: electron and hole velocities, electron
diffusion coefficient, and electron and hole ionization rates.
Tunneling was not included in these simulations and is not considered
to be important for the structures considered here. The generation
term is explicit in the program. The boundary conditions are Dirichlet
for the majority carrier, and for the minority carrier the boundary
condition is either Dirichlet or a mixed boundary condition which
ensures that the total current (drift plus diffusion) is constant at
the boundary and equal to a specified reverse saturation current.
However, even when the mixed boundary condition is selected, the
minority boundary condition becomes Dirichlet if the electric field
becomes negative at the boundary; in that case the boundary concentra-
tion retains the value that was set when the electric field was last
positive, until the boundary field becomes positive again.

As is explained in Reference 4, the program employs a "staggered"
mesh with two kinds of mesh points, space-charge points, and field
points. This formulation has the advantage that the finite-difference
equations are conservative under electric field reversal.

The material parameters used for GaAs at 300°K and 500°K[4,6] are
listed in Table 1. The properties of the following GaAs IMPATT
structures are presented in the following order: uniformly doped
single-drift, single-drift high-low and low-high-low diodes,
uniformly doped double-drift structures, hybrid double-drift sturctures,

Table 1

GaAs Material Parameters

$$v_n(E) = \frac{\mu_n |E| + v_{nsat}\left(\frac{E}{E_v}\right)^4}{1 + \left(\frac{E}{E_v}\right)^4}$$

$$v_p(E) = v_{psat}[1 - \exp(-\mu_p|E|/v_{psat})]$$

$$D_n(E) = \frac{D_{no} + D_{nsat}\left(\frac{E}{E_d}\right)^4}{1 + \left(\frac{E}{E_d}\right)^4}$$

$$D_p(E) = 20 \text{ cm}^2/\text{s}$$

$$\alpha_n(E) = \alpha_p(E) = A \exp[-(b/E)^2]$$

T ($^\circ$K)	μ_n $\left(\frac{cm^2}{V\text{-}s}\right)$	v_{nsat} (cm/s)	E_v (V/cm)	v_{psat} (cm/s)	μ_p $\left(\frac{cm^2}{V\text{-}s}\right)$	D_{nsat} (cm^2/s)	E_d (V/cm)
300	5000	8×10^6	3.5×10^3	10^7	400	20	4.5×10^3
500	4000	5×10^6	4.0×10^3	6.5×10^6	200	20	5.8×10^3

T ($^\circ$K)	A (cm^{-1})	b (V/cm)	D_{no} (cm^2/s)
300	2.0×10^5	5.5×10^5	187
500	2.3×10^5	6.9×10^5	217

-3-

and double-Read double-drift diodes (high-low doping profile on both sides of the junction).

2. Approximate Analysis

Approximate methods for analyzing high-efficiency GaAs IMPATT diodes are desirable, especially since the cost per solution of the finite-difference large-signal program can be significant (as much as $10 for double-drift, nonpunch-through structures). The simplified analysis is typically used to determine approximately the optimum RF drive for operation of a particular structure at a particular frequency; then large-signal runs are made and the parameters adjusted until optimum operation is obtained. The simplified analysis could also be used to determine the optimum frequency, given a particular structure and the RF voltage amplitude.

In the simplified analysis, the electric field profile is assumed to be piecewise linear. The initial field profile is determined by running the finite-difference dc program. Figures 1 and 2 show the field profiles included in the analysis. These profiles are appropriate for the hybrid double-drift case with uniform doping on the p-side and high-low doping on the n-side. However, by making the slope of the segment from $x = 0$ to $x = w_{ns}$ equal to the slope from $x = w_{ns}$ to $x = w_n$, it is seen that the analysis can be used for structures with uniform doping on both sides. Also, by making w_p very small, the analysis is applicable to one-sided, high-low or uniformly doped structures.

In the approximate analysis, it is assumed that the field profile moves up and down, but that it retains piecewise linearity as the terminal voltage is changed. Thus dynamic space-charge effects are
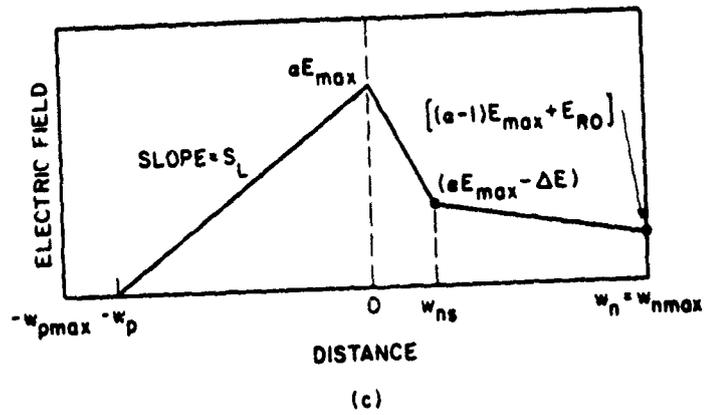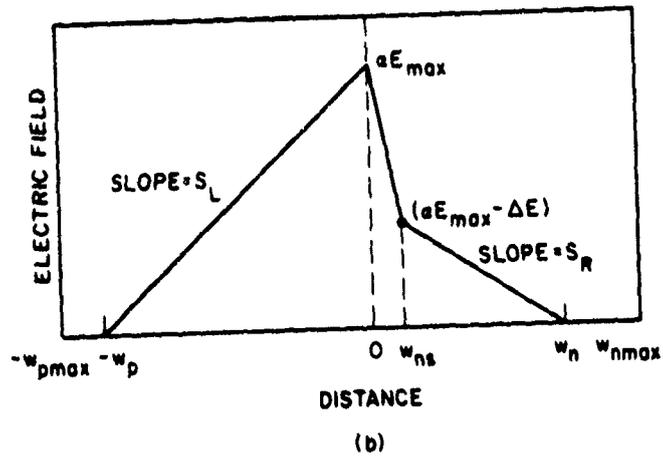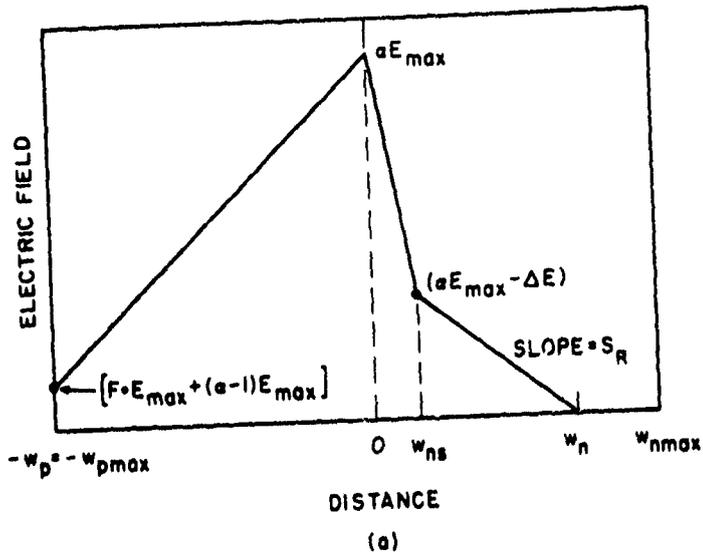
FIG. 1 ELECTRIC FIELD PROFILES INCLUDED IN THE APPROXIMATE ANALYSIS.
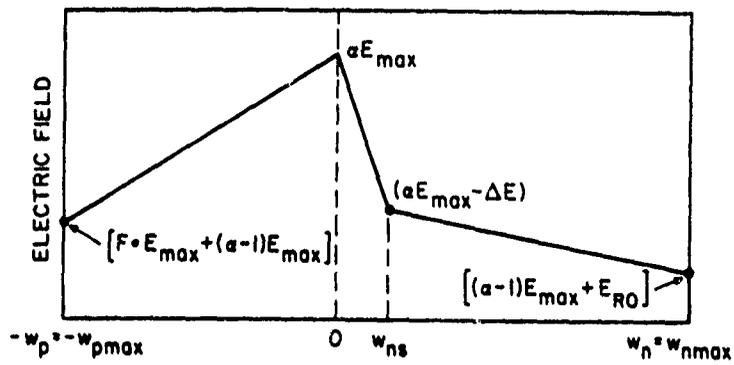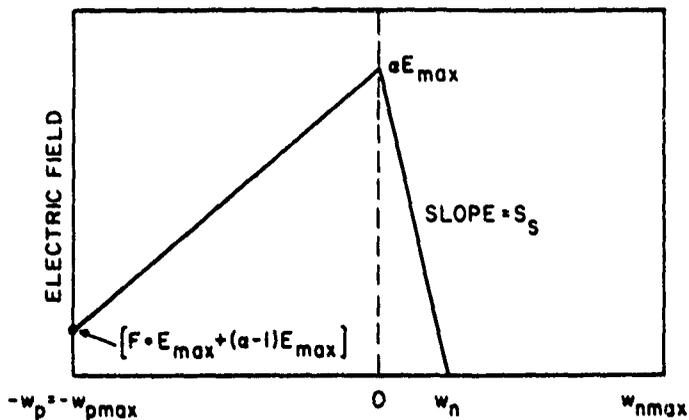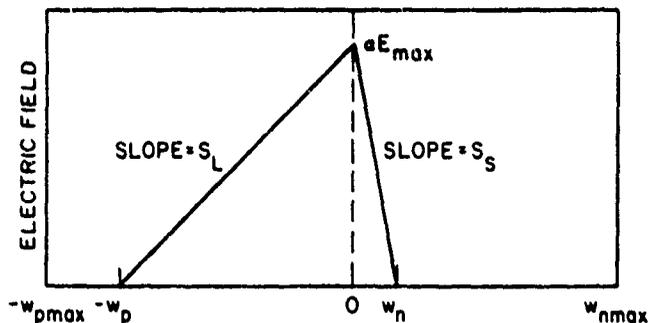
FIG. 2 ELECTRIC FIELD PROFILES INCLUDED IN THE APPROXIMATE ANALYSIS.

ignored (dc space-charge effects are of course included in the determination of the dc field profile). The terminal voltage is given by

$$V(t) = V_{dc} + V_{RF} \sin (\omega t + \pi) \quad , \qquad (1)$$

where $t = 0$ corresponds to the half-cycle point. At $t = 0$, an electron appears at some location $x_n(t = 0) > 0$ and a hole appears at $x_p(t = 0) < 0$. (These positions are found from previous runs of the complete finite-difference program, where the positions of the generated pulse maxima at half-cycle were determined.) At $t = 0$ the peak field is E_{max}, or $\alpha = 1$ in Figs. 1 and 2. Therefore the velocities of the electron and hole at $x_n(0)$ and $x_p(0)$ can be found using the expressions in Table 1 since the electric field is known. The particles are next advanced to new positions according to:

$$\left. \begin{array}{l} x_n(\Delta t) = x_n(0) + v_n(E_n)\Delta t \\ x_p(\Delta t) = x_p(0) + v_p(E_p)\Delta t \end{array} \right\} \quad , \qquad (2)$$

where the time step Δt is a small fraction of the cycle period and E_n, E_p are, respectively, the fields at the electron and hole positions.

At $t = \Delta t$, a new terminal voltage is evaluated from Eq. 1. Then the value of α must be found such that the integral of the field profile equals $V(t)$. The equations that yield α for the profiles of Figs. 1 and 2 are:

For Fig. 1a

$$\alpha^2 \left(\frac{E_{max}^2}{2S} \right) + \alpha \left((w_p + w_{ns})E_{max} - \frac{\Delta E}{S} E_{max} \right) + \left(\frac{w_p E_{max}}{2} (F - 1) \right.$$

$$\left. - \frac{\Delta E w_{ns}}{2} + \frac{\Delta E^2}{2S} - V(t) \right) = 0 \quad . \quad (3)$$

For Fig. 1b

$$\alpha^2 \left(\frac{E_{max}^2}{2S_L} + \frac{E_{max}^2}{2S_R} \right) + \alpha \left(w_{ns} E_{max} - \frac{\Delta E \cdot E_{max}}{S_R} \right) + \left(\frac{\Delta E^2}{2S_R} - \frac{w_{ns} \Delta E}{2} - V(t) \right) = 0 \quad .$$

$$(4)$$

For Fig. 1c

$$\alpha^2 \left(\frac{E_{max}^2}{2S_L} \right) + \alpha(w_n E_{max}) + \left(\frac{E_{Ro}}{2} (w_n - w_{ns}) - \frac{E_{max}}{2} (w_n - w_{ns}) \right.$$

$$\left. - \frac{\Delta E \cdot w_n}{2} - V(T) \right) = 0 \quad . \quad (5)$$

For Fig. 2a

$$\alpha = \frac{V(T) - \frac{1}{2} \left[(F - 1)w_p E_{max} + (w_{ns} - w_n)(E_{max} - E_{Ro}) - \Delta E w_n \right]}{E_{max}(w_p + w_n)} \quad .$$

$$(6)$$

For Fig. 2b

$$\alpha^2 \left(\frac{E_{max}^2}{2S_s} \right) + \alpha(w_p E_{max}) + \left(\frac{w_p}{2} (F - 1)E_{max} - V(T) \right) = 0 \quad . \quad (7)$$

For Fig. 2c

$$\alpha = \frac{V(t)}{E_{max}\left(\frac{1}{S_L} + \frac{1}{S_s}\right)} \quad . \tag{8}$$

At this point, both the new particle positions and new electric field
profiles are known at the future time. Therefore new particle
velocities can be computed and the process is repeated. The particle
trajectories are computed until each particle encounters a point where
the electric field goes to zero. The time of this event is stored and
at the conclusion of the run these two transit times are printed out,
along with the velocities of the depletion edges at the time of collection.

3. Single-Drift GaAs IMPATTs

3.1 Uniformly Doped Structures. Extensive runs for uniformly
doped, single-drift IMPATTs were not carried out in this study;
however, one case is presented here which illustrates the operation of
these devices in the precollection mode.

The donor concentration for the device analyzed is 1.4×10^{16} cm^{-3}
and the length of the epitaxial layer is 3.24 µm. Figure 3 shows the
dc solution for J_{dc} = 1000 A/cm^2 and T = 500°K; it is seen that this
device is nonpunch through under these conditions. The avalanche
width, defined as the point where the hole current drops to 5 percent
of its maximum value, is 0.75 µm for this case. The depletion width
at dc is found to be approximately 2.75 µm.

A series of large-signal solutions was obtained for this device
at different frequencies and RF voltage amplitudes. The optimum
efficiency was 15.4 percent, obtained for f = 10 GHz, J_{dc} = 971 A/cm^2
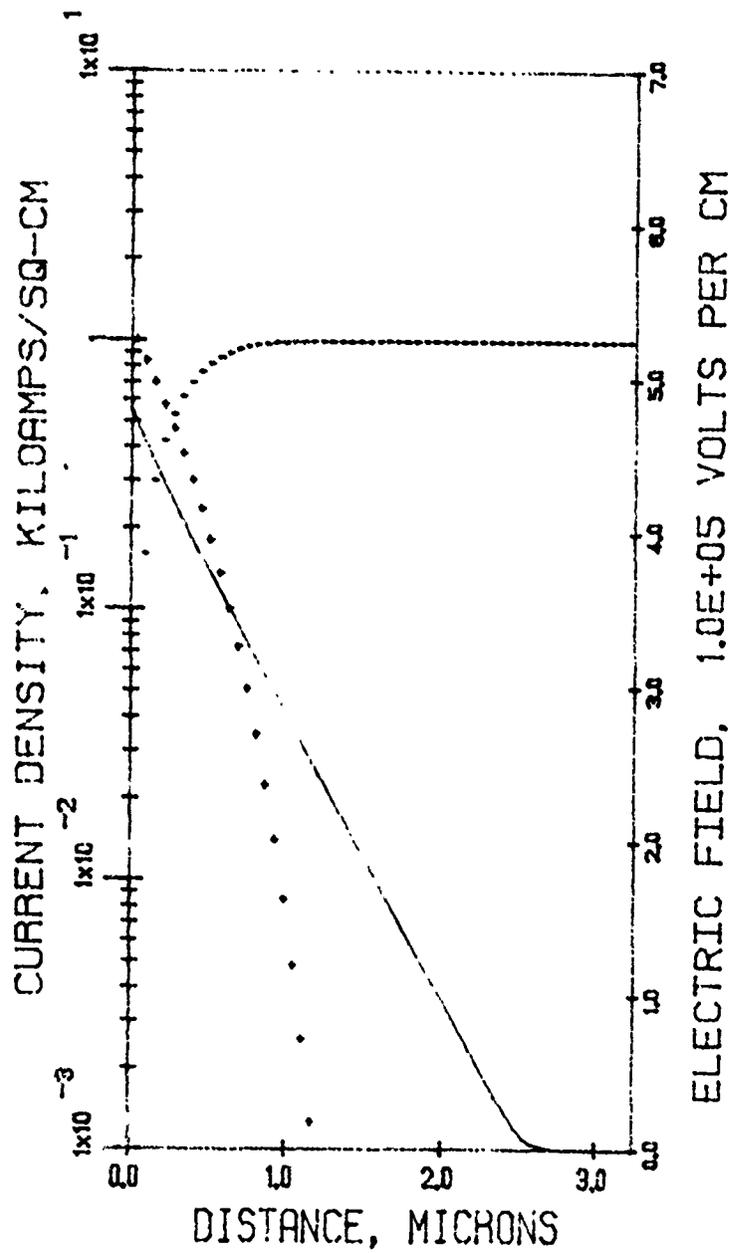
FIG. 3 DC SOLUTION FOR UNIFORMLY DOPED IMPATT FOR

J_{dc} = 1000 A/cm^2 AND T = 500°K.

and V_{RF} = 30 V, which is approximately one half of the dc operating voltage. The device voltage and current waveforms for this solution are shown in Fig. 4.

The "injected current" shown in Fig. 4a can be explained as follows. If the convention is adopted that positive electron and hole currents flow to the left while positive x is to the right, then the particle continuity equations are:

$$\frac{\partial p}{\partial t} = (G + R) + \frac{1}{q} \frac{\partial J_p}{\partial x} \qquad (9a)$$

and

$$\frac{\partial n}{\partial t} = (G + R) - \frac{1}{q} \frac{\partial J_n}{\partial x} , \qquad (9b)$$

where G, R are the generation and recombination rates ($cm^{-3}-s^{-1}$) and q is positive and equal to the electronic charge. Adding Eqs. 9 and integrating over the device length w gives

$$q \int_0^W \left(\frac{\partial p}{\partial t} + \frac{\partial n}{\partial t} \right) dx = 2q \int_0^W (G + R) \, dx + J_p(w)$$

$$- J_n(w) - J_p(0) + J_n(0) . \qquad (10)$$

It is now assumed that the device undergoes a periodic oscillation of period T seconds. Integrating Eq. 10 from 0 to T seconds and dividing by T shows that the term on the left-hand side is zero. Also, if J_{dc} is the average current for the oscillation, the following is obtained:

UNIFORMLY DOPED

VRF=30.

JDC= 971. A/CM**2

FREQUENCY = 10.0 GHZ
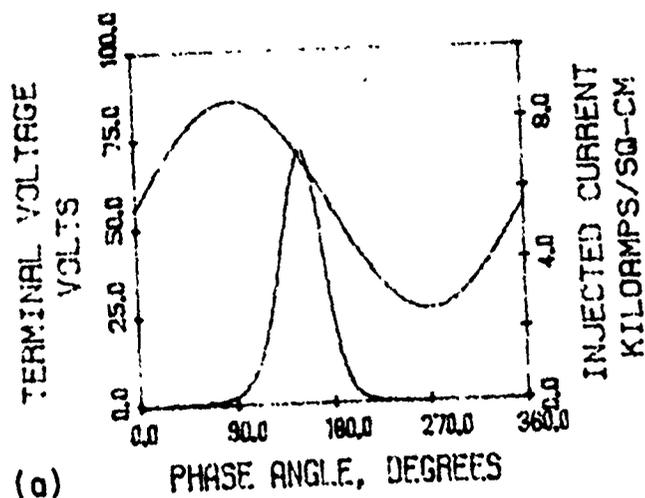
(a)
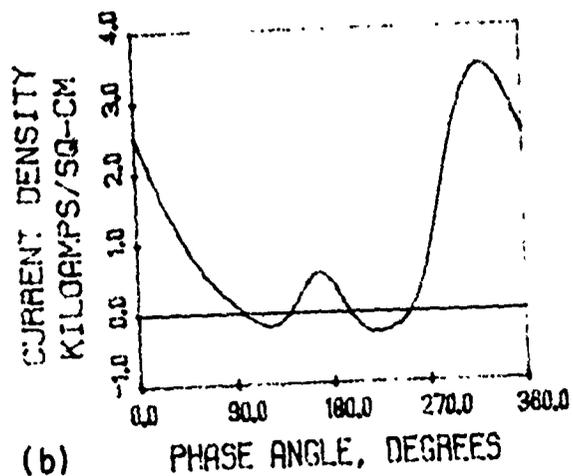
(b)

FIG. 4   LARGE-SIGNAL SOLUTION FOR THE STRUCTURE OF FIG. 3

WITH V_{RF} = 30 V AND J_{dc} = 971 A/cm^2.

-12-

$$J_{dc} = \frac{1}{T} \int_0^T [J_p(x = 0,t) + J_n(x = 0,t)] \, dt$$

$$= \frac{1}{T} \int_0^T [J_n(x = w,t) + J_p(x = w,t)] \, dt \quad . \quad (11)$$

Substituting from Eq. 11 yields

$$J_{dc} = \frac{1}{T} \int_0^T \left(q \int_0^W (G + R) \, dx + J_p(x = w,t) + J_n(x = 0,t) \right) dt \quad .$$

$$(12)$$

If the injected current is defined as

$$J_{inj}(t) \triangleq q \int_0^W (G + R) \, dx + J_p(x = w,t) + J_n(x = 0,t) \quad ,$$

$$(13)$$

it is seen that one of the requirements for having a periodic solution is that the time average of the injected current must be equal to the average terminal current J_{dc}. The reason for calling the expression in Eq. 13 the "injected" current is that it is a measure of the total charge injected into the device; charge injected at the boundaries appears in the J_p, J_n terms and charge appearing through generation appears in the spatial integral of the generation-recombination term. For IMPATTs, the generation term dominates in Eq. 13 and $J_{inj}(t)$ is essentially the total generation occurring throughout the device at time t.

The current density plotted in Fig. 4b is explained as follows. At any particular time, the total current is constant at any point in the device and is given by

$$J_{total} = J_p(x) + J_n(x) + \varepsilon \frac{\partial E}{\partial t} \quad . \tag{14}$$

Integrating over the length of the diode and dividing by w yields

$$J_{total} = \frac{1}{w} \int_0^W [J_n(x) + J_p(x)] \, dx + \frac{\partial}{\partial t} \left(\frac{\varepsilon}{w} V \right) \quad . \tag{15}$$

The second term on the right-hand side is the displacement current and does not contribute to real power flow. Therefore the terminal current plotted in Fig. 4b is given by

$$J_{ter} = \frac{1}{w} \int_0^W [J_n(x) + J_p(x)] \, dx \quad . \tag{16}$$

Although the displacement current term in Eq. 15 has been removed, some displacement current may appear in the terminal current calculated according to Eq. 16. w denotes the total length of the diode that is simulated; for example, w is greater than 3 μm for the diode of Fig. 3. However the depletion width of the diode is only 2.75 μm and furthermore the depletion width changes during the RF cycle. Hence the displacement term of Eq. 15 does not in general contain all of the displacement current.

Figure 5 presents curves at three points in the RF cycle of the electric field and particle distributions in the device. At 180 degrees in Fig. 5a, the electron pulse has been generated and is drifting to the right. In Fig. 5b at 252 degrees in the cycle, the pulse maximum meets the depletion edge which is moving to the left since the terminal voltage in Fig. 4 is decreasing. In Fig. 5c at 270 degrees, the electron pulse has been collected in the undepleted region. At this point of the RF cycle the width of the depleted region
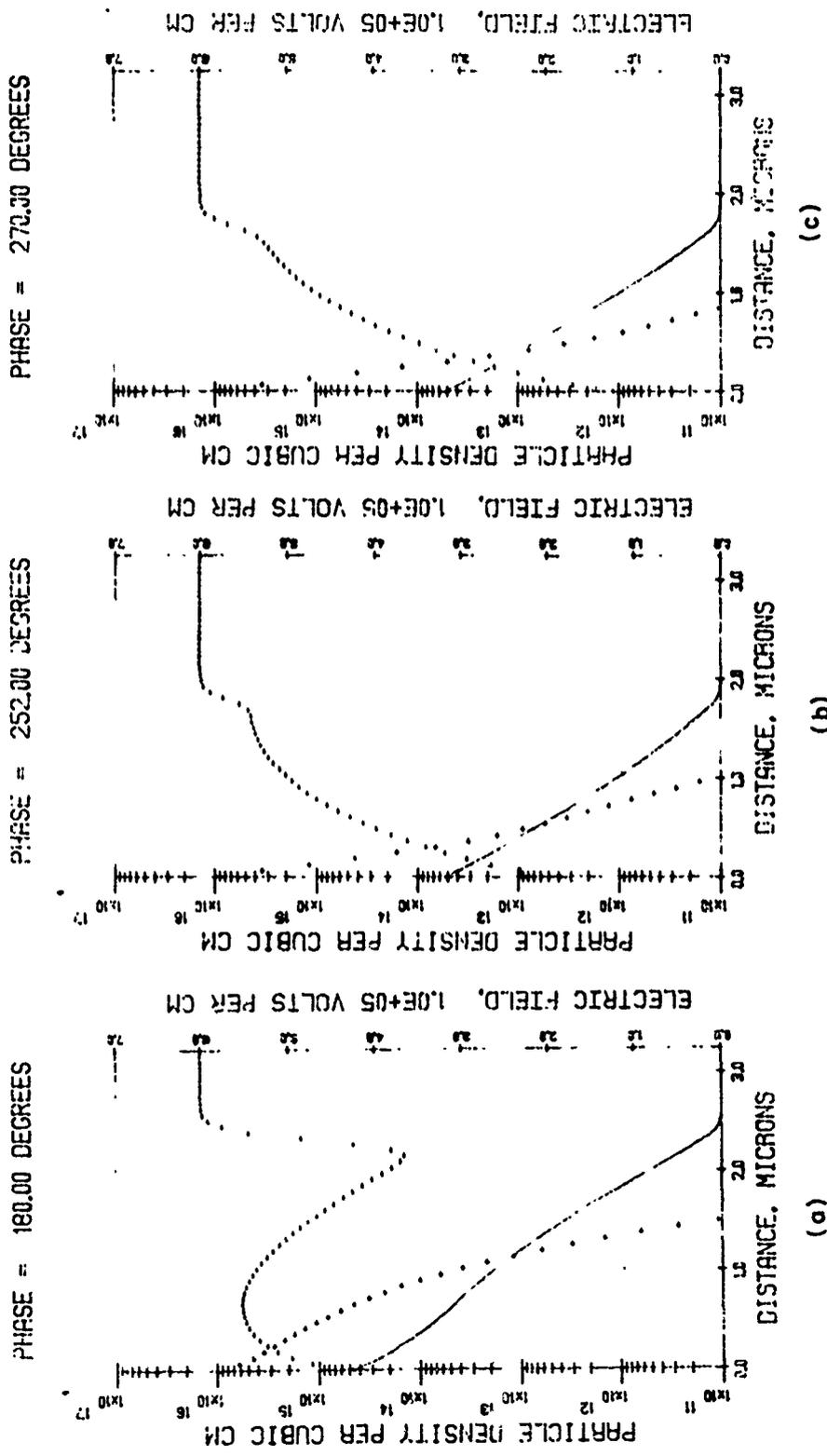
FIG. 5 PARTICLE CONCENTRATIONS AND ELECTRIC FIELD AT THREE TIMES DURING THE

LARGE-SIGNAL SOLUTION OF FIG. 4.

is less than 2 μm, considerably smaller than the dc value of 2.75 μm. Hence this device is operating in the precollection mode.

Between 270 and 360 degrees in the cycle the depletion edge moves from a position of 1.8 μm to 2.6 μm. The corresponding time is one quarter of the period, or 25 ps. Therefore the average velocity of carriers in the undepleted region during this time period is 3.2×10^6 cm/s, considerably less than the saturated velocity for electrons which is 5×10^6 cm/s. Therefore it is seen that predictions of the performance of precollection-mode devices based upon transit times calculated using saturated velocities can be significantly in error.

A simple equation for the movement of the depletion edge is derived as follows. $w, N_D(w)$ denotes the position of the depletion edge and the doping at that position at a particular time, Δw denotes a small change in the depletion edge position, and ΔV denotes the small change in terminal voltage brought about by Δw. Then

$$ w \times \Delta E = w \times \frac{q N_D(w)}{\varepsilon} (\Delta w) = \Delta V \quad . \tag{17} $$

Therefore the rate of change of w is

$$ \frac{dw}{dt} = \frac{\varepsilon}{q w N_D(w)} \frac{dV}{dt} \quad . \tag{18} $$

For example, at the end of the cycle ($\omega t = 2\pi$), using $w = 2.6$ μm, $N_D(w) = 1.4 \times 10^{16}$ cm^{-3} and $dV/dt = \omega V_{RF} = 2\pi \times 10^{10} \times 30$, Eq. 18 yields $dw/dt = 3.58 \times 10^6$ cm/s. The peak electron velocity at $T = 500°$K, which occurs for a field of 4 kV/cm, is 1.05×10^7 cm/s. According to Eq. 18, to achieve the peak electron velocity in the

undepleted region would require an RF voltage drive approximately 2.8 times the value for the solution of Fig. 4, which clearly is not possible for this structure. However, Eq. 18 also indicates that reducing the doping level in the drift region would achieve higher velocities and, in fact, it is shown later that near peak electron velocities can be obtained for high-low and low-high-low doping profiles, which is responsible for the high efficiencies in these structures.

Examination of the terminal current density of Fig. 4b shows that the current from 180 degrees to 270 degrees in the cycle is small, because the positive current induced by the drifting pulse is canceled by negative current in the undepleted region which is necessary for the movement to the left of the depletion edge. This effect tends to increase the efficiency, since the optimum current waveform would be a spike at 270 degrees. However, the effect is counteracted by the movement of the depletion edge to the right from 0 to 90 degrees, which increases the current during this portion of the cycle. Therefore in uniformly doped IMPATTs the effect of depletion-edge modulation is largely capacitive and does not significantly effect the efficiency.

The approximate analysis illustrated in Figs. 1 and 2 can be used to predict the RF performance of this device. The field profile is chosen to match the electric field resulting from the dc solution shown in Fig. 3. From the previous RF solution it was found that at 180 degrees in the cycle the maximum of the generated electron pulse is located approximately $0.9 \, x_A$, where x_A is the avalanche region width. The electron was injected at this location at

180 degrees in the approximate analysis, the diode was driven with a 10-GHz signal, and various RF voltage amplitudes were tried until the electron met the depletion edge with exactly a 25-ps transit time. It was found that the proper transit time resulted when the RF voltage amplitude was 50 percent of the dc voltage, almost exactly the same as the large-signal result. The approximate analysis works very well for this case because, since the doping is relatively high, space-charge effects brought about by the generated charge are minor. Hence the neglect of space-charge effects in the approximate analysis does not introduce significant error.

The approximate analysis could alternately have been applied as follows. If it is assumed that maximum efficiency will result from a voltage modulation of 50 percent, the RF voltage amplitude could be set and the frequency varied until the proper transit time is obtained. The frequency resulting from this procedure would again be 10 GHz.

3.2 Single-Drift High-Low GaAs IMPATTs. As was seen in the last section, the doping level in uniformly doped GaAs IMPATTs is too high to obtain near peak velocities for electrons in the undepleted region. However the drift region doping cannot be made too small because the transit time would become too large and space-charge effects become severe. The results of Bauhahn[6] indicate that for operation at 10 GHz the optimum drift region doping is approximately 5.5×10^{15} cm^{-3}. If Eq. 18 is evaluated with the same parameters as before but with $N_D(w) = 5.5 \times 10^{15}$, the velocity of electrons in the undepleted region at 360 degrees in the cycle is found to be 9.1×10^6 cm/s, or just below the peak velocity.

-18-

Thus it appears that $N_D \approx 5.5 \times 10^{15}$ cm^{-3} is a good choice for 10-GHz operation.

The first simulation of a high-low structure was for a diode previously analyzed by Bauhahn,[6] specifically diode No. 18 in Bauhahn's report, where an optimum large-signal efficiency of 28.9 percent was reported. The dc solution for the structure with $J_{dc} = 1250$ A/cm^2 is shown in Fig. 6a and the doping profile, in Fig. 6b. Figure 6c shows an equivalent low-high-low doping profile for this diode; it is equivalent in the sense that if a dc solution is obtained for the profile of Fig. 6c, the resulting avalanche width is the same as for Fig. 6b. Also, the electric field in the drift region is the same for both profiles. The Q_c given in Fig. 6c is the integral of the doping in the high region, in this case $0.04 \times 10^{-4} \times 6.07 \times 10^{17}$ cm^{-2}. The high region can be fabricated with a doping spike, such that the integral of the doping within the spike equals Q_c. For example, in this report the standard doping spike is taken to have a Gaussian profile with 0.035 μm half width. To realize the profile of Fig. 6c using such a spike, the height would be approximately 6.53×10^{17} cm^{-3} and it would be centered at 0.22 μm.

The choice of $J_{dc} = 1250$ A/cm^2 was made as follows. For highly efficient precollection of the electron pulse it is necessary for the height of the generated pulse to be slightly higher than the background doping at the point of collection. When this is true, the electric field flattens out and takes on a small positive slope in the vicinity of the pulse. This tends to bunch up the pulse as it is accelerated into the undepleted region, producing a spike of
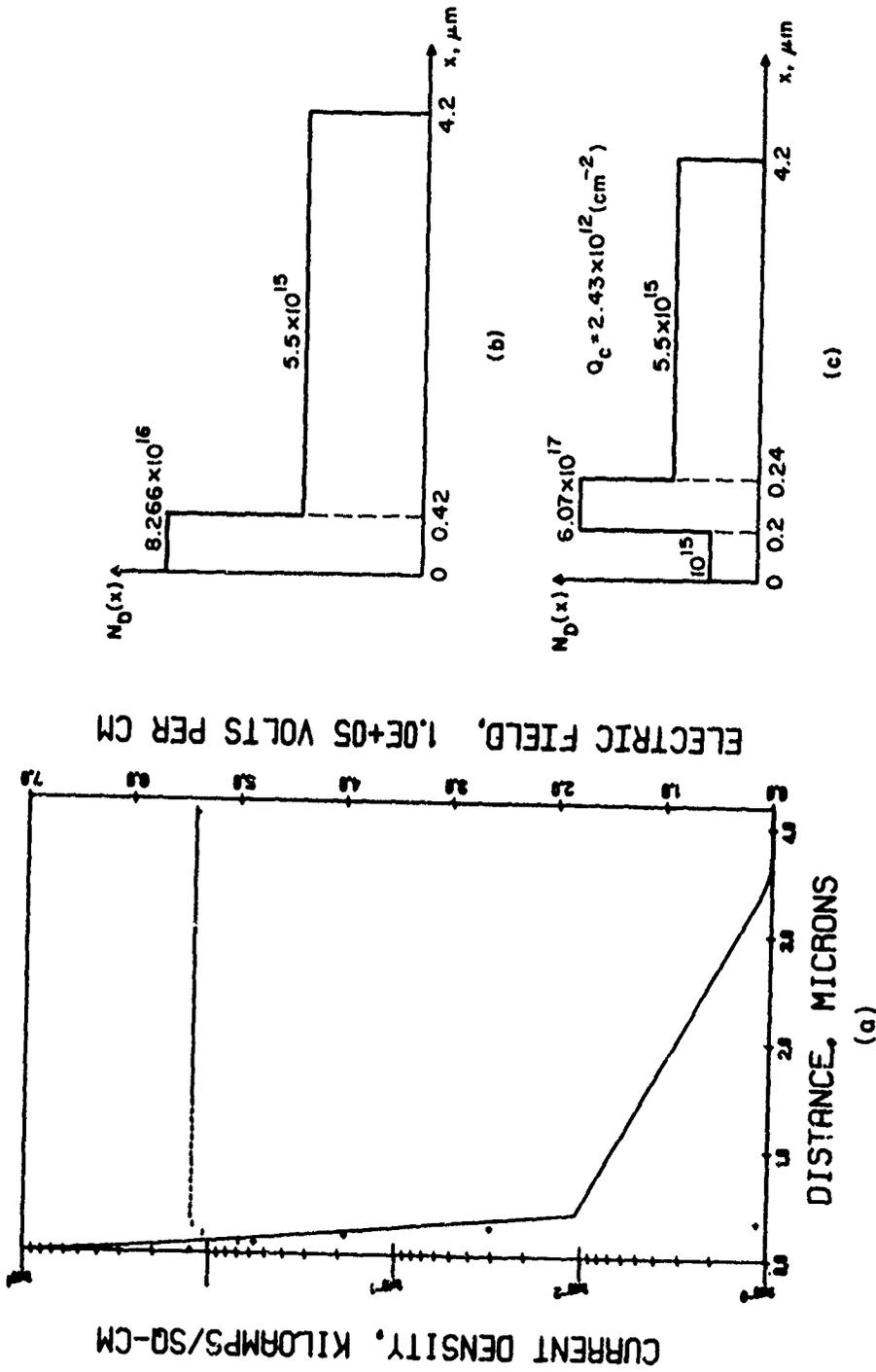
FIG. 6   (a) DC SOLUTION WITH J_{dc} = 1250 A/cm^2 AND T = 500°K,   (b) DOPING PROFILE AND

(c) EQUIVALENT LOW-HIGH-LOW DOPING PROFILE FOR THE STRUCTURE SIMULATED.

current near 270 degrees in the cycle, exactly where it is needed
for high efficiency. Since the height of the generated pulse is
directly proportional to J_{dc}, there is a threshold dc current above
which the height of the pulse is greater than the background doping.
Figure 7 shows results obtained by Bauhahn[6] indicating that this
threshold current is approximately 1000 A/cm^2 for operation at
10 GHz. If J_{dc} is increased too much above this threshold value,
the efficiency drops since the dc power increases faster than the
generated RF power. Simulations at different J_{dc} values showed that
optimum efficiency is obtained when the diode is biased slightly
above threshold, at $J_{dc} = 1200$ A/cm^2.

Figure 8 shows a large-signal solution obtained for the doping
profile of Fig. 6b. The diode terminal voltage and injected current,
as defined by Eq. 13, are plotted along with the terminal current
defined in Eq. 16. The spike near 270 degrees is brought about by
the precollection mechanism previously described. Figure 9a shows
the state of the diode as the electron pulse is accelerated into the
undepleted region. The pulse relaxes very quickly as it is collected,
of the order of the dielectric relaxation time since it enters a
region of low field. This produces a reduction in current as observed
in the terminal current waveform. As the terminal voltage recovers,
the field in the undepleted region increases such that the electrons
are extracted at velocities higher than the saturated velocity,
producing the second, broader peak in the terminal current. Figure 9b
shows the diode state as the electrons are being rapidly extracted.
At this point the electric field in the undepleted region is approximately
2 kV/cm for which the electron velocity is approximately 7.8 x 10^6 cm/s.
The efficiency resulting from this simulation was 27.67 percent.
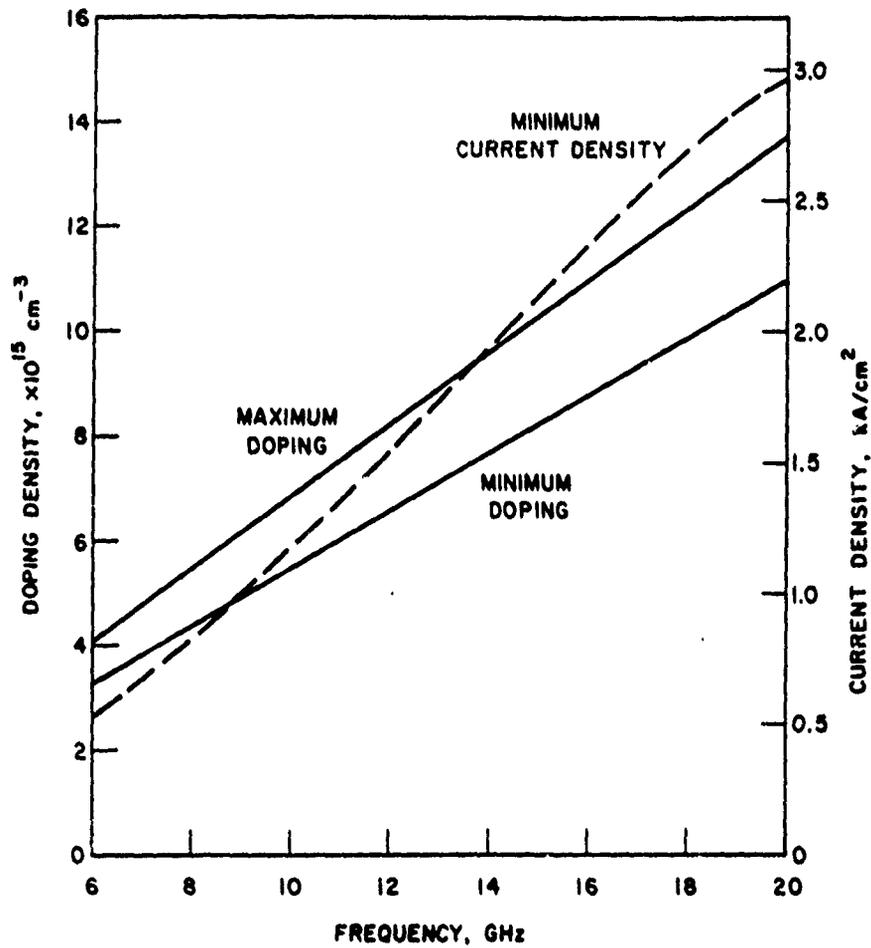
FIG. 7   MINIMUM AND MAXIMUM DOPING AND MINIMUM DC CURRENT
         DENSITY FOR THE PRECOLLECTION MODE AT VARIOUS
         FREQUENCIES.

VRFAMP=28.1

JDC= 1250. A/CM**2

FREQUENCY = 10.0 GHZ
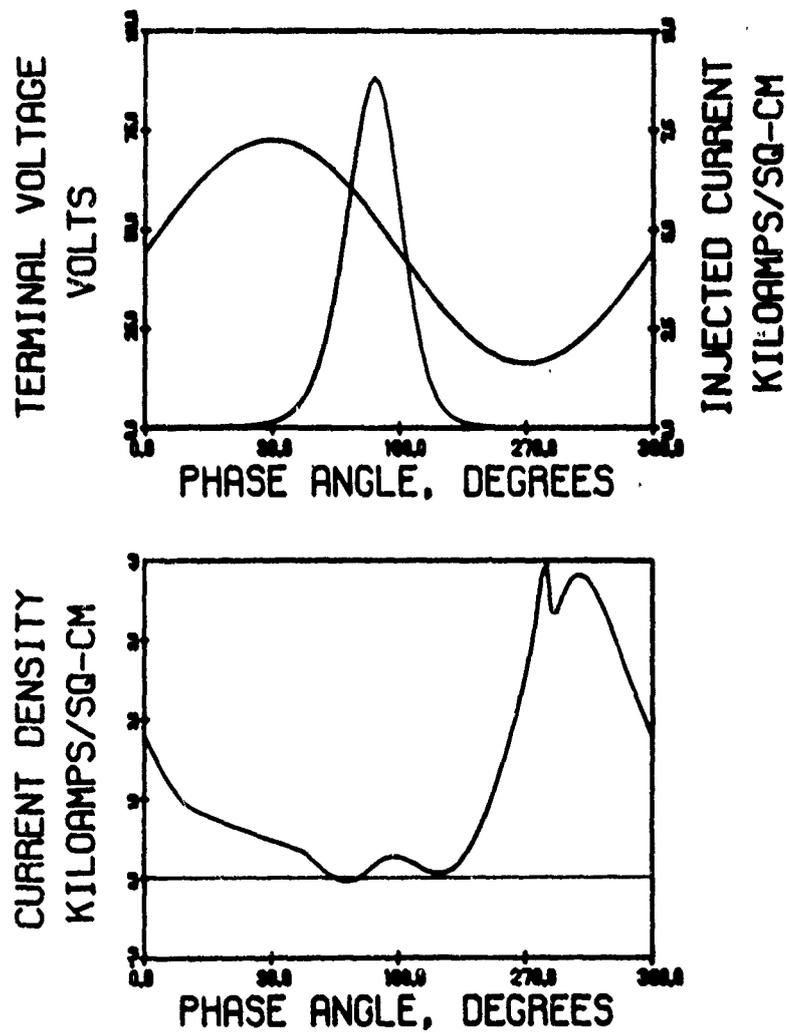
FIG. 8   LARGE-SIGNAL SOLUTION WITH 27.67-PERCENT EFFICIENCY FOR
THE STRUCTURE OF FIG. 6.
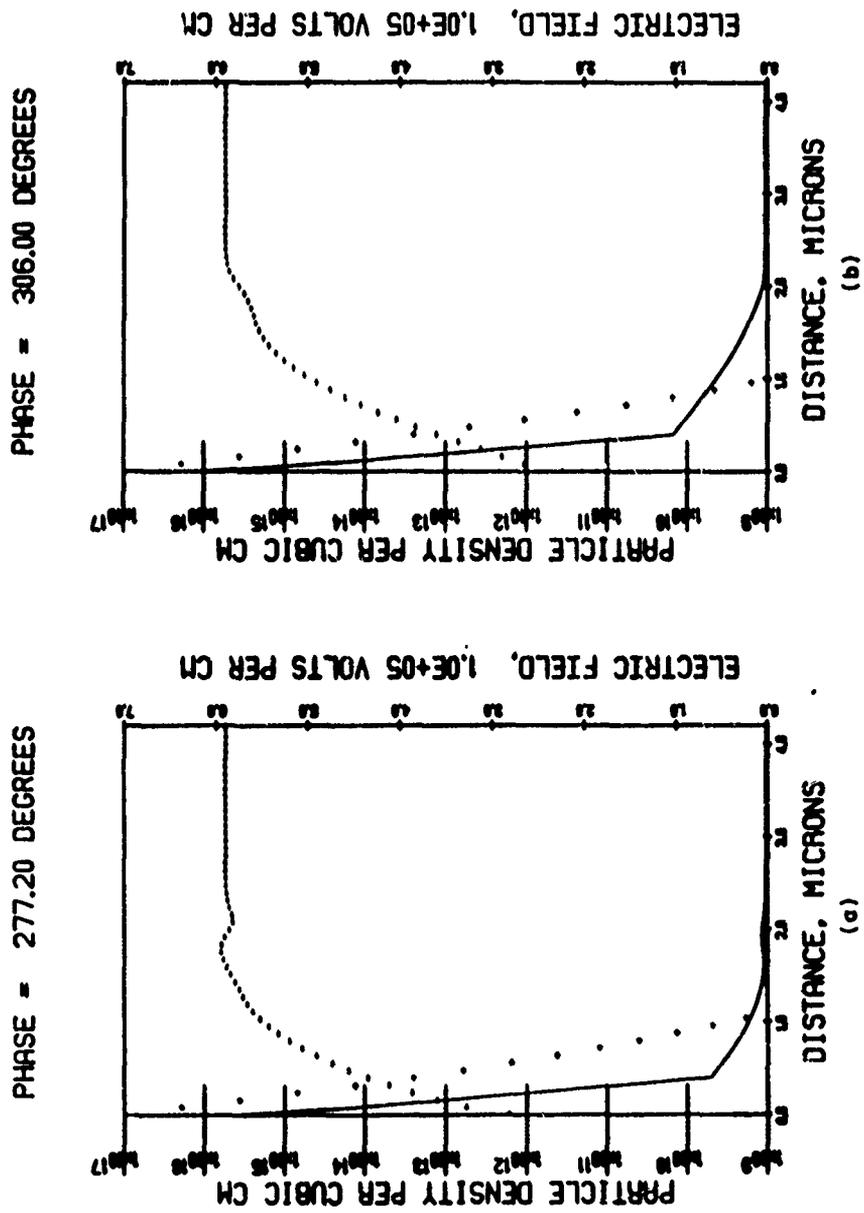
FIG. 9 DIODE STATE AT TWO DIFFERENT TIMES DURING THE SOLUTION OF FIG. 8.

Examination of the terminal current of Fig. 8 shows that the current is rather large during the first half of the cycle which reduces the efficiency. This is partially due to the movement of the depletion edge to the right and is therefore capacitive current. However near 90 degrees, since $dV/dt = 0$, the capacitive component disappears yet the current is still large. This can be understood by realizing that not all of the electron pulse is extracted at higher than the saturated velocity; some electrons are left behind and are extracted at the saturated velocity. Since the transit time at saturated velocity is long, all the electrons are not collected until well into the first half of the following cycle. For this reason, it is next shown that reducing the length of the diode results in higher efficiency.

Table 2 presents results of simulations of this structure at various dc current densities and RF voltages. All the runs are for $f = 10$ GHz and $T = 500°K$.

The next structure examined was the profile of Fig. 10a which is the same as that of Fig. 6b except that the length is shorter. The dc solution for $J_{dc} = 1250$ A/cm^2 and $T = 500°K$ is shown in Fig. 10b; it is seen that the device is slightly punched through for this shorter length. Figure 11 shows the terminal waveforms for the optimum large-signal run obtained for this structure. Comparison with Fig. 8 shows that, as expected, the terminal current is smaller during the first half of the cycle when the diode length is reduced; this results in higher efficiency. The efficiency calculated for the run of Fig. 11 was 29.35 percent. Table 3 shows the results obtained for this structure at different RF voltages, all at $f = 10$ GHz

Table 2

Large-Signal Results for the Structure of Fig. 6b with

$T = 500°K$ and $f = 10.0$ GHz

V_{RF} (V)	V_{dc} (V)	P_{RF} (W/cm^2)	η (Percent)	G ($\mho$/cm^2)	B ($\mho$/cm^2)	J_{dc} (A/cm^2)
31.15	47.4	1.40x10^4	16.96	-28.892	188.14	1740
32.0	43.3	1.35x10^4	17.93	-26.408	194.26	1740
33.0	43.6	7.76x10^3	9.97	-14.261	198.67	1780
29.0	48.0	1.10x10^4	15.61	-26.257	193.77	1470
30.0	44.1	1.774x10^4	27.23	-39.411	198.84	1480
31.0	42.9	1.277x10^4	20.11	-26.57	204.24	1480
32.7	43.0	1.215x10^3	1.88	- 2.272	208.86	1500
27.0	47.0	9.613x10^3	16.52	-26.373	200.01	1240
28.1	44.4	1.51x10^4	27.67	-38.245	205.98	1230
28.5	44.1	1.525x10^4	27.90	-37.55	206.48	1240
29.0	44.0	1.576x10^4	27.90	-37.482	205.47	1280
30.0	42.6	1.138x10^4	21.93	-25.291	213.96	1220
26.4	44.4	1.038x10^4	23.34	-29.775	212.34	1000
27.0	43.8	1.130x10^4	25.71	-30.994	215.34	1000
28.0	43.0	1.096x10^4	25.86	-27.953	219.55	985
29.5	40.9	3.954x10^3	9.84	- 9.087	231.57	983
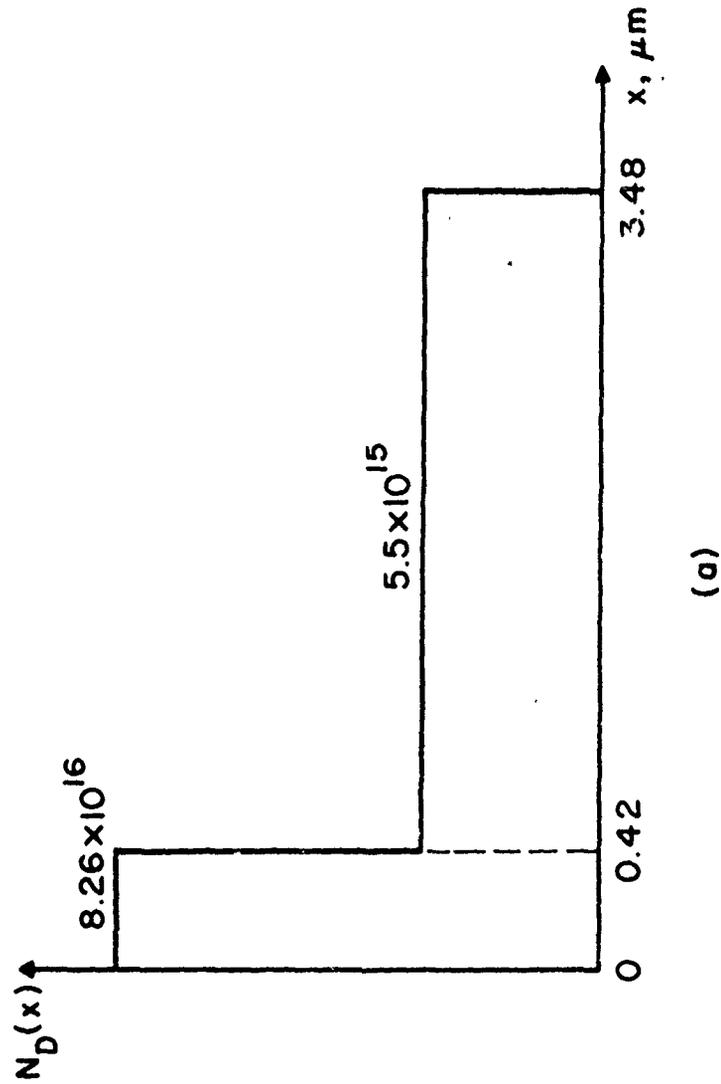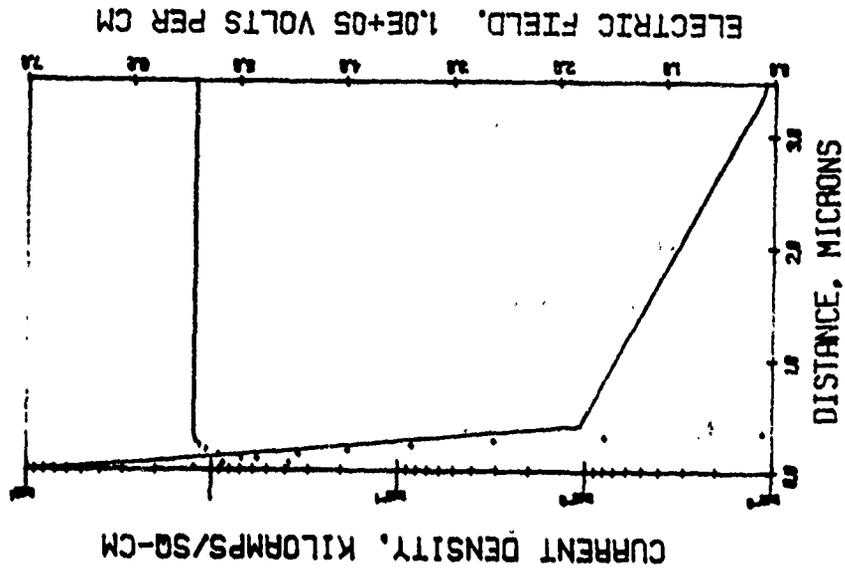
FIG. 10 (a) DOPING PROFILE AND (b) DC SOLUTION AT T = 500°K AND J_{dc} = 1250 A/cm² FOR A HIGH-LOW STRUCTURE SHORTER THAN THAT OF FIG. 6b.

PRECOLLECTION MODE

VRF=28.0

JDC= 1250. A/CM**2

FREQUENCY = 10.0 GHZ
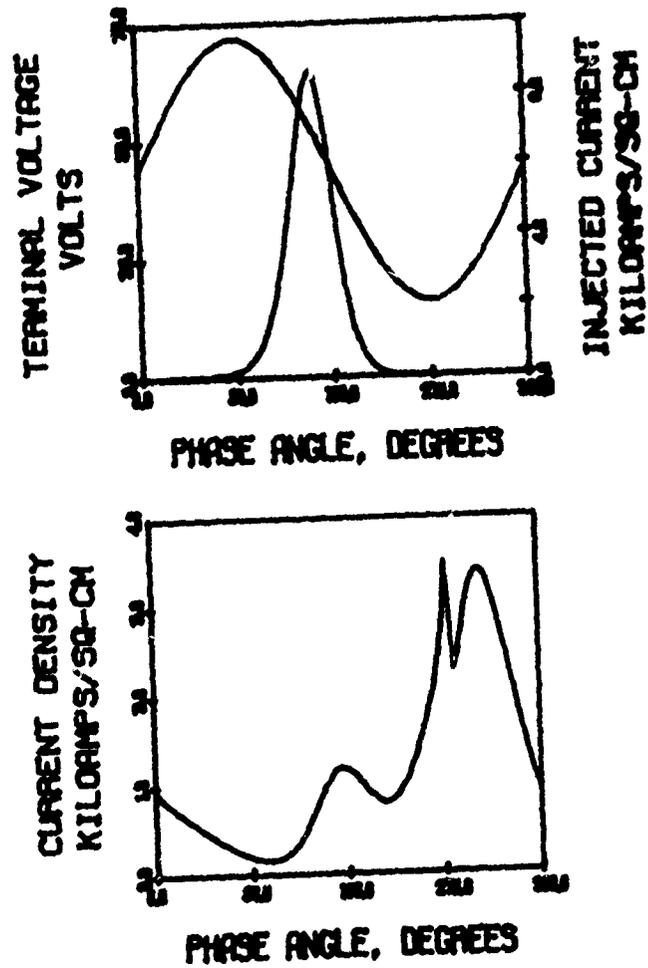
FIG. 11 LARGE-SIGNAL SOLUTION FOR THE STRUCTURE OF

FIG. 10a YIELDING 29.35-PERCENT EFFICIENCY.

Table 3

Large-Signal Results for the Structure of Fig. 10a
with T = 500°K and f = 10 GHz

V_{RF} (V)	G ($\mho/cm^2$)	B ($\mho/cm^2$)	n (%)	V_{dc} (V)	J_{dc} (A/cm²)	P_{RF} (W/cm²)
1.0	-143.52	30.591	0.12	46.6	1250	71.736
5.0	-119.44	166.36	2.55	46.8	1250	1.49×10^3
10.0	- 73.466	198.1	6.30	46.9	1240	3.67×10^3
15.0	- 52.937	205.14	10.21	46.9	1240	5.955×10^3
20.0	- 41.502	208.85	14.23	46.9	1240	8.3×10^3
25.0	- 35.76	210.71	19.30	46.2	1250	11.175×10^3
27.5	- 40.553	211.97	28.68	44.2	1210	15.334×10^3
29.8	- 40.062	212.7	29.22	43.8	1210	15.48×10^3
23.0	- 39.561	213.18	29.35	43.7	1210	15.508×10^3
28.5	- 37.321	215.03	28.92	43.3	1210	15.157×10^3
29.7	- 5.514	236.6	5.03	40.0	1210	2.432×10^3

and T = 500°K. Figure 12a shows a plot of negative conductance, susceptance, and efficiency vs. RF voltage; Fig. 12b presents dc voltage and RF power vs. RF voltage.

The next diode studied is similar to diode No. 12 in Bauhahn's report,[6] for which an optimum large-signal efficiency of 38.3 percent was reported. Figure 13a shows the low-high-low doping profile for this structure and Fig. 13b presents an equivalent high-low profile. If a Gaussian doping spike of 0.035 μm half width were used to realize the highly doped region of Fig. 13b, it would be centered at 0.39 μm with a height of 3.67×10^{17} cm^{-3}. The high doping of Fig. 13a is less than the value given in Bauhahn's report; this reduction was necessary to obtain the same electric field profile reported there. The reason for this is that different boundary conditions were used for these simulations than for the simulations reported by Bauhahn. Bauhahn used Dirichlet boundary conditions for both carrier concentrations; the simulations in this report use Dirichlet boundary conditions for the majority carrier, however, for the minority carrier a current boundary condition is imposed such that the current at the boundary is equal to a specified reverse saturation current, as explained in the introduction of this report.

Figure 13c shows the dc solution for J_{dc} = 1000 A/cm^2 and T = 500°K obtained with the doping profile of Fig. 13a. It is seen that the diode is significantly punched through at dc. An important parameter for these structures is E_{to}, defined as the electric field value at dc at the beginning of the drift region on the n-side. For Fig. 13c, E_{to} = 2.67×10^5 V/cm. For the previous structure of Fig. 10b, E_{to} was 1.8×10^5 V/cm.
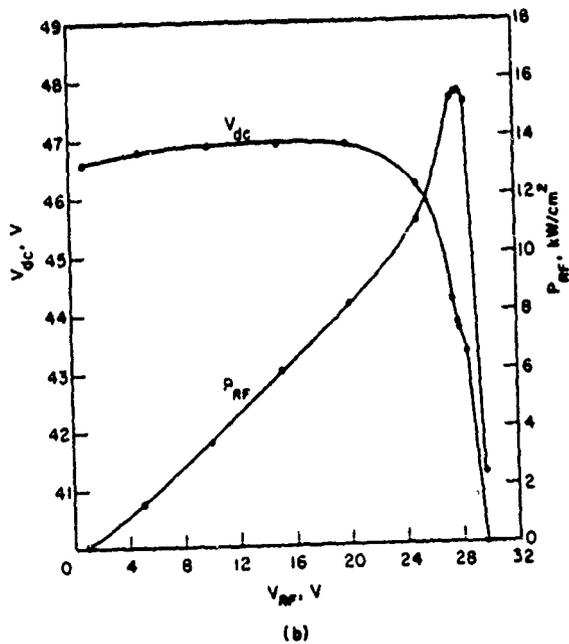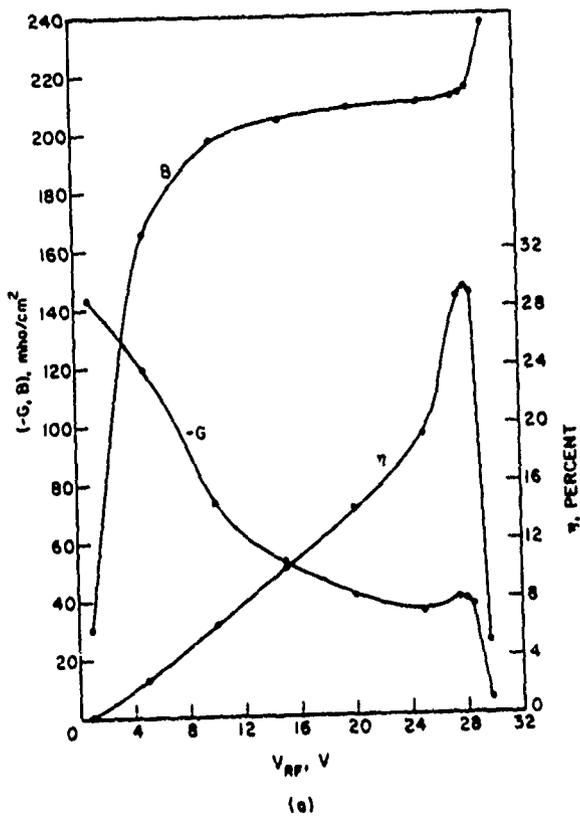
FIG. 12 LARGE-SIGNAL RESULTS FOR THE STRUCTURE OF FIG. 10a WITH

T = 500°K, f = 10 GHz AND $J_{dc} \simeq 1250$ A/cm^2.

-31-
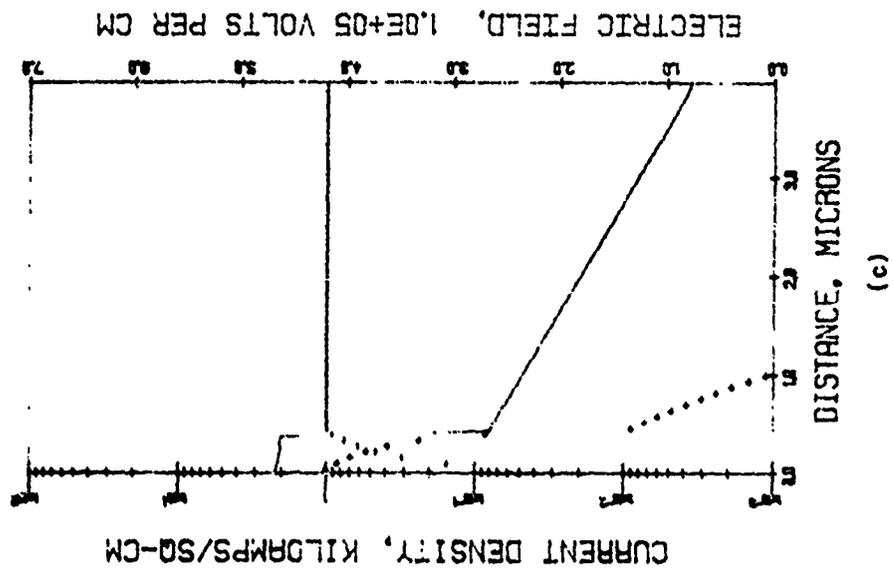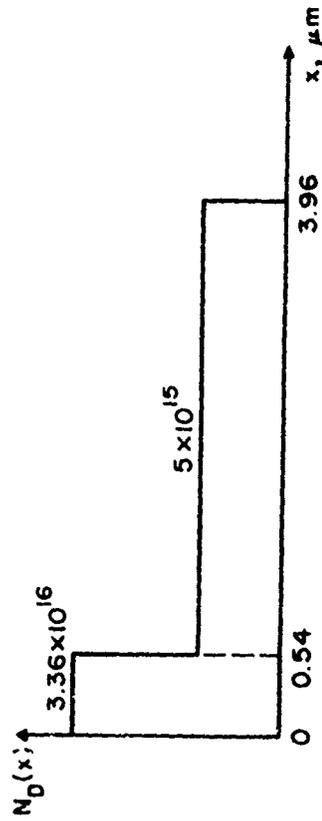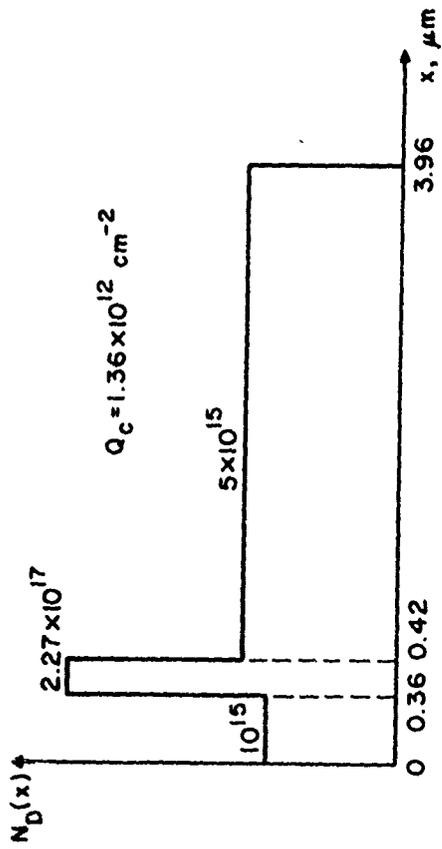
FIG. 13 (a) LOW-HIGH-LOW DOPING PROFILE, (b) EQUIVALENT HIGH-LOW PROFILE AND (c) DC SOLUTION OF (a) WITH T = 500°K AND J_{dc} = 1000 A/cm^2.

Figure 14 shows the device waveforms for the most efficient
(η = 35.12 percent) solution obtained with f = 8.5 GHz. The efficiency
at 10 GHz is not as good because the device is too long for optimum
operation at 10 GHz. The peak in the terminal current near 180
degrees is induced by the generated electron pulse drifting away
from the avalanche region; at 180 degrees the device is punched
through. The dip in terminal current near 230 degrees is caused
by the inward movement of the depletion edge, when the device becomes
nonpunch through. Near 270 degrees the inward movement of the depletion
edge ceases and the pulse is accelerated into the undepleted region,
both effects causing a peak in the terminal current. As before, when
the electric field recovers in the undepleted region, the electrons
are extracted at faster than the saturated velocity. At the end of
the cycle the diode is punched through again; however, a significant
current still flows because not all the electrons have been extracted.
If this structure is operated at 10 GHz the current at the end of the
cycle increases, which reduces the efficiency.

Table 4 shows the results of the simulations of the doping
profile in Fig. 13a at f = 8.5 GHz for different RF voltages. To
obtain optimum efficiency at 10 GHz the diode was shortened, resulting
in the profile of Fig. 15a. The dc solution with J_{dc} = 1200 A/cm^2
is shown in Fig. 15b. Figure 16 shows terminal waveforms for the
most efficient (η = 34.18 percent) solution at f = 10 GHz and Table 5
shows simulation results for different RF voltages. Figure 17a shows
a plot of negative conductance, susceptance and efficiency vs. RF
voltage for this structure; Fig. 17b shows dc voltage and RF power
vs. RF voltage. Comparison with Fig. 12 for the slightly punched

-33-

PRECOLLECTION MODE

VRF=55.0

JDC= 1150. A/CM**2

FREQUENCY = 8.5 GHZ
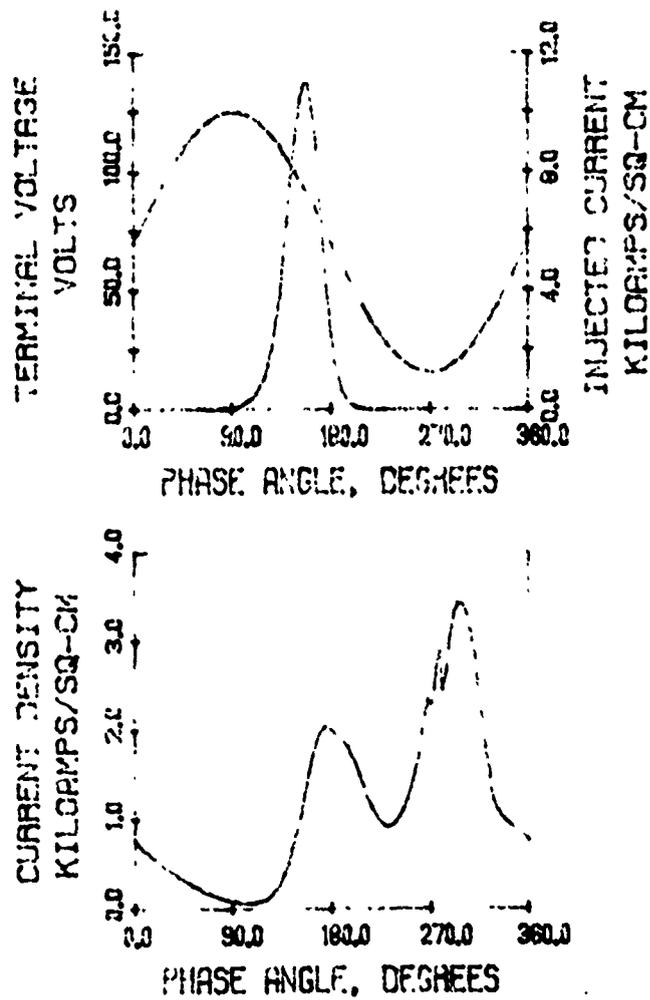
FIG. 14   LARGE-SIGNAL SOLUTION FOR THE DIODE OF FIG. 13a

WITH T = 500°K RESULTING IN 35.12-PERCENT EFFICIENCY.

Table 4

Large-Signal Results for the Structure of Fig. 13a

with f = 8.5 GHz and T = 500°K

V_{RF} (V)	G ($\mho/cm^2$)	B ($\mho/cm^2$)	η (%)	V_{dc} (V)	J_{dc} (A/cm^2)	P_{RF} (W/cm^2)
5.0	-73.726	23.018	1.00	77.2	1190	921.51
10.0	-79.574	105.18	4.27	77.1	1210	3.9785x10^3
15.0	-63.358	134.44	7.64	76.9	1210	7.1276x10^3
20.0	-51.762	146.16	10.91	76.7	1240	10.352x10^3
25.0	-41.912	154.39	14.39	76.1	1200	13.097x10^3
30.0	-35.95	157.62	17.72	75.4	1210	16.178x10^3
35.0	-31.184	159.63	21.15	74.3	1220	19.10x10^3
40.0	-27.51	160.7	24.74	72.7	1220	22.008x10^3
45.0	-23.554	162.28	28.54	70.4	1190	23.848x10^3
50.0	-21.943	161.87	33.98	67.3	1200	27.428x10^3
55.0	-18.74	147.21	35.12	70.3	1150	28.343x10^3
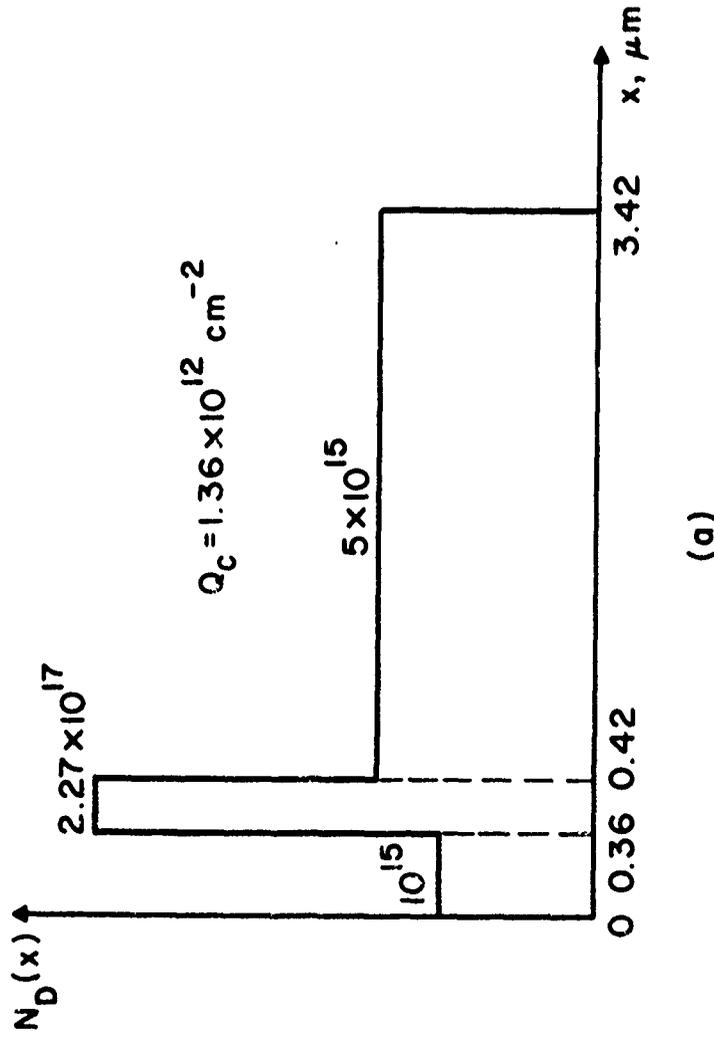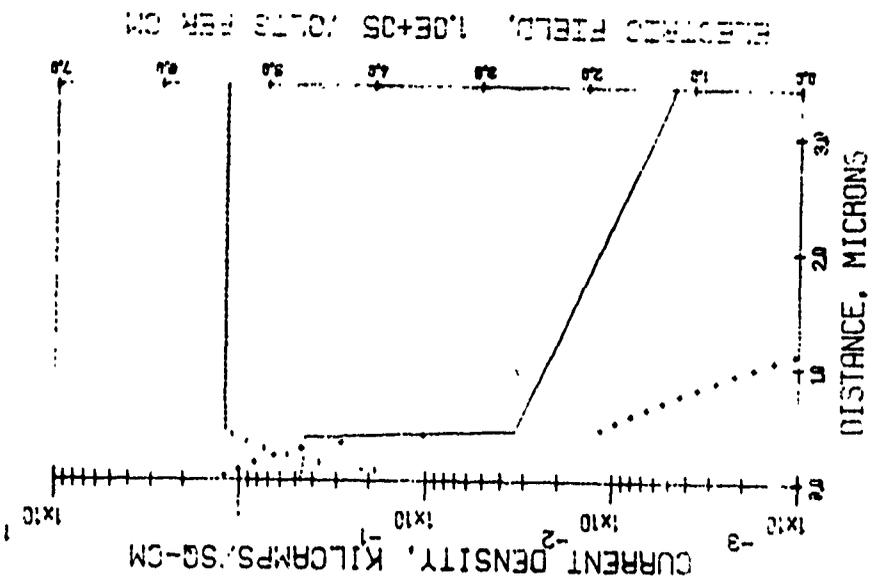
FIG. 15 (a) LOW-HIGH-LOW DOPING PROFILE WITH SHORTER OVERALL LENGTH THAN FIG. 13a AND (b) DC SOLUTION FOR (a) WITH T = 500°K AND J_{dc} = 1200 A/cm².

PRECOLLECTION MODE

VRF=51.9

JDC= 1160. A/CM**2

FREQUENCY = 10.0 GHZ
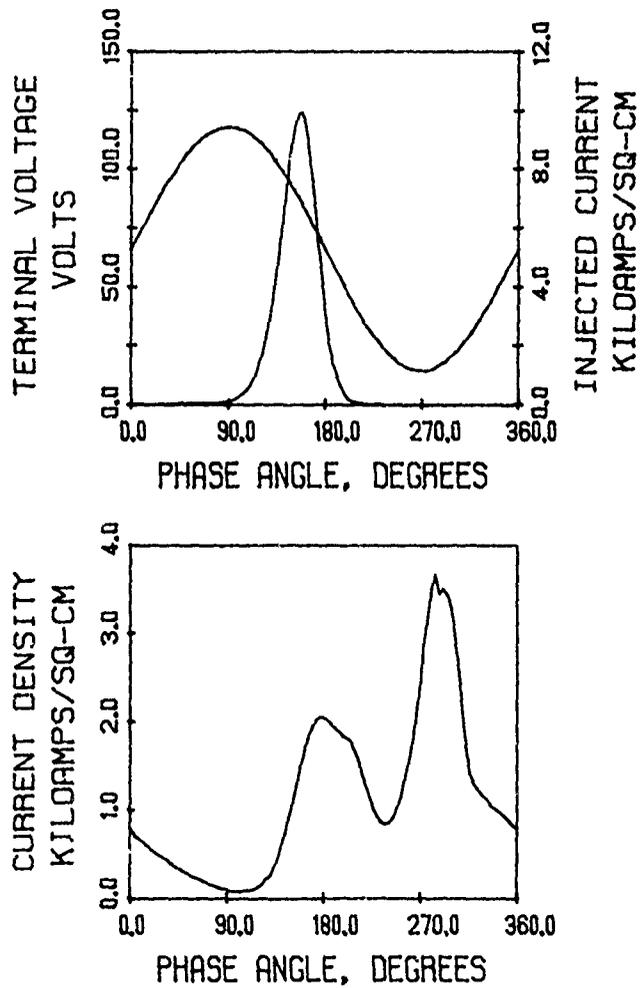
FIG. 16   LARGE-SIGNAL SOLUTION FOR THE STRUCTURE OF FIG. 15a

RESULTING IN η = 34.18 PERCENT.

-37-

Table 5

Large-Signal Results for the Structure of Fig. 15a

with f = 10 GHz, T = 500°K and E_{to} = 2.68 x 10^5 V/cm

V_{RF} (V)	G (℧/cm²)	B (℧/cm²)	η (%)	V_{dc} (V)	J_{dc} (A/cm²)	P_{RF} (W/cm²)
1.0	-125.84	79.127	.07	77.3	1200	62.898
5.0	-104.05	154.96	1.41	77.2	1200	1.3×10^3
10.0	- 70.45	183.3	3.76	77.2	1210	3.522×10^3
15.0	- 51.58	193.3	6.27	77.0	1200	5.8026×10^3
20.0	- 40.985	196.63	8.78	76.8	1210	8.197×10^3
25.0	- 34.05	198.2	11.35	76.5	1230	10.64×10^3
30.0	- 28.863	199.2	13.98	75.9	1220	13.0×10^3
35.0	- 24.386	200.0	16.63	74.9	1200	14.937×10^3
40.0	- 21.73	200.0	19.54	73.6	1210	17.384×10^3
45.0	- 18.997	200.0	22.18	71.1	1220	19.234×10^3
50.0	- 16.686	200.92	25.71	68.0	1190	20.857×10^3
51.0	- 16.729	201.02	27.24	67.1	1190	21.756×10^3
51.8	- 17.04	201.23	29.05	66.5	1180	22.862×10^3
51.9	- 19.42	199.92	34.18	66.1	1160	26.155×10^3
52.0	- 19.121	200.19	33.79	66.0	1160	25.851×10^3
52.8	24.69	220.63	-51.07	56.2	1200	-34.416×10^3
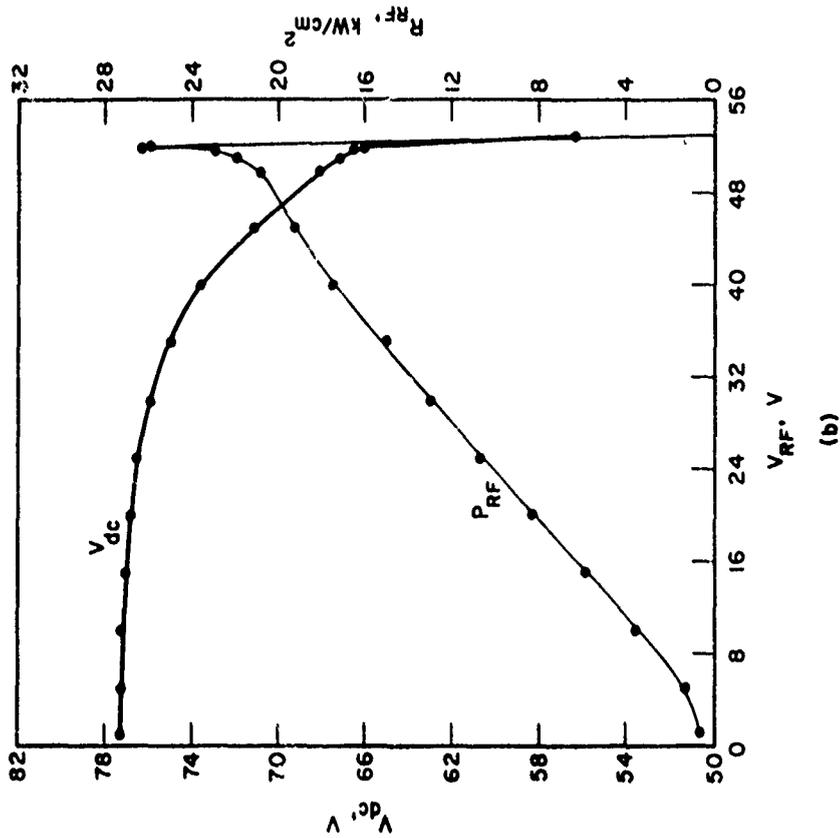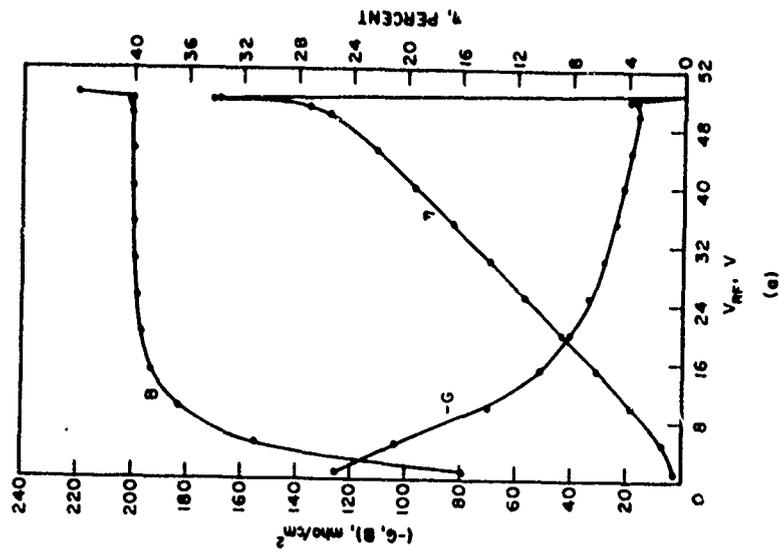
FIG. 17 LARGE-SIGNAL RESULTS FOR THE DIODE OF FIG. 15a WITH $f = 10$ GHz, $T = 500°K$ AND $J_{dc} = 1200$ A/cm^2.

through case with smaller E_{to} shows that as the diode becomes more punched through, the efficiency increases, the dc voltage rectification becomes larger, and the RF voltage range for which high efficiency is obtained is reduced.

Previously published results[7] indicated that GaAs IMPATTs should not be punched through at any point of the cycle. This argument is based on the fact that, for a given electric field modulation in the avalanche region, the maximum RF voltage swing is obtained for an under-punched-through structure; also the back-bias effect is reduced if nonpunch-through diodes are used. The simulations in this report consistently show that back bias is indeed more significant for punched-through structures and that the field modulation in the avalanche region is greater. However, allowing larger field modulations results in greater calculated efficiencies. That this is true can be explained as follows. To achieve the precollection mode, according to the simplified analysis (ignoring space-charge effects) the electric field profile of Fig. 15b must drop at 270 degrees in the cycle so that the field is zero at the location of the pulse maximum at that time. If E_{to} is raised but the field in the avalanche region remains the same, the amount by which the field must drop from the dc value at 270 degrees is increased. This produces an increase in RF voltage swing. However, raising E_{to} also increases the dc voltage which increases the dc power (J_{dc} remains the same for precollection). However, the dc voltage increase is due to the increase of the electric field in the drift region only, since the field in the avalanche region stays the same; in contrast, the RF voltage increase involves the entire

-40-

electric field profile, since the entire profile must drop to the level required for precollection. Hence as the diode is made more punched through, the RF voltage increases faster than the dc voltage, which increases the efficiency. This effect becomes more pronounced for double-drift GaAs IMPATTs, since then the field on the p-side remains unchanged as E_{to} is increased. (Of course the back-bias effect must also be taken into account which reduces both V_{RF} and V_{dc} as predicted from a simplified analysis.)

Another reason efficiency increases as E_{to} increases is related to the length of the device. Obviously any punched-through structure is shorter than the corresponding nonpunched-through structure. As previously mentioned, some electrons are left behind in the pre-collection process and must be extracted at saturated velocity. If the device is too long, these electrons produce a significant current at the beginning of the next cycle, thus reducing the efficiency. The punched-through structure is shorter, reducing the current at the beginning of the cycle and increasing the efficiency.

The increased back-bias effect in punched-through IMPATTs can result in thermal instabilities. This problem is addressed later in the report.

Because the range of RF voltage for which high efficiencies are obtained is quite narrow, as shown in Fig. 17a, an attempt was next made to modify the structure of Fig. 15a in order to stabilize the mode over a wider RF voltage range. After collection of the pulse near 270 degrees in the cycle, it is desirable that the depletion edge move at near peak velocity for as long a time as possible during the last quarter cycle. If w_c denotes the position of the depletion

edge upon collection of the pulse and t_c, the time of collection, then it is desirable to have

$$w(t) = w_c + v(t - t_c) \quad , \quad t \geqq t_c \quad , \tag{19}$$

where v denotes a velocity greater than the saturated velocity and less than the peak electron velocity and w denotes the depletion-edge position. Since the diode waveform is known from previous simulation of the structure with a uniformly doped drift region and it is assumed that the voltage waveform will not significantly change when the structure is modified, Eq. 18 may be solved for the $N_D(x)$ necessary to yield the desired depletion-edge movement. Since dV/dt = 0 at 270 degrees, the doping must be made smaller at the point of collection in order to increase the depletion-edge velocity soon after 270 degrees in the cycle. Near 360 degrees the dV/dt term approaches its maximum value so $N_D(x)$ must reach a larger value near the right-hand contact.

Figure 18a shows a doping profile resulting from the solution of Eq. 18; it is similar to the profile of Fig. 15a except that the drift region doping has been tailored for more efficient extraction of electrons. Figure 18b shows the dc solution for J_{dc} = 1200 A/cm^2. Figures 19a and b show large-signal results vs. RF voltage. It is seen that tailoring the drift region doping has resulted in high-efficiency precollection for a wider range of RF voltages. Also, the maximum efficiency is slightly higher. Hence there is an advantage to designing high-efficiency GaAs IMPATTs with a positive doping gradient in the drift region. Figure 20 shows terminal waveforms for this structure which yield the best efficiency, η = 35 percent.
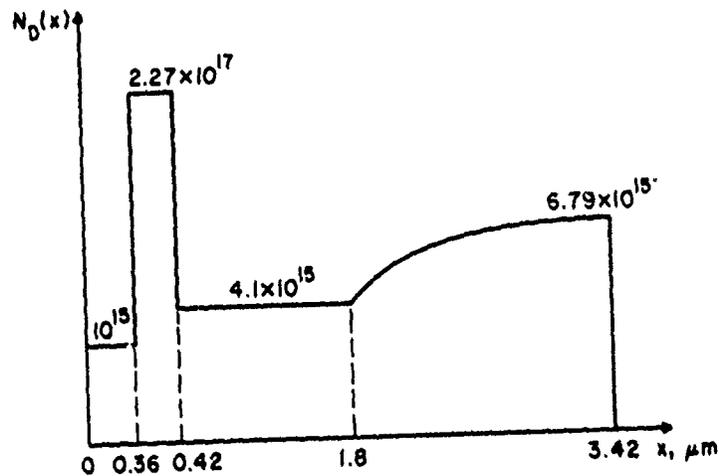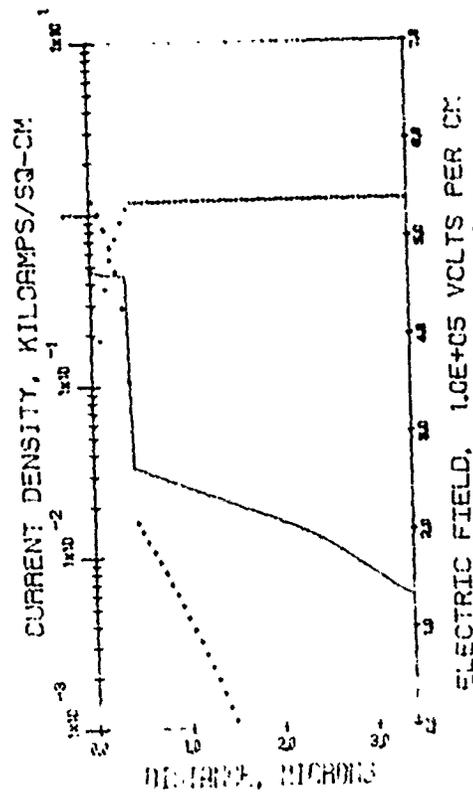
FIG. 18 (a) DOPING PROFILE TAILORED FOR MORE EFFICIENT EXTRACTION

OF ELECTRONS AND (b) DC SOLUTION OF THE PROFILE WITH

J_{dc} = 1200 A/cm^2, T = 500°K AND E_{to} = 2.67 x 10^5 V/cm.

-43-
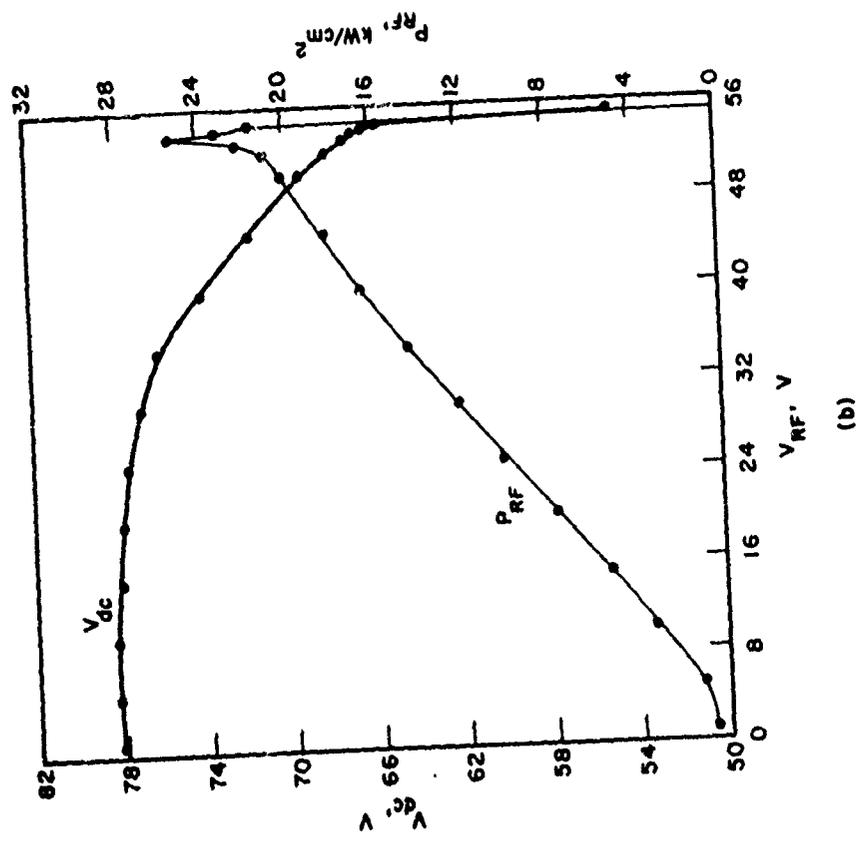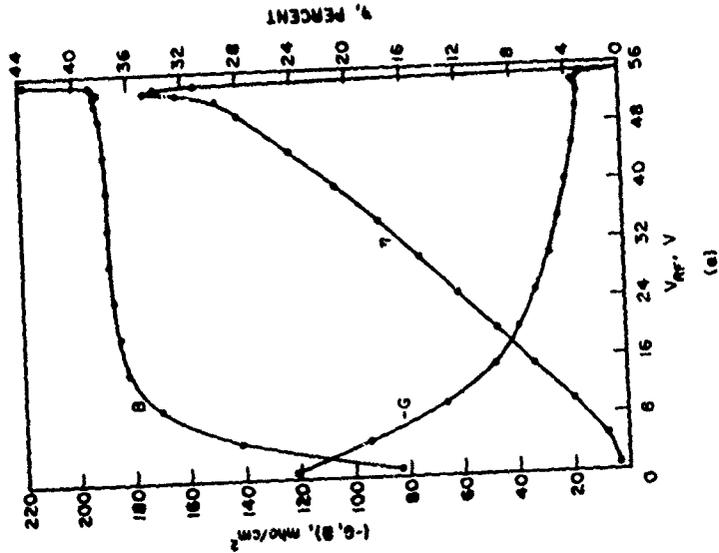
FIG. 19 LARGE-SIGNAL RESULTS FOR THE TAILORED DOPING PROFILE OF FIG. 18a WITH f = 9.5 GHz,

T = 500°K AND J_{dc} ≈ 1050 A/cm².

PRECOLLECTION MODE

VRF=53.7

JDC= 1050. A/CM**2

FREQUENCY = 9.5 GHZ
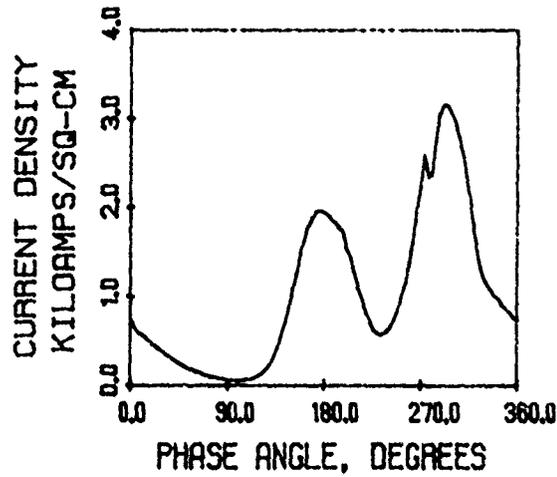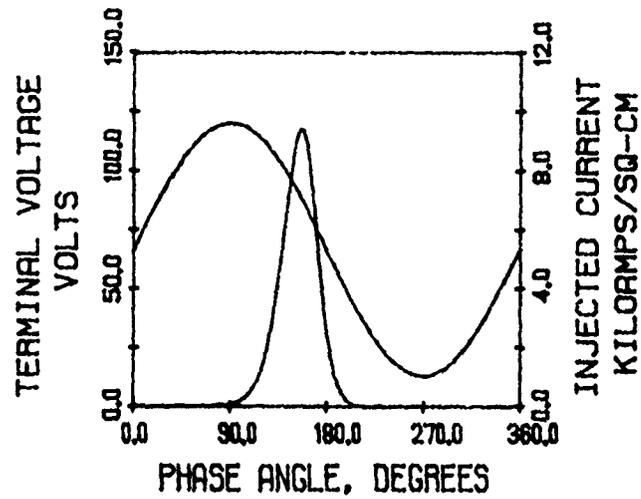
FIG. 20 LARGE-SIGNAL SOLUTION FOR THE STRUCTURE OF FIG. 18a

WITH T = 500°K RESULTING IN 35.0-PERCENT EFFICIENCY.

The next structure studied was similar to Fig. 18a except that the avalanche region width was reduced by one-half. Figure 21a shows the resulting profile where the height of the highly doped region was also adjusted so that the field in the drift region is the same as for the structure of Fig. 18a. (It is necessary to increase this doping because, since the avalanche region width is smaller, the maximum electric field in the device is higher.) Figure 21b shows the dc solution for this profile with J_{dc} = 980 A/cm^2. If the highly doped region were realized with a Gaussian doping spike of 0.035 μm half width, the height of the spike would be 5.5 x 10^{17} cm^{-3} and it would be located at 0.2 μm. Table 6 shows the results of large-signal simulations of this structure; it is seen that halving the avalanche width has increased the maximum efficiency from 35 to 38.3 percent. Figure 22 shows plots of the large-signal results vs. RF voltage for f = 9.5 GHz and T = 500°K.

The next structure examined was a modification of the structure of Fig. 15a to show the effect of increasing the doping in the drift region. Figure 23a shows the profile with N_D in the drift region increased to 7.8 x 10^{15} cm^{-3}; the device length is also increased so that it is nonpunch through during the entire RF cycle. Figure 23b shows the dc solution for this structure. The maximum large-signal efficiency obtained was 22 percent since the generated electron pulse is no longer higher than the background doping at the point of collection; as previously explained, the pulse must be higher than the background doping for efficient precollection to occur. This result confirms that the optimum doping level in the drift region for precollection at 10 GHz is approximately 5 x 10^{15} cm^{-3}.

ELECTRIC FIELD, 1.0E+05 VOLTS PER CM

DISTANCE, MICRONS

(b)

CURRENT DENSITY, KILOAMPS/SQ-CM

$Q_c = 2.04 \times 10^{12}$ cm^{-2}

$E_{to} = 2.65 \times 10^5$ V/cm

6.79×10^{15}

4.1×10^{15}

6.814×10^{17}

10^{15}

$N_D(x)$

(a)
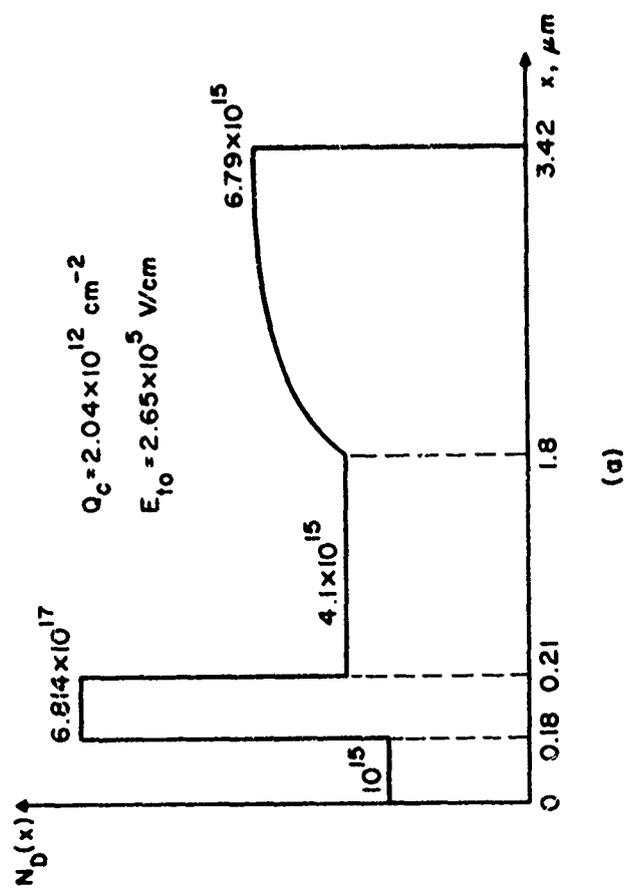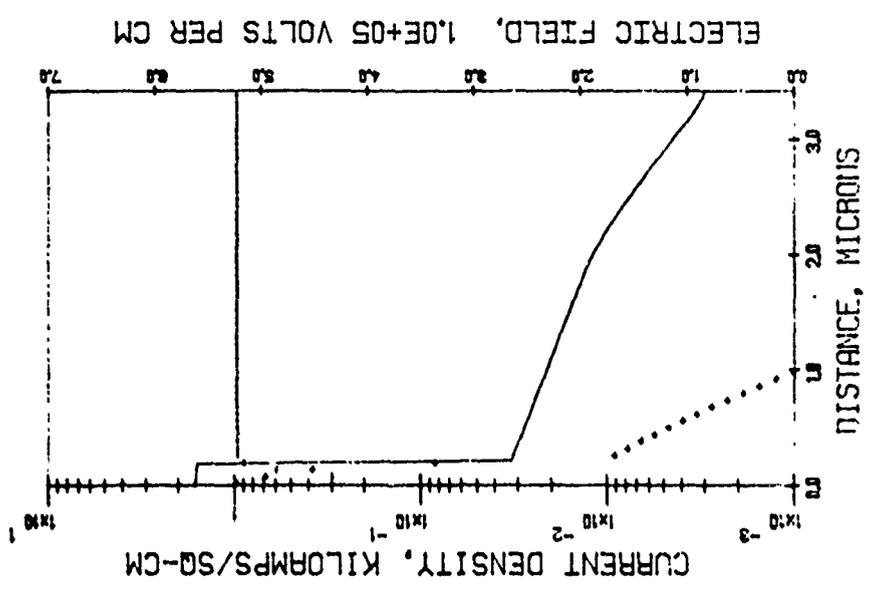
FIG.   (a) DOPING PROFILE SIMILAR TO THAT OF FIG. 18a BUT WITH REDUCED AVALANCHE WIDTH

AND (b) DC SOLUTION OF (a) WITH T = 500°K AND J_{dc} = 980 A/cm^2.

Table 6

Large-Signal Results for the Diode of Fig. 21a

at $T = 500°K$ and $f = 9.5$ GHz

V_{RF} (V)	G ($\mho/cm^2$)	B ($\mho/cm^2$)	η (%)	V_{dc} (V)	J_{dc} (A/cm²)	P_{RF} (W/cm²)
5.0	-92.214	163.97	1.64	72.1	977	1.1526x10³
10	-61.892	183.29	4.37	72.0	984	3.0945x10³
20	-35.895	191.7	10.05	71.7	996	7.1788x10³
30	-24.147	193.25	15.84	70.8	968	10.866x10³
40	-19.098	193.15	22.72	68.3	985	15.279x10³
46	-16.231	195.06	27.04	65.7	967	17.172x10³
48	-15.566	195.89	28.92	64.4	962	17.932x10³
50	-15.397	196.65	31.83	63.0	961	19.246x10³
50.5	-15.685	196.76	33.48	62.5	956	20.0x10³
51.0	-17.44	196.24	38.3	61.9	957	22.68x10³
52	-11.775	200.52	27.17	59.8	979	15.919x10³
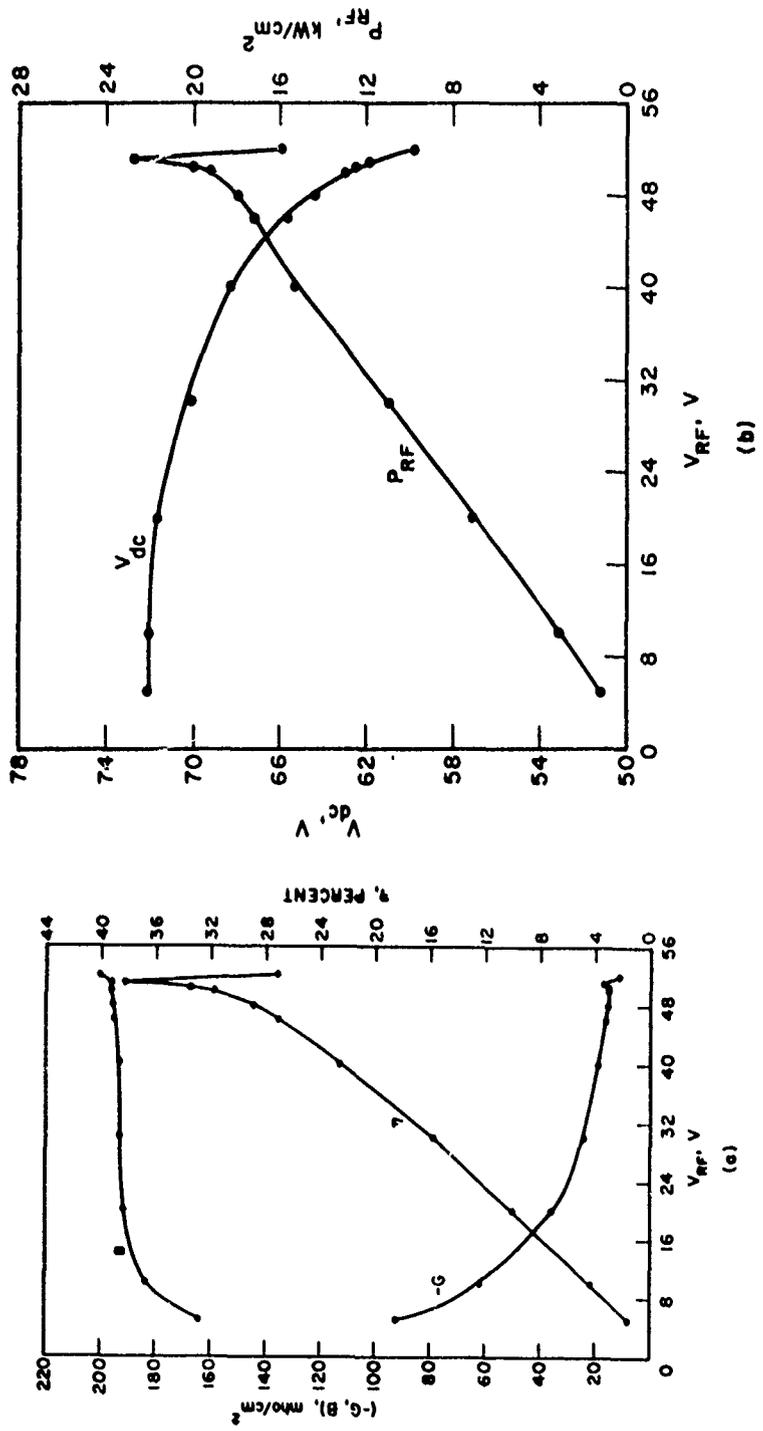
FIG. 22 LARGE-SIGNAL RESULTS FOR THE DIODE OF FIG. 21a AT T = 500°K, f = 9.5 GHz

AND $J_{dc} \approx 980$ A/cm^2.
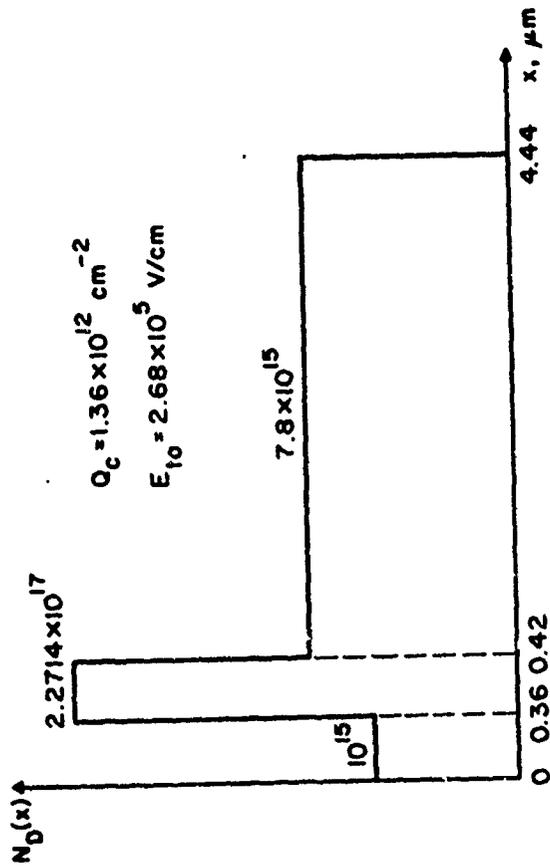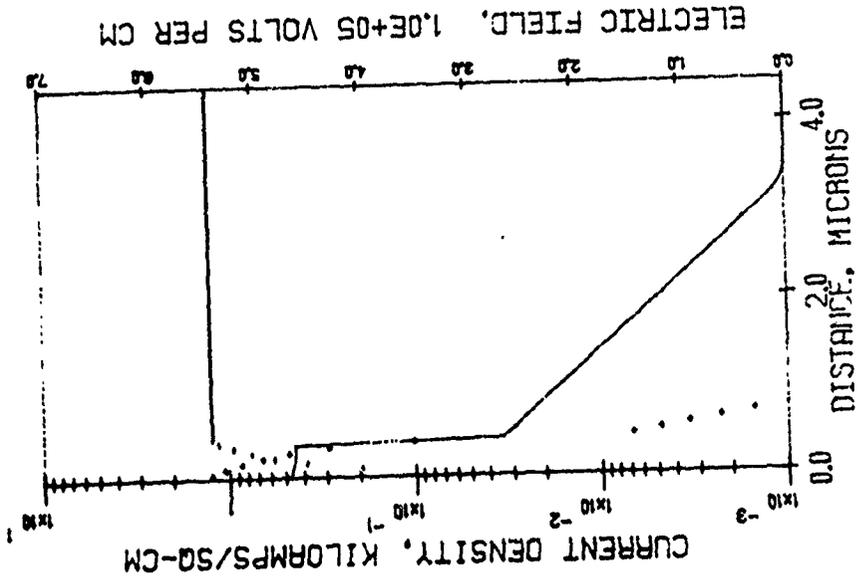
(a) DOPING PROFILE MODIFIED FROM FIG. 15a BY INCREASING OVERALL LENGTH AND DRIFT REGION DOPING AND **(b)** DC SOLUTION WITH T = 500°K AND J_{dc} = 1250 A/cm^2.

FIG. 23

4. Double-Drift GaAs IMPATTs

4.1 Uniformly Doped Structures.

The approximate analysis developed in Section 2 can be used to design uniformly doped, double-drift GaAs IMPATTs. From the simulations of single-drift, uniformly doped diodes it can be inferred that precollection of the electron pulse will occur on the n-side near 270 degrees in the cycle. Therefore a reasonable design procedure is to ensure that the injected electron in the approximate analysis has about a one-quarter period transit time before it meets the depletion edge. Also, it has generally been found in these simulations that optimum efficiency occurs when V_{RF} is approximately one-half V_{dc}; this value of voltage modulation may also be incorporated in the approximate analysis.

Figure 24 shows an electric field profile which resulted from the approximate analysis for operation at 10 GHz. From dc solutions of similar structures, it was found that the peak field is approximately 4.04×10^5 V/cm at 500°K. Also, it is a typical design procedure to make the electric field on the left-hand side approximately $0.25\ E_{max}$; this ensures that the device is punched through on the p-side for most or all of the RF cycle. The lengths in Fig. 24 are obtained from the approximate analysis. If a 10-GHz sinusoidal voltage of magnitude $V_{dc}/2$ is impressed across the device, it is found that a dc depletion width of approximately 2.1 µm on the n-side yields an electron transit time of 25 ps. As explained in Section 2, the electron transit time is the time between the electron injection at the half-cycle point and the time when the injected electron meets the depletion edge on the right-hand side, where the electric field goes to zero in the approximate model. A transit time of 25 ps is desired for a 10-GHz signal because the electron pulse should be collected

-51-
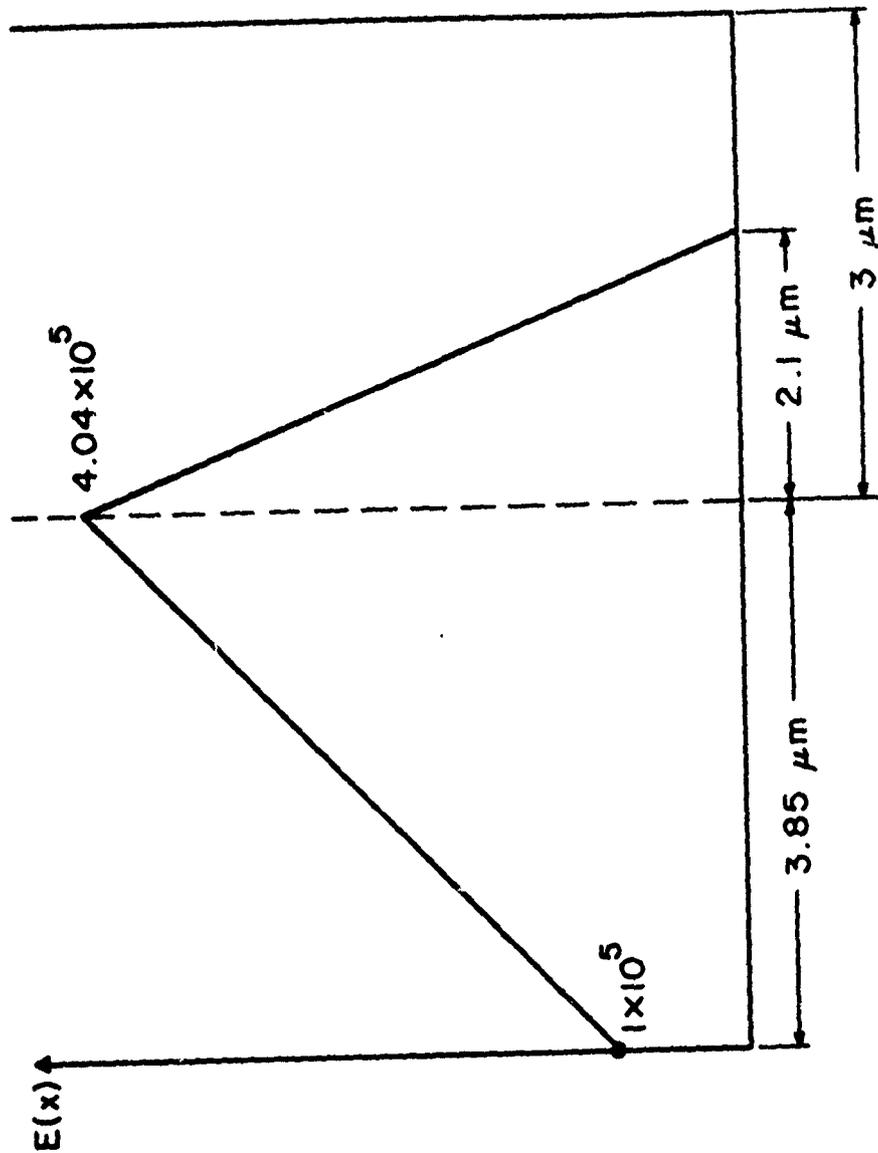
FIG. 24 DC ELECTRIC FIELD PROFILE RESULTING FROM THE APPROXIMATE ANALYSIS FOR OPERATION AT 10 GHz.

near 270 degrees in the cycle for optimum operation. Of course, at the time of collection the depletion width on the n-side is significantly smaller than it is for the dc solution. (The initial electron position at 180 degrees was determined from previous large-signal simulations of similar structures; it was 0.2 µm to the right of the junction. The hole starting position was 1.4 µm to the left of the junction, which was also determined from large-signal simulations.) The length of the p-side was chosen so that the hole transit time is 45 ps, slightly less than half the period. The efficiency is improved if the hole transit time is somewhat less than T/2, since then the pulse is more thoroughly collected by the end of the cycle. (Due to back diffusion, some of the holes arrive after the pulse maximum at the left-hand boundary.) An additional micron of undepleted material is added on the n-side so that the diode is never punched through on the n-side.

A doping profile that yields a dc electric field similar to that of Fig. 24 for J_{dc} = 1000 A/cm^2 is shown in Fig. 25a; Fig. 25b shows the dc solution for this structure at T = 500°K. Tab.e 7 shows the results of large-signal simulations of this structure; the optimum frequency was found to be 9 GHz rather than 10 GHz, although better than 15-percent efficiency was obtained at 10 GHz. It is believed that these results represent realistic efficiencies obtainable from uniformly doped GaAs double-drift diodes at X-band.

Figure 26 shows the terminal waveforms for the optimum solution obtained with this structure at f = 9 GHz. Near 180 degrees both pulses drift toward their respective contacts, producing a positive induced current as shown in Fig. 27a; however, this positive
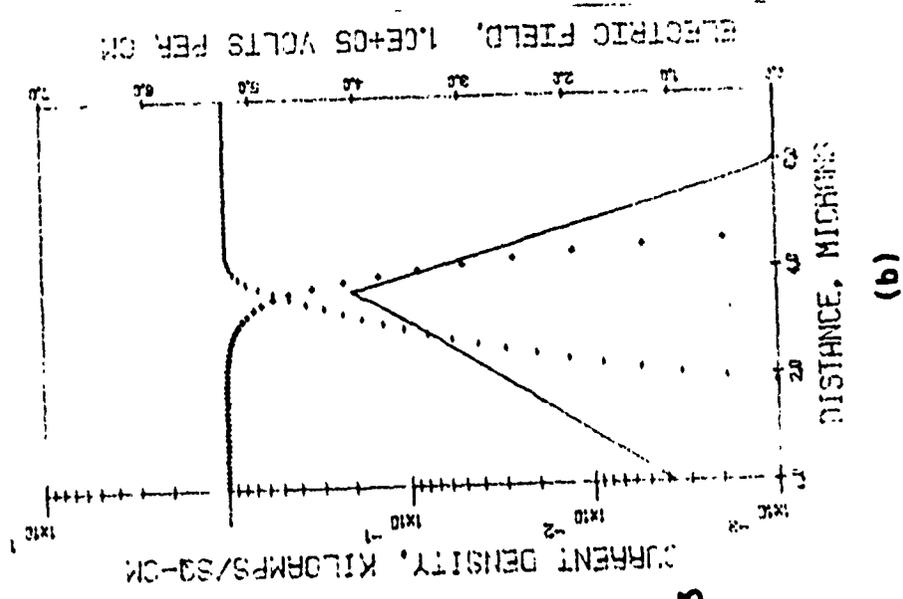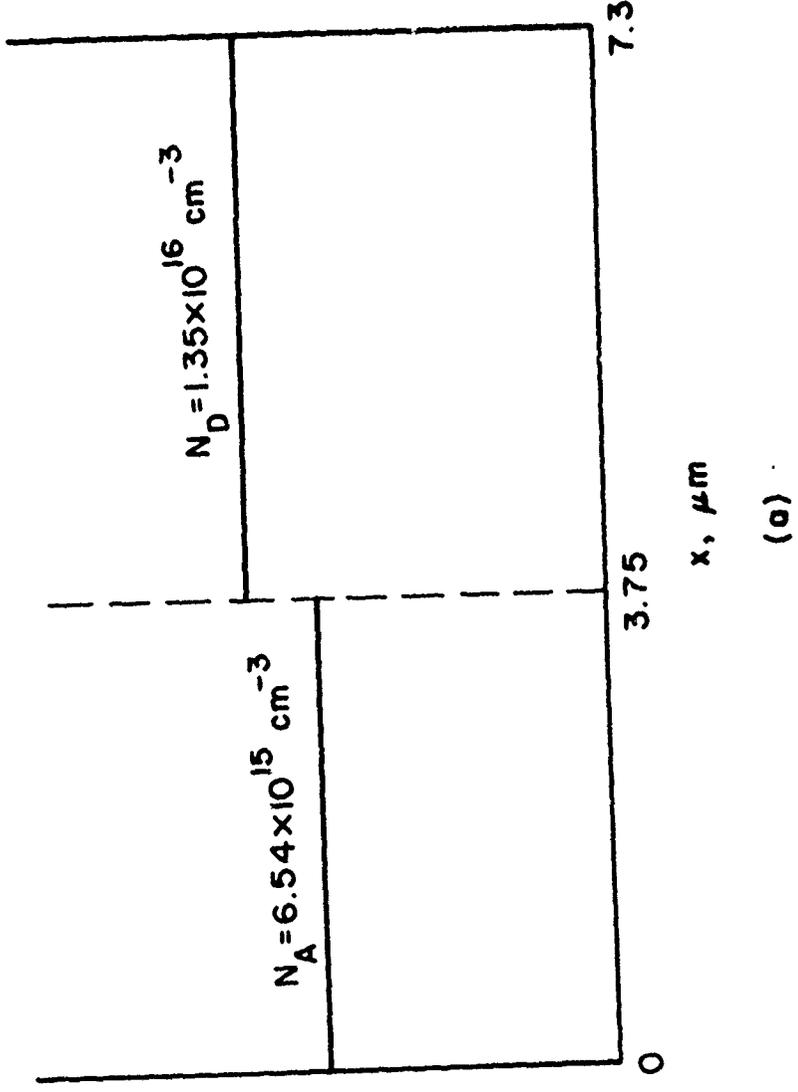
FIG. 25 (a) DOPING PROFILE WHICH REALIZES THE DC FIELD DISTRIBUTION OF FIG. 24 AND (b) DC SOLUTION

FOR T = 500°K AND J_{dc} = 1000 A/cm².

Table 7

Large-Signal Results for the Double-Drift Diode of Fig. 25a

with $T = 500°K$

f (GHz)	V_{RF} (V)	V_{dc} (V)	P_{RF} (kW/cm^2)	η (Percent)	G ($\mho$/cm^2)	B ($\mho$/cm^2)	J_{dc} (A/cm^2)
9.0	70.0	116	18.8	16.07	-7.674	98.14	1010
10.0	70.0	117	17.733	15.47	-7.238	112.88	984
10.0	65.0	119	18.118	15.43	-8.577	111.14	986
10.0	60.0	122	17.568	14.76	-9.76	109.7	979

DOUBLE DRIFT

VRF=70.

JDC=980. A/CM**2

FREQUENCY = 9.0 GHZ
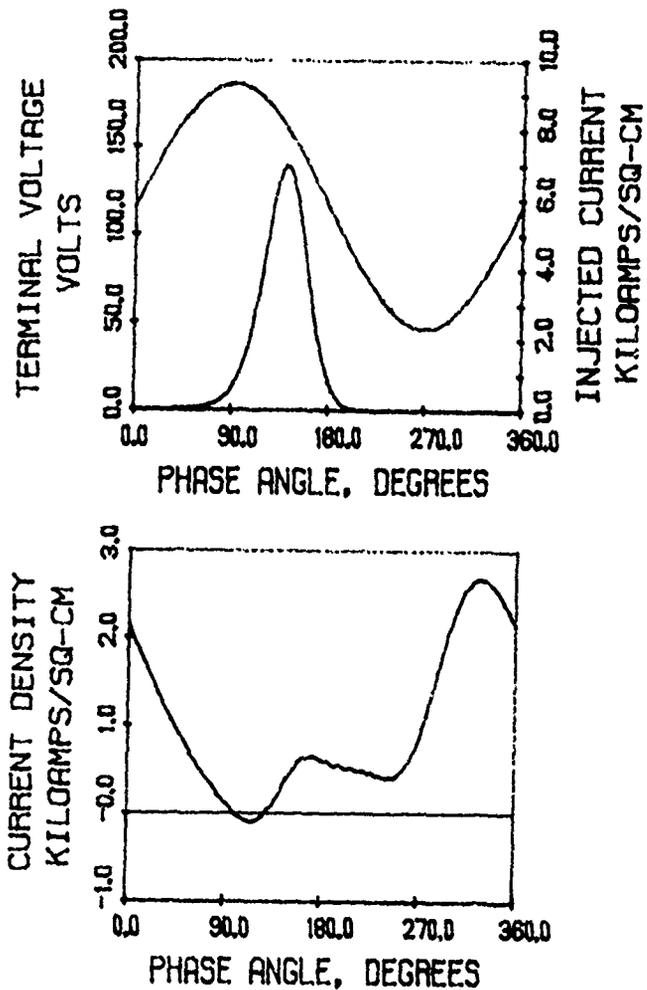
FIG. 26   LARGE-SIGNAL SOLUTION FOR THE DOUBLE-DRIFT DIODE

OF FIG. 25a AT T = 500°K YIELDING 16.07-PERCENT

EFFICIENCY.

PHASE = 277.20 DEGREES

ELECTRIC FIELD, 1.0E+05 VOLTS PER CM

DISTANCE, MICRONS

(b)

CURRENT DENSITY, KILOAMPS/SQ-CM

PHASE = 180.00 DEGREES

ELECTRIC FIELD, 1.0E+05 VOLTS PER CM

DISTANCE, MICRONS

(a)

PARTICLE DENSITY PER CUBIC CM

FIG. 27 DIODE STATE AT TWO TIMES DURING THE RF CYCLE OF FIG. 26.

-57-
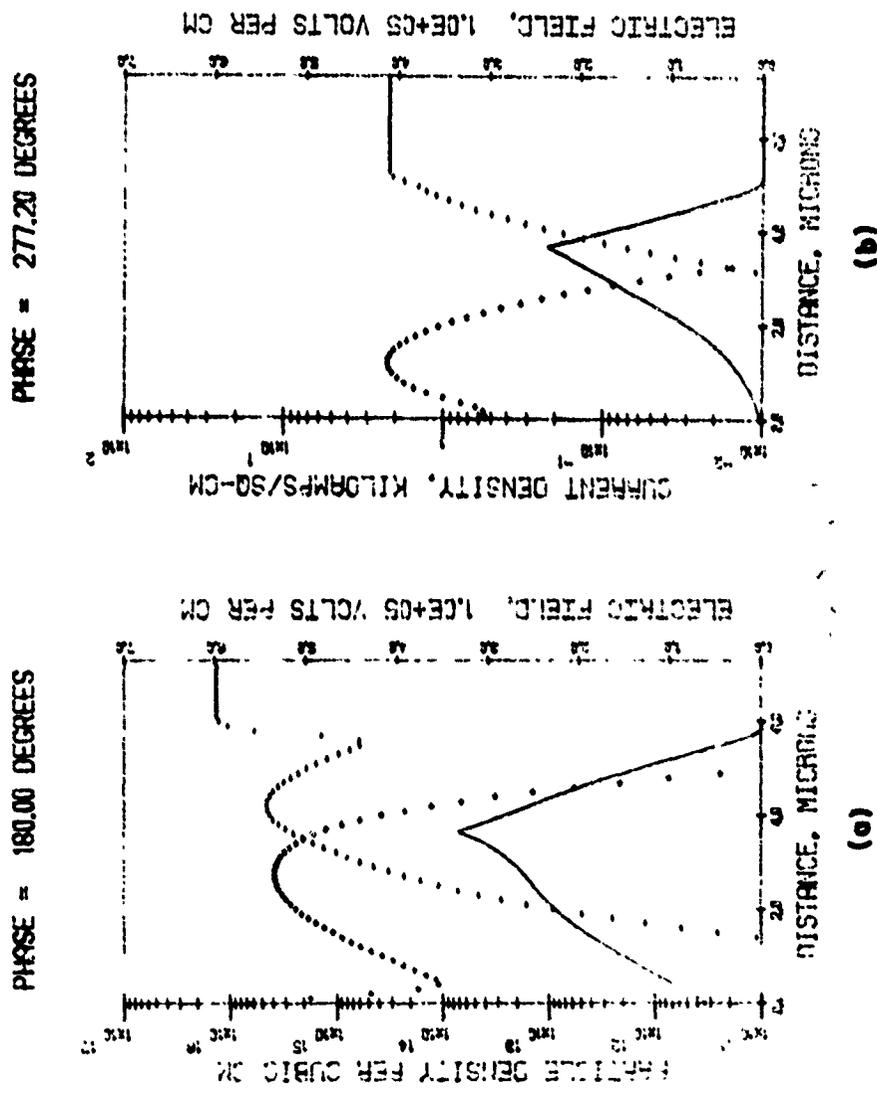
current is offset by a negative current brought about by the inward movement of the depletion edge on the n-side. Hence the terminal current near 180 degrees is not very large. Near 270 degrees the electron pulse is collected in the undepleted region while the hole pulse continues drifting to the left as shown in Fig. 27b. The large terminal current between 270 and 360 degrees in Fig. 26 is brought about by both the outward movement of the depletion edge on the n-side and the movement of holes on the p-side. The current due to the depletion-edge movement has a large capacitive component but it is not entirely capacitive since the previously collected electron pulse is also being extracted. As with the one-sided uniformly doped GaAs structure, the doping on the n-side of double-drift, uniformly doped diodes is too large to achieve greater than saturated velocities.

4.2 Hybrid Double-Drift Structures. This section considers double-drift GaAs IMPATTs which are uniformly doped on the p-side with a high-low (or low-high-low) profile on the n-side. It is not possible to simply append a uniformly doped p-side onto a doping profile that has been optimized for a one-sided GaAs IMPATT. This is because adding the p-side significantly widens the avalanche region, thereby lowering the peak electric field at the junction; hence, the electric field profile on the n-side is quite different from the one-sided case if the same profile is used in a hybrid structure.

The approximate analysis developed in Section 2 can be used to design hybrid structures. First, however, the dc program must be run at the expected temperature and dc current density of operation in

order to approximately determine the maximum electric field. Also, an estimate must be made of the positions of the electron and hole pulse maxima at 180 degrees in the RF cycle either through experience running the large-signal program for similar structures in the frequency range of interest or from an analytical expression for the injection angle. Further, the value of E_{to}, or the electric field at the beginning of the drift region, must be assumed; initially it will be taken as approximately 1.8×10^5 V/cm. The procedure is then to optimize the structure such that the proper transit times are obtained for both carriers. On the n-side the electron pulse is precollected due to the inward movement of the depletion edge, much like the mode of operation in one-sided precollection diodes. Therefore the electron transit time on the n-side should be approximately 0.25 T. (As previously, the electron transit time in the approximate analysis is defined as the time interval between injection at half-cycle and the instant the injected electron meets the depletion edge on the right-hand side.) On the p-side, the hole pulse is collected in the normal IMPATT mode; optimum efficiency is obtained when the hole transit time is approximately 0.4 T.

Figure 28a shows a hybrid doping profile designed to be nonpunch through during the entire RF cycle; Fig. 28b shows the dc solution for J_{dc} = 1500 A/cm^2 and T = 500°K. It will be recalled that for the one-sided case the threshold dc current density for precollection at 10 GHz was approximately 1000 A/cm^2. However, for the hybrid structure the avalanche region width is considerably wider and hence the generated electron pulse is wider. Therefore a higher J_{dc} is necessary so that the height of the electron pulse
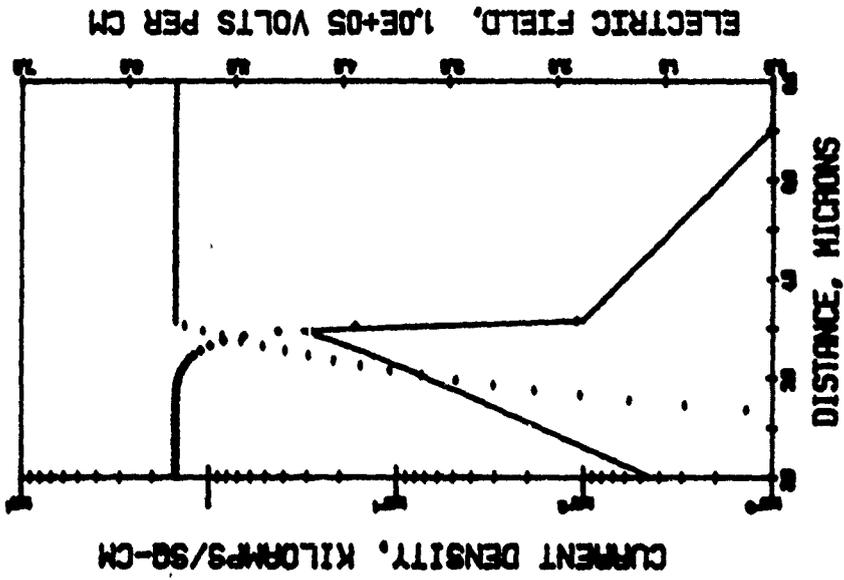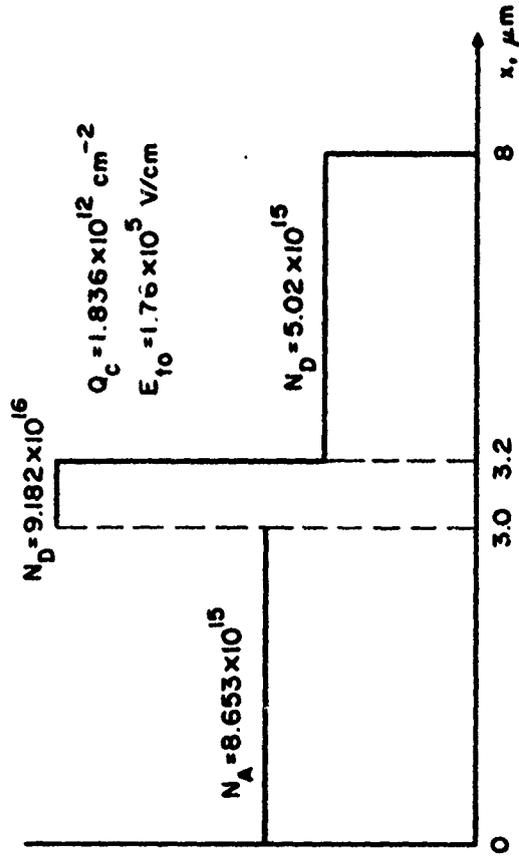
FIG. 28 (a) HYBRID DOPING PROFILE DESIGNED FOR 10-GHz OPERATION AND (b) DC SOLUTION

AT T = 500°K AND J_{dc} = 1500 A/cm².

is greater than the background doping at the point of precollection, which raises the field in front of the pulse and results in more efficient collection of the pulse. The broader generated pulses and higher required J_{dc}, as well as the presence of the p-side where precollection does not occur, reduce the efficiencies obtained from hybrid structures below those obtained with one-sided precollection mode IMPATTs.

If the maximum dc electric field profile from running the dc program is approximately known (and the hole and electron positions at 180 degrees from large-signal runs are known), the approximate analysis can be used to determine the dimensions of Fig. 28a for 10-GHz operation as follows. A 10-GHz RF voltage waveform of amplitude $V_{dc}/2$ is impressed across the device and the lengths are adjusted until the proper transit times are obtained for the injected hole and electron, i.e., approximately 40 ps and 25 ps, respectively. The electric field on the left-hand side is set to 0.25 E_{max} during the adjustments. It was found that the dimensions of Fig. 28a yielded a hole transit time of 36 ps and an electron transit time of 25 ps.

Figure 29 shows terminal waveforms for the most efficient RF solution obtained at 10 GHz with $\eta = 18.72$ percent. The V_{RF}/V_{dc} ratio for this solution was 0.6, whereas 0.5 optimum voltage modulation was assumed in the approximate analysis. It is seen that there is a significant terminal current flowing during the first half-cycle. To see why this is the case, Fig. 30 shows the electric field and particle concentrations at two points in the cycle, 306 degrees and 0 degrees (or 360 degrees). In Fig. 30a the electric field reaches a
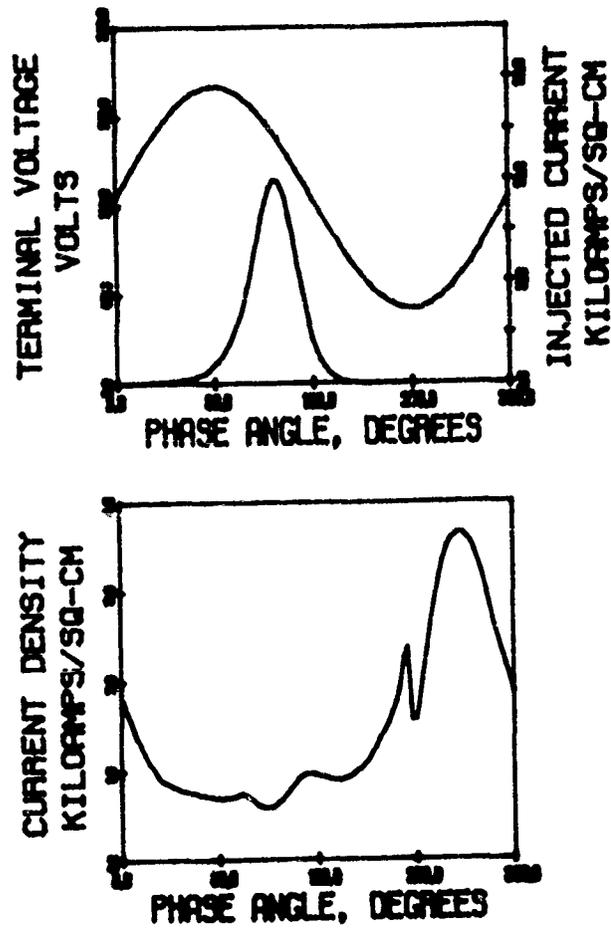
FIG. 29   LARGE-SIGNAL SOLUTION FOR THE DIODE OF FIG. 28a

AT T = 500°K WITH η = 18.72 PERCENT, V_{RF} = 62.5 V,

J_{dc} = 1470 A/cm^2, V_{dc} = 104 V, G = - 14.73 $\mho$/cm^2,

B = 98.12 $\mho$/cm^2 AND f = 10 GHz.
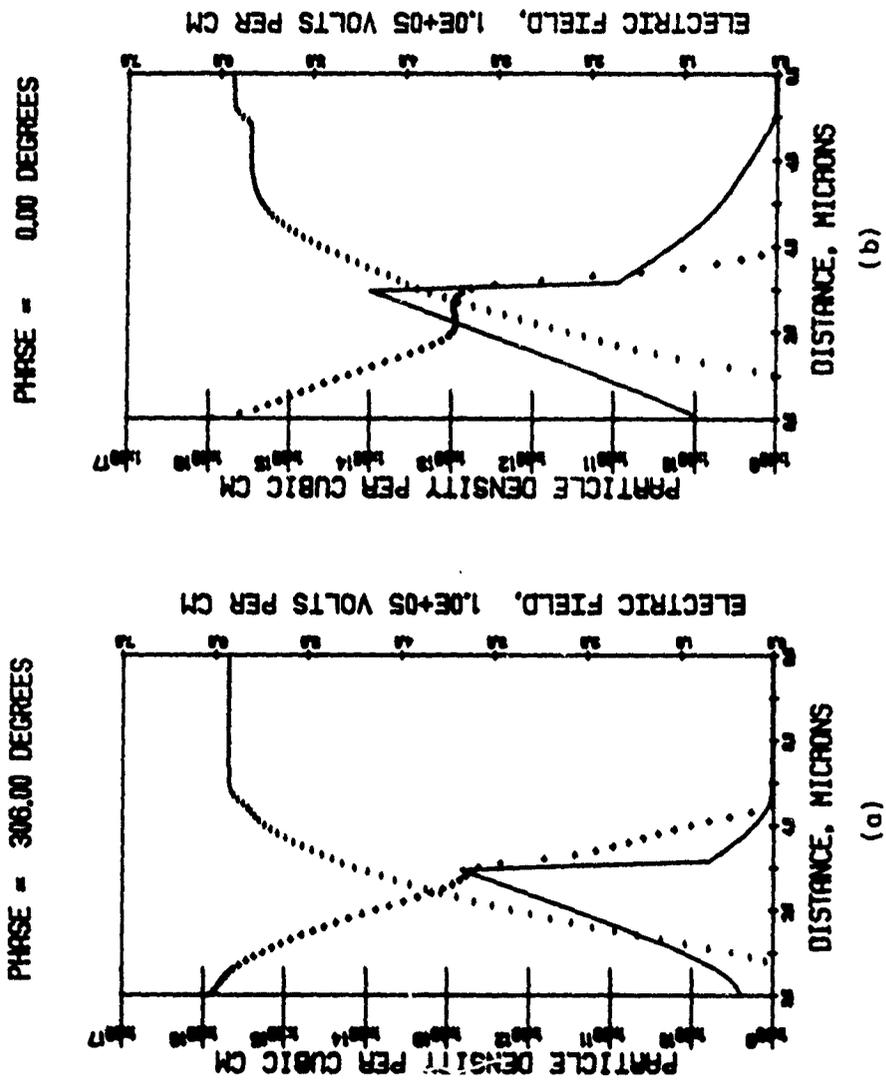
FIG. 30   DIODE STATES AT TWO DIFFERENT TIMES DURING THE RF SOLUTION OF FIG. 29.

small constant value in the undepleted region at approximately 4.75 μm; in Fig. 30b the depletion edge is at 7 μm. The time interval corresponding to this depletion edge movement is $(360 - 306)$ x T/360, or 15.0 ps. Therefore the average velocity of the depletion edge during this time interval is 1.50×10^7 cm/s, which is 50 percent greater than the peak electron velocity. At 306 degrees the electric field in the undepleted region is 2.34 kV/cm which corresponds to an electron velocity of 8.67×10^6 cm/s. Hence the "knee" of the electric field is moving considerably faster than the electrons. For this reason many electrons are left behind in a high field region where they are extracted at saturated velocity. This effect is brought about by the increased space charge in the device. Since the threshold dc current density for efficient precollection is now approximately 1500 A/cm^2 rather than 1000 A/cm^2 for the previous one-sided case, the width of the depleted region on the n-side is increased; therefore, the depletion edge must move faster to cover a longer distance in the same time period. One way to reduce the current during the first half-cycle is to reduce E_{to} for the dc solution of Fig. 28b which is accomplished by increasing the doping in the "high" region on the n-side in Fig. 28a, as in the doping profile of Fig. 31a. Figure 31b shows the dc solution with $J_{dc} = 1500$ A/cm^2 and T = 500°K for this case. It is seen that the depletion edge is now at 6.3 μm instead of 7.0 μm for the previous case. Figure 32 shows the most efficient solution obtained for this structure at 10 GHz. Although the terminal current during the first half-cycle is somewhat reduced, the efficiency is reduced because the voltage modulation is now only 0.477. The fact that

-64-
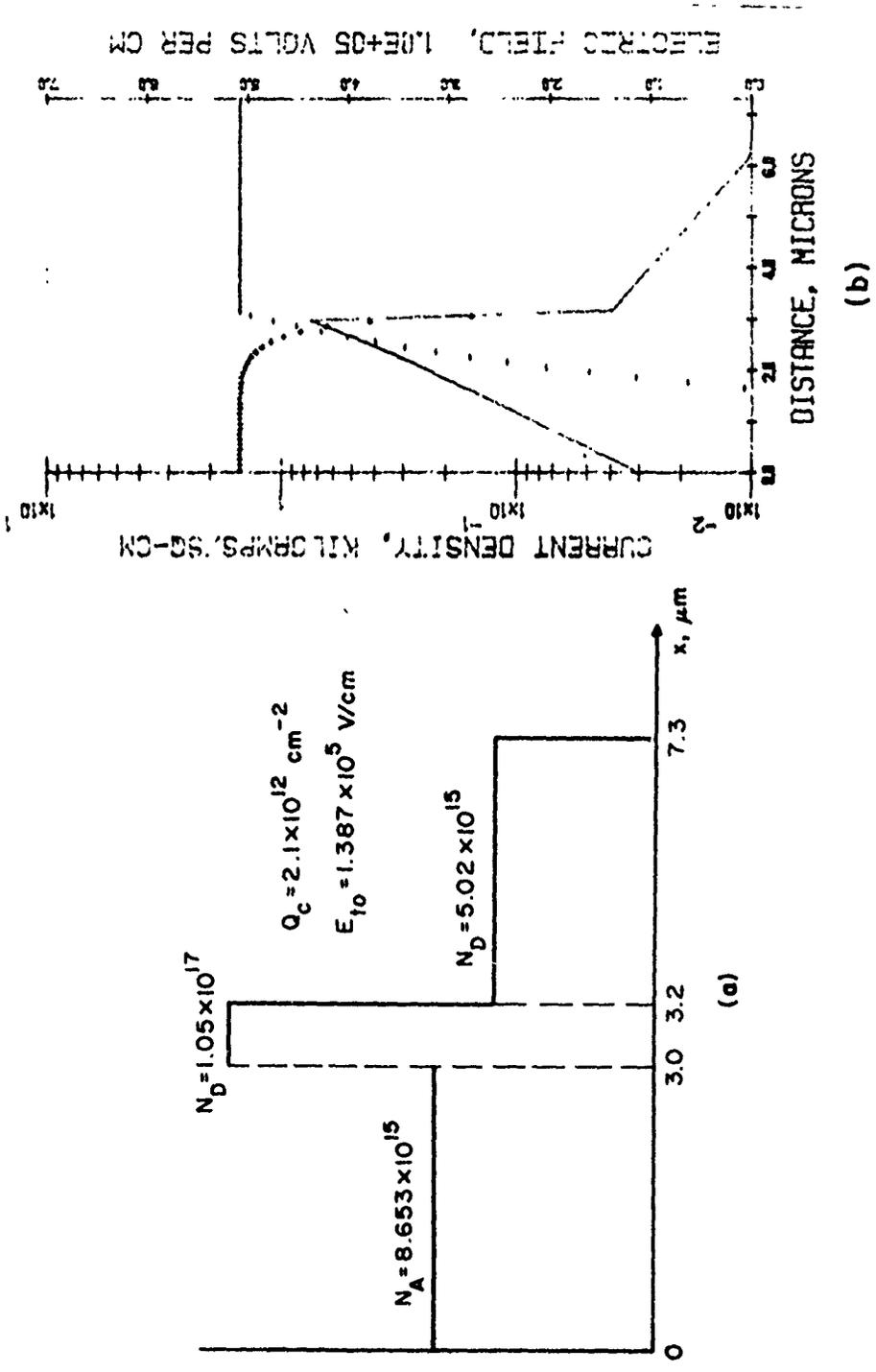
FIG. 31 (a) DOPING PROFILE WITH REDUCED E_{to} AND (b) DC SOLUTION AT

$T = 500°K$ AND $J_{dc} = 1500$ A/cm^2.

DOUBLE DRIFT

VHF=46.0

JDC=1500. A/CM**2

FREQUENCY = 10.0 GHZ
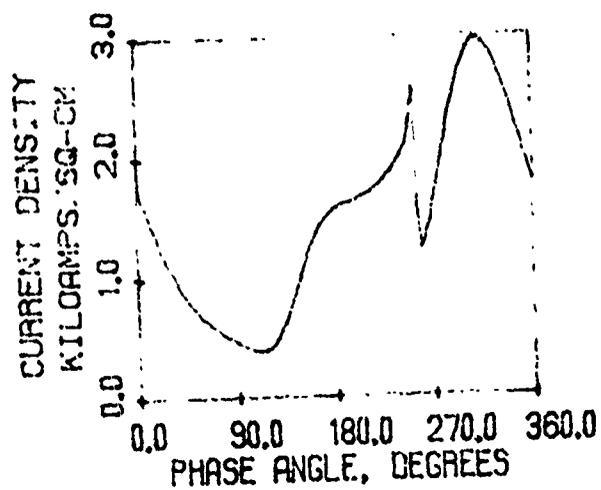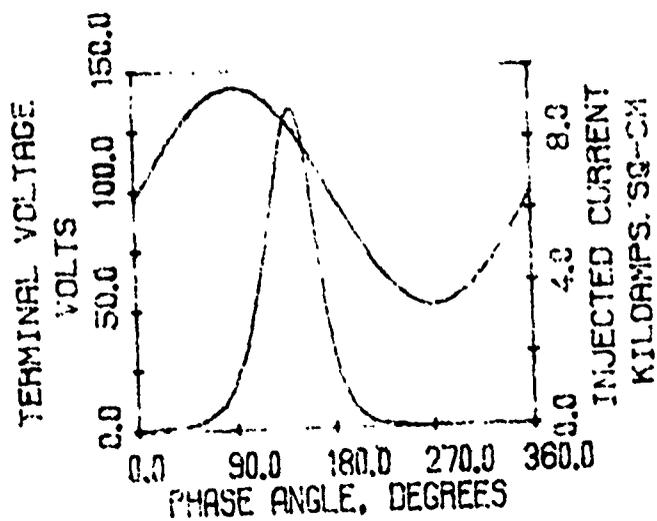
FIG. 32 LARGE-SIGNAL SOLUTION FOR THE DIODE OF FIG. 31a AT

T = 500°K YIELDING η = 15 PERCENT WITH V_{dc} = 96.5 V,

G = - 20.547 ʊ/cm² AND B = 101.14 ʊ/cm².

V_{RF}/V_{dc} decreases with E_{to} is intuitively expected, as previously discussed for the one-sided case; this is because reducing E_{to} reduces the RF swing of the entire electric field profile, but the dc field profile is only affected in the drift region on the n-side. Therefore the RF voltage decreases faster than the dc voltage, as is seen by comparing Figs. 29 and 32.

To increase the efficiency, the diode of Fig. 28a can simply be made shorter, and hence punched through, so that the transit time is shorter for any carriers that are extracted at saturated velocity. In Fig. 33a, the length has been reduced to 6.0 µm; Fig. 33b shows the dc solution for this structure with J_{dc} = 1500 A/cm² and V_{dc} = 117.6 V. The optimum RF solution for this structure at 10 GHz resulted in η = 22.49 percent, V_{RF} = 61.0 V, V_{dc} = 101 V, J_{dc} = 1450 A/cm², G = - 17.8, and B = 106.5 ℧/cm².

To further increase the effic y, E_{to} may be increased, which is accomplished by reducing the magnitude of the highly doped region on the n-side in Fig. 33a. However, it is expected that increasing E_{to} will result in a greater back-bias effect, as was the case for the one-sided structures. Figure 34a shows a doping profile designe so that E_{to} = 2.23 x 10⁵ V/cm; an equivalent Gaussian doping spike for the highly doped region with half-width 0.035 µm would have a maximum value of 4.05 x 10¹⁷ and would be located about x = 3.1 µm. Figure 34b shows the dc solution with J_{dc} = 1500 A/cm² and V_{dc} = 130 V. Table 8 presents the results of RF simulations of this structure at T = 500°K, and Fig. 35 shows the most efficient solution obtained at 10 GHz. As expected, the V_{RF}/V_{dc} ratio is larger than before, equal to 0.72. Also the current in the first half-cycle
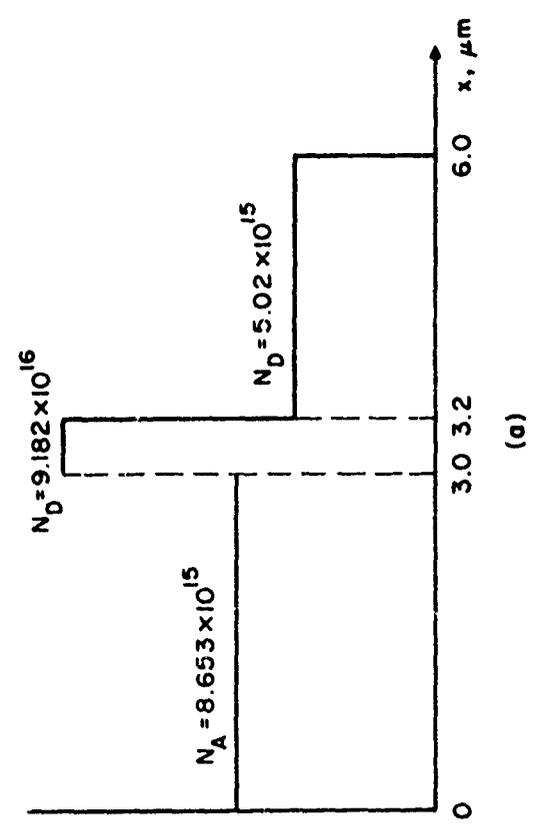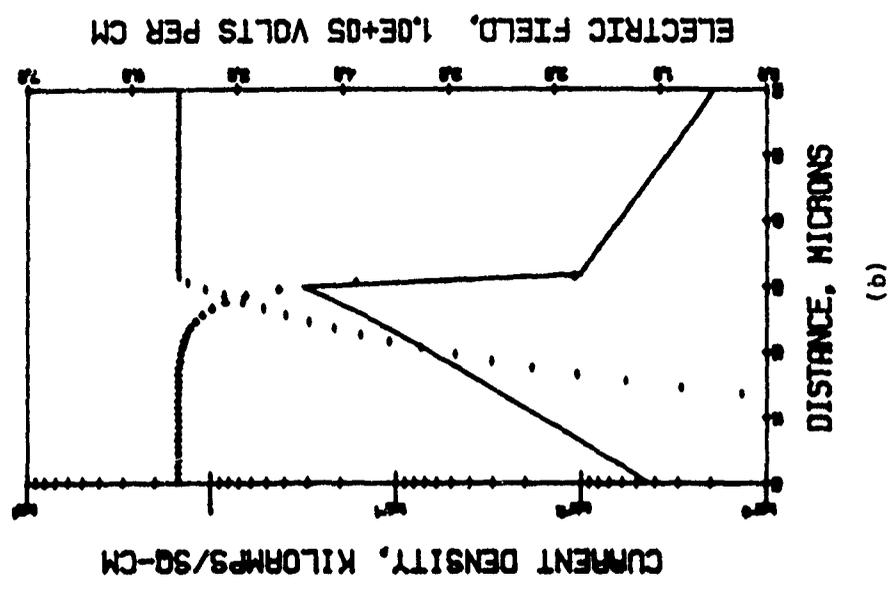
FIG. 33 (a) HYBRID DOPING PROFILE WITH SHORTER LENGTH ON THE n-SIDE AND (b) DC SOLUTION

FOR T = 500°K AND J_{dc} = 1500 A/cm^2.
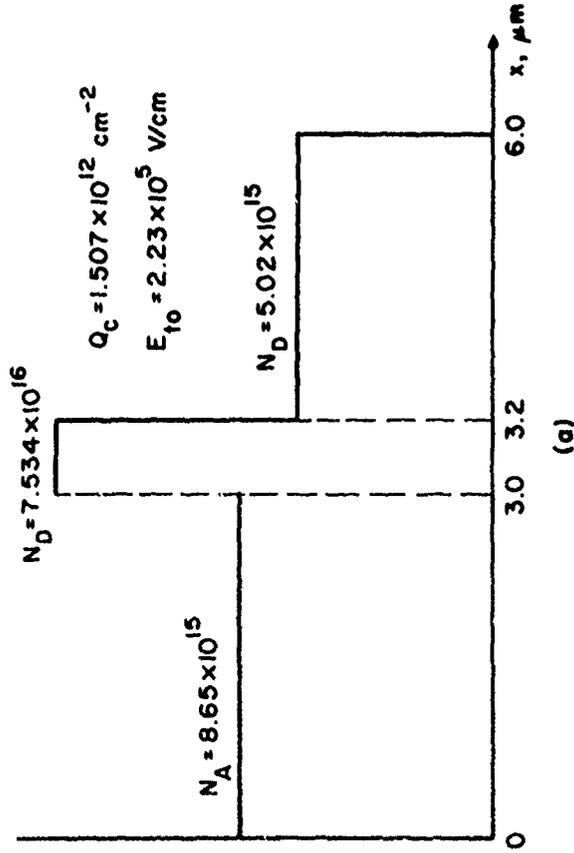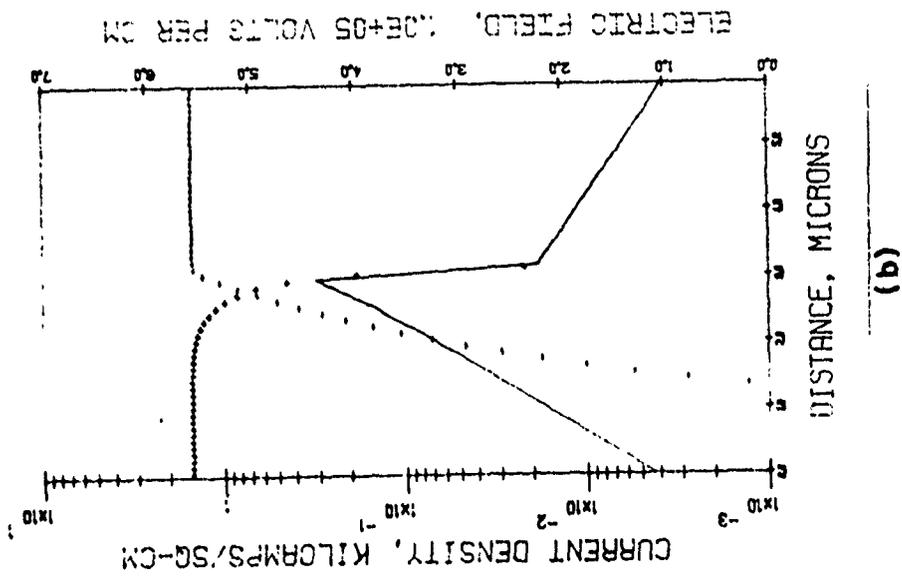
FIG. 34 (a) HYBRID DOPING PROFILE WITH REDUCED DOPING IN THE HIGHLY DOPED REGION SO THAT E_{to} IS INCREASED AND (b) DC SOLUTION AT $T = 500°K$ AND $J_{dc} = 1500$ A/cm^2.

Table 8

Large-Signal Results for the Hybrid Structure of Fig. 34a

with T = 500°K

V_{RF} (V)	G (℧/cm²)	B (℧/cm²)	η (%)	V_{dc} (V)	J_{dc} (A/cm²)	P_{RF} (W/cm²)	f (GHz)
10	-55.621	62.701	1.43	129	1500	2.7806×10^3	10
20	-44.376	83.96	4.61	128	1500	8.8745×10^3	10
30	-34.897	94.484	8.24	127	1510	15.703×10^3	10
40	-28.047	100.13	11.98	124	1510	22.436×10^3	10
50	-23.407	103.35	15.86	122	1520	29.257×10^3	10
60	-19.624	105.86	19.76	118	1510	35.321×10^3	10
70	-16.155	107.66	23.52	112	1500	39.577×10^3	10
76	-14.921	108.93	27.61	108	1450	43.089×10^3	10
77	-14.587	109.23	27.67	107	1460	43.241×10^3	10
78	-14.301	109.49	27.16	107	1500	43.501×10^3	10
79	-13.824	109.96	26.90	107	1500	43.135×10^3	10
80	-13.645	110.0	26.59	106	1540	43.661×10^3	10
82	-12.118	111.65	25.51	106	1510	40.739×10^3	10
84	-10.347	113.38	23.36	105	1490	36.502×10^3	10
86	- 9.0035	114.36	20.57	104	1550	33.293×10^3	10
88	- 5.7764	117.36	14.38	103	1510	22.365×10^3	10
89		-263.4					
77	-15.14	100.98	27.75	107	1510	44.88×10^3	9.5
77	-15.094	115.93	26.98	107	1540	44.742×10^3	10.5
77	-15.074	93.233	27.18	108	1530	44.684×10^3	9

DOUBLE DRIFT

VRF=77.

JDC=1460. A/CM**2

FREQUENCY = 10.0 GHZ
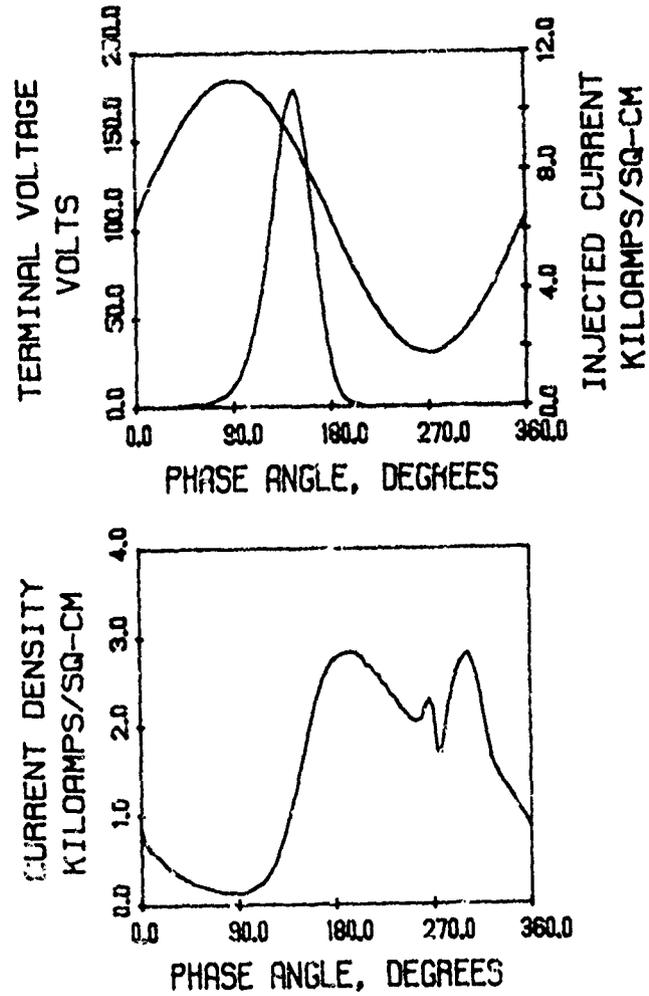
FIG. 35   LARGE-SIGNAL SOLUTION FOR THE HYBRID STRUCTURE

OF FIG. 34a AT T = 500°K YIELDING η = 27.67 PERCENT.

-71-

is significantly reduced due to the shorter length of the device. Figure 36 shows the results for $f = 10$ GHz and $T = 500°K$ plotted as a function of V_{RF}. The negative conductance curve of Fig. 36a decreases monotonically, whereas the negative conductance curve of Fig. 12a has a local maximum near the maximum efficiency point. Therefore these results indicate that it would be easier to operate the double-drift diode as an oscillator at the maximum efficiency point than the single-drift diode. The monotonically decreasing character of the conductance for the double-drift diode is due to the presence of the p-layer. In Fig. 36b it is seen that the dc operating voltage drops by almost 20 percent from the dc value. This is worth noting since the device heats up considerably for small V_{RF}, where the efficiency is much less and the dc power is increased.

In the doping profile of Fig. 37a, the doping in the highly doped region is further reduced so that E_{to} is increased to 2.68×10^5 V/cm. The equivalent Gaussian doping spike for this case would have a maximum value of 3.167×10^{17} cm^{-3}. Figure 37b presents the dc solution for $J_{dc} = 1500$ A/cm^2, $T = 500°K$ and $V_{dc} = 141.6$ V. Table 9 presents the results of the large-signal simulations for $f = 10$ GHz and $T = 500°K$; it is seen that by increasing E_{to}, the maximum large-signal efficiency is increased to over 29 percent. The V_{RF}/V_{dc} ratio is now 0.81 at maximum efficiency compared to 0.72 for the previous case with smaller E_{to}. The dc operating voltage drops approximately 20 percent from $V_{RF} = 0$ to $V_{RF} = 92$ V, as seen in Fig. 38b; Fig. 38a shows that the high-efficiency mode has become more critical for this structure, that is the efficiency curve is more peaked and the negative conductance curve is starting to increase near the maximum
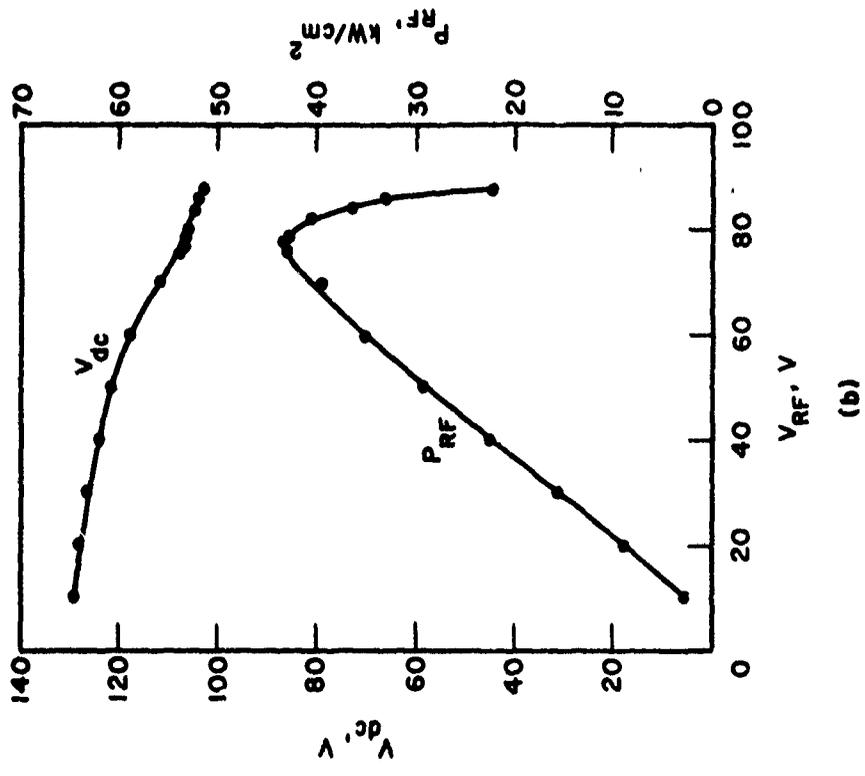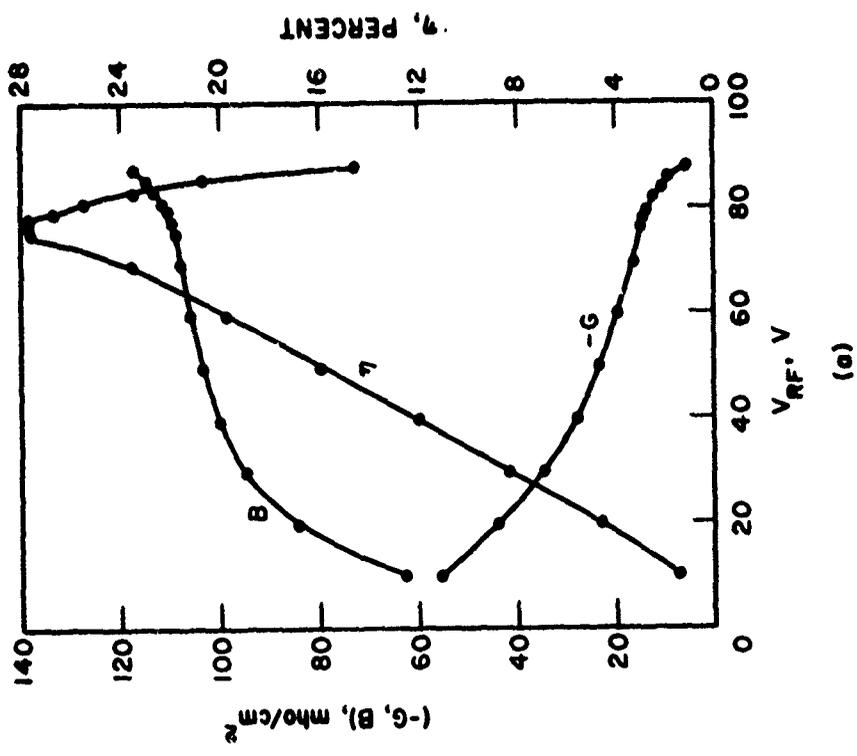
FIG. 36 LARGE-SIGNAL RESULTS FOR THE HYBRID STRUCTURE OF FIG. 34a AT T = 500°K,

$f = 10$ GHz, AND $J_{dc} \approx 1500$ A/cm^2.
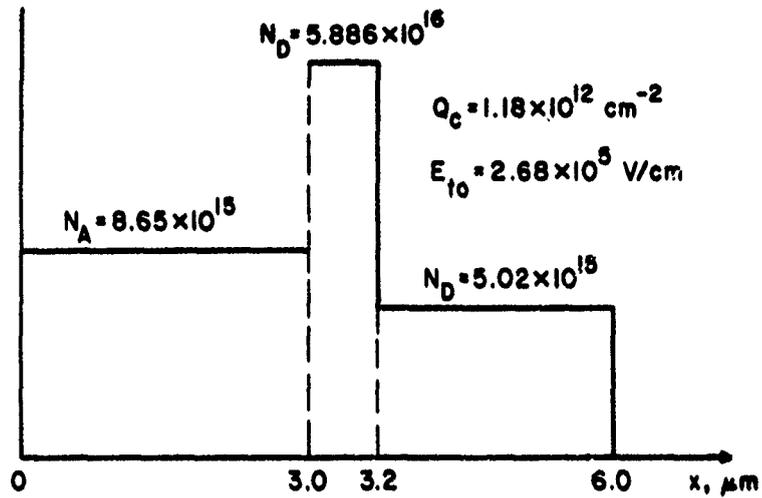
(a)
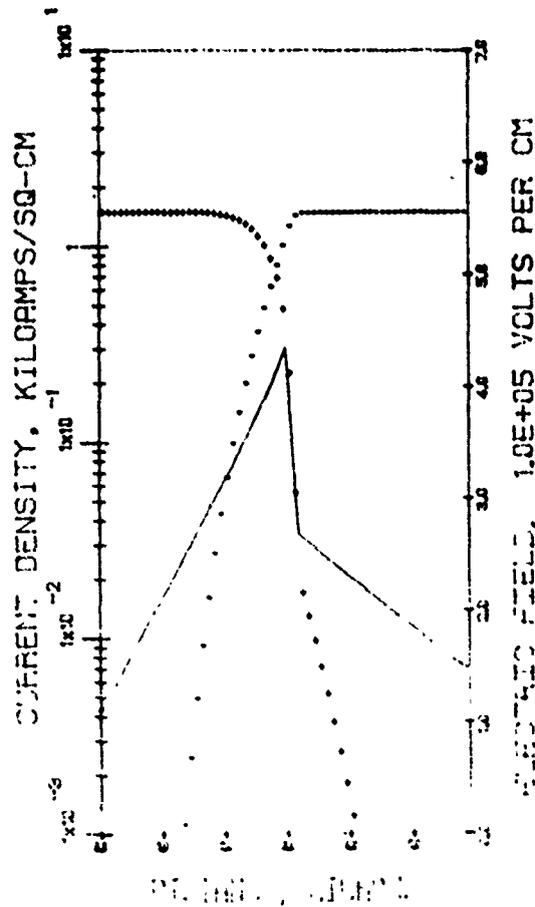
(b)

FIG. 37 (a) HYBRID DOPING PROFILE WHICH FURTHER INCREASES E_{to} AND

(b) DC SOLUTION AT T = 500°K AND J_{dc} = 1500 A/cm^2.

Table 9

Large-Signal Results for the Diode of Fig. 37a

at $T = 500°K$ and $f = 10$ GHz

V_{RF} (V)	G ($\mho/cm^2$)	B ($\mho/cm^2$)	η (%)	V_{dc} (V)	J_{dc} (A/cm^2)	P_{RF} (W/cm^2)
10	-56.712	62.006	1.34	141	1500	2.8351×10^3
20	-44.932	83.553	4.27	140	1500	8.9854×10^3
30	-35.161	94.36	7.61	138	1500	15.821×10^3
40	-28.585	99.703	11.05	136	1520	22.867×10^3
50	-23.558	103.25	14.56	133	1520	29.446×10^3
60	-19.52	105.95	18.06	130	1500	35.135×10^3
70	-16.522	107.94	21.43	126	1500	40.478×10^3
80	-14.15	109.41	24.69	121	1520	45.276×10^3
85	-13.078	110.2	25.55	118	1570	47.241×10^3
87	-12.272	110.86	25.77	117	1550	46.44×10^3
88	-11.616	111.47	25.85	116	1500	44.974×10^3
89	-12.035	110.98	26.19	115	1580	47.663×10^3
90	-11.535	111.5	26.52	114	1540	46.715×10^3
91	-11.49	111.81	29.00	113	1460	47.572×10^3
91	-11.69	111.45	28.10	113	1530	48.401×10^3
92	-11.832	111.46	29.08	113	1530	50.071×10^3
93	-10.689	112.55	28.11	112	1470	46.224×10^3
94	- 9.954	113.28	26.52	111	1490	43.974×10^3
95	- 9.65	113.56	26.25	111	1490	43.545×10^3
96	- 8.7767	114.17	23.83	110	1540	40.441×10^3
98	- 5.8704	116.65	17.44	109	1490	28.188×10^3
99	- 1.4408	120.12	4.68	105	1430	7.06×10^3
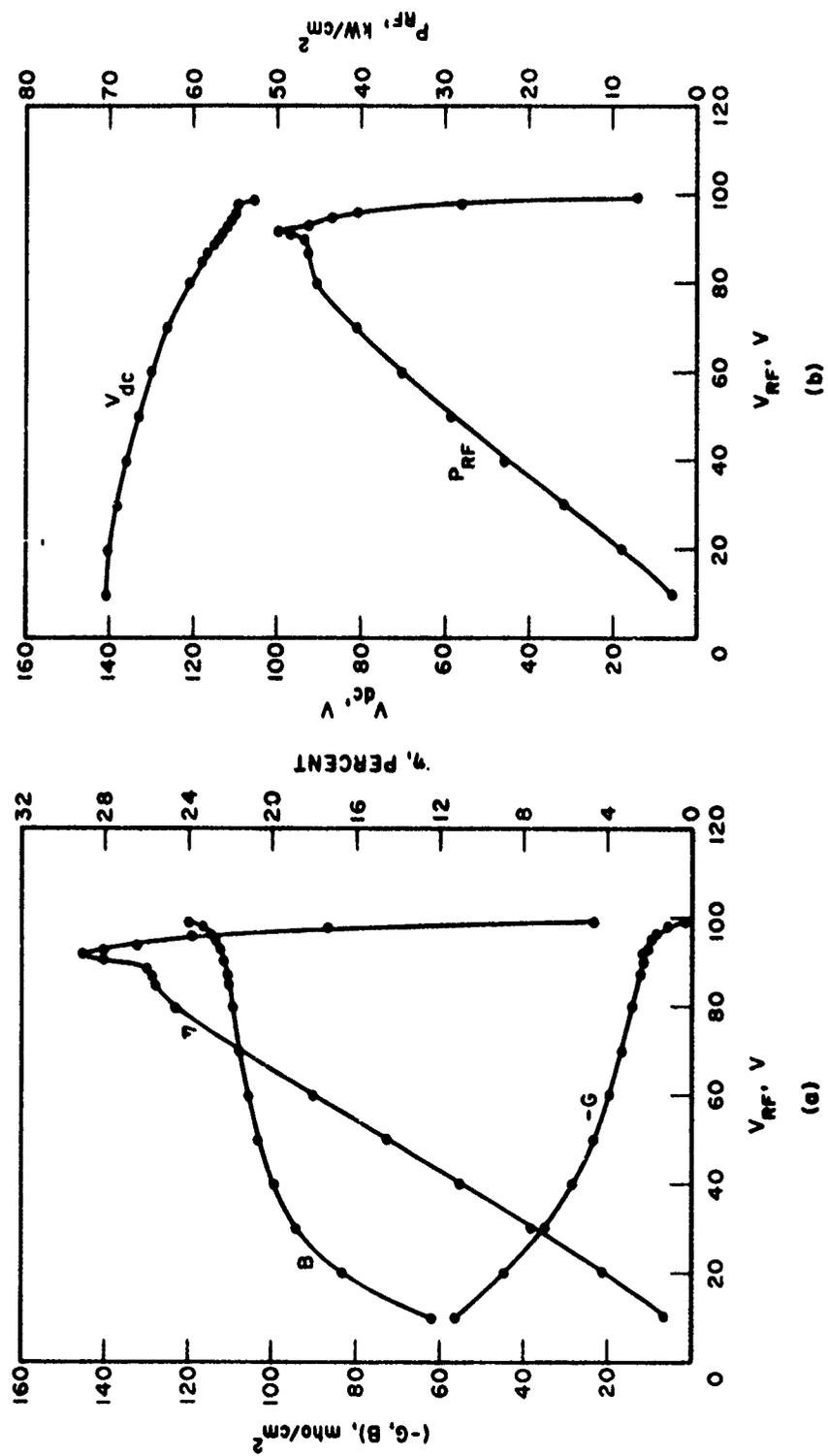
FIG. 38 LARGE-SIGNAL RESULTS FOR THE HYBRID STRUCTURE OF FIG. 37a AT T = 500°K, f = 10 GHz

AND $J_{dc} \approx 1500$ A/cm^2.

efficiency point. Therefore it appears that further increase of E_{to} will not be advantageous. Figure 39 shows the diode waveforms for the large-signal solution for which 29.0-percent efficiency was obtained. The dip in the current near 270 degrees is brought about by the inward movement of the depletion edge as it comes to meet the electron pulse. The large RF voltage modulation possible for this structure results in higher efficiency than for the previous hybrid double-drift structures.

The effect of varying the uniform doping on the p-side in hybrid structures is examined next. Previously, the doping was set so that at dc the electric field at the left-hand boundary was approximately one-fourth the maximum electric field value. It is not clear what would happen if the doping were increased resulting in a lower field at the left-hand side. The avalanche width would be decreased which should be beneficial; on the other hand a portion of the p-layer may become undepleted during the RF cycle which would introduce loss due to the low mobility for holes.

Figure 40a shows a doping profile that was simulated to test the effect of N_A; it is identical with the profile of Fig. 34a except for N_A which was set so that the diode is just punched through at dc, as shown in Fig. 40b. For the structure of Fig. 34a, the maximum efficiency obtained was 27.67 percent. Figure 41 shows the waveforms at maximum efficiency for the just punched through structure of Fig. 40a, where $\eta = 24.93$ percent. The results of this large-signal simulation show that much of the p-side is undepleted near 270 degrees in the cycle. Therefore it is desirable to design the p-side to be well punched through at dc.

DOUBLE DRIFT

VRF=91.

JDC=1460. A/CM**2

FREQUENCY = 10.0 GHZ
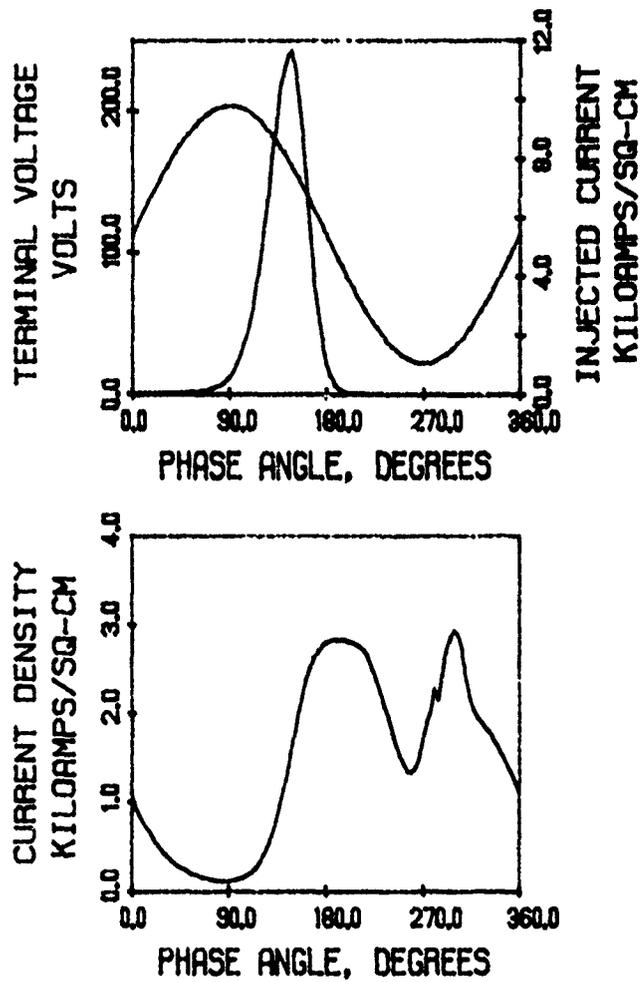
FIG. 39   LARGE-SIGNAL SOLUTION FOR THE HYBRID DIODE OF FIG. 37a

AT T = 500°K YIELDING η = 29.0 PERCENT.
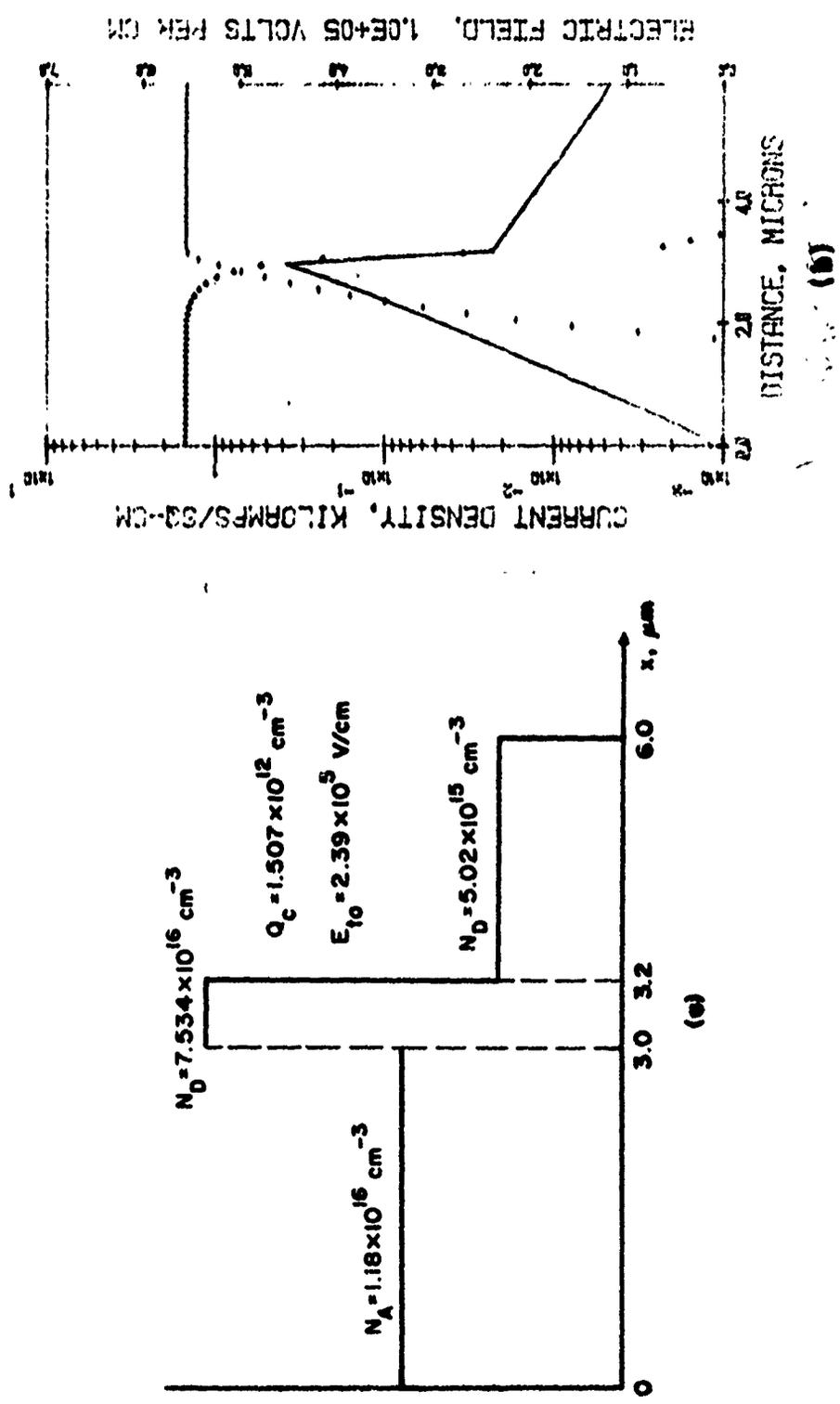
FIG. 40 (a) HYBRID DOPING PROFILE DESIGNED SO THAT THE p-SIDE IS JUST PUNCHED THROUGH AT DC AND (b) DC SOLUTION AT T = 500°K AND J_{dc} = 1500 A/cm².

DOUBLE DRIFT

VRF=77.

JDC=1460. A/CM**2

FREQUENCY = 10.0 GHZ
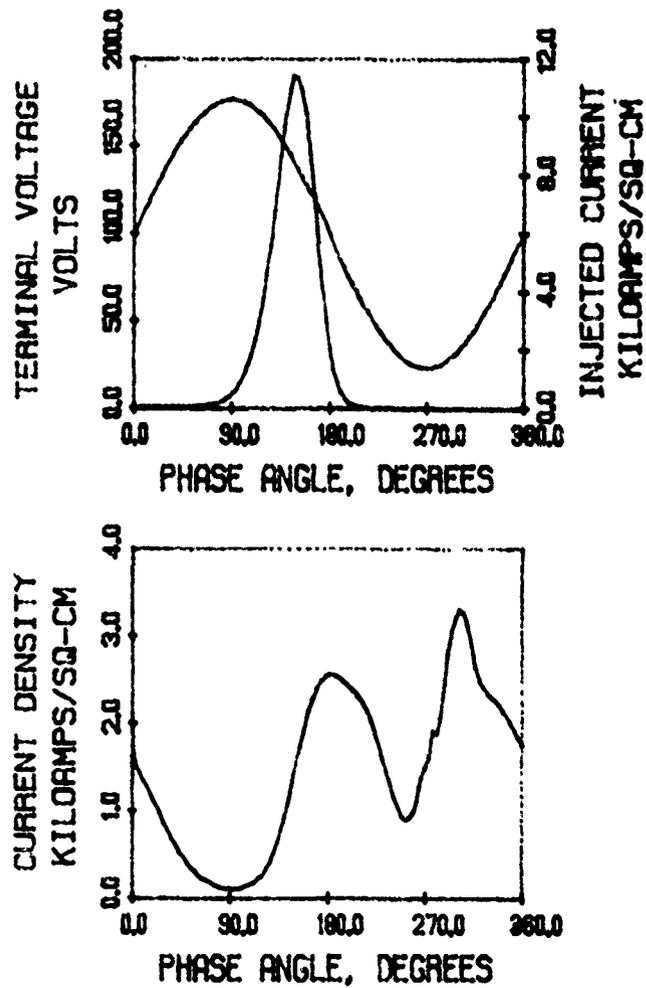
FIR. 41 LARGE-SIGNAL SOLUTION FOR THE STRUCTURE OF FIG. 40a.

(η = 24.93 PERCENT, V_{dc} = 100 V, G = - 12.28 AND

B = 116.9 $\mho$/cm^2)

-80-

Simulations were also carried out for a structure with lower N_A than that of Fig. 34a so that the field on the left-hand side was one-half the maximum electric field at dc. The maximum large-signal efficiency obtained was 27.28 percent, only slightly lower than for the diode of Fig. 34a; however, the range of V_{RF} for which high efficiency is obtained was reduced. These results indicate that designing so that the field on the left-hand side is 0.25 E_{max} at dc is desirable, but this field value is not a critical factor.

4.3 Double-Read Double-Drift Structures. The double-drift diodes considered up to now were uniformly doped on the p-side which resulted in a large avalanche region width. This section considers structures with high-low, Read doping profiles on both sides of the junction. Such a structure can theoretically achieve higher efficiencies than hybrid double-drift IMPATTs.

Figure 42a shows the first double-Read structure that was studied. For this case the highly doped regions on both sides of the junction are equal. The dc solution with J_{dc} = 1250 A/cm^2 and T = 500°K is shown in Fig. 42b. The structure was designed so that E_{to} (field at the beginning of the drift region) is approximately the same on both sides. Also the electric field at the left-hand boundary is designed above the value at the right-hand boundary so that the diode remains punched through on the p-side throughout the entire RF cycle.

Table 10 presents results of large-signal simulations with f = 10 GHz and T = 500°K; it is seen that efficiencies of over 36 percent are obtainable. Figure 43 shows plots of the results vs. RF voltage for the cases with J_{dc} near 1250 A/cm^2. Figure 43a shows

-81-
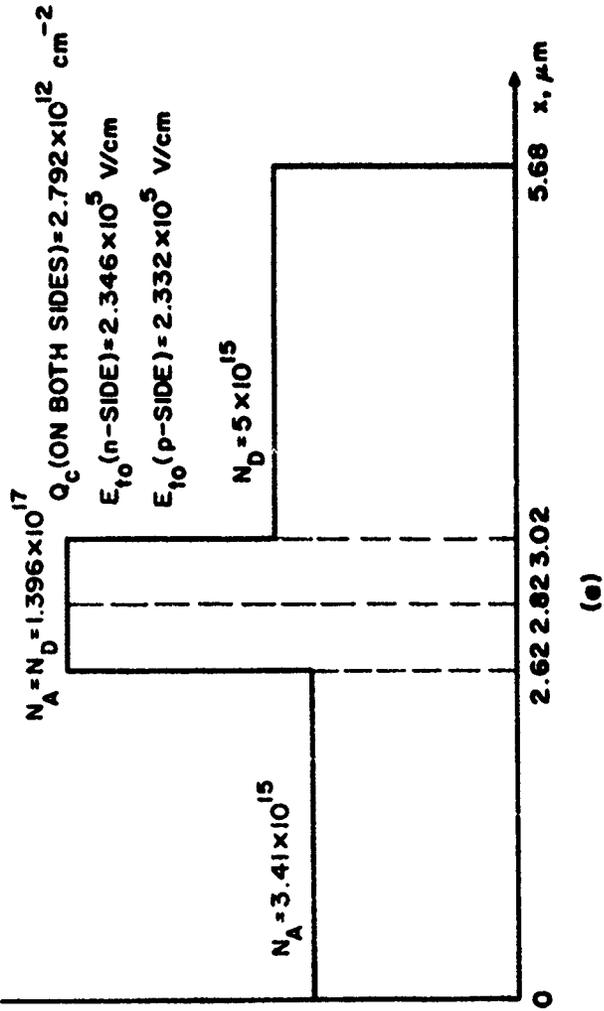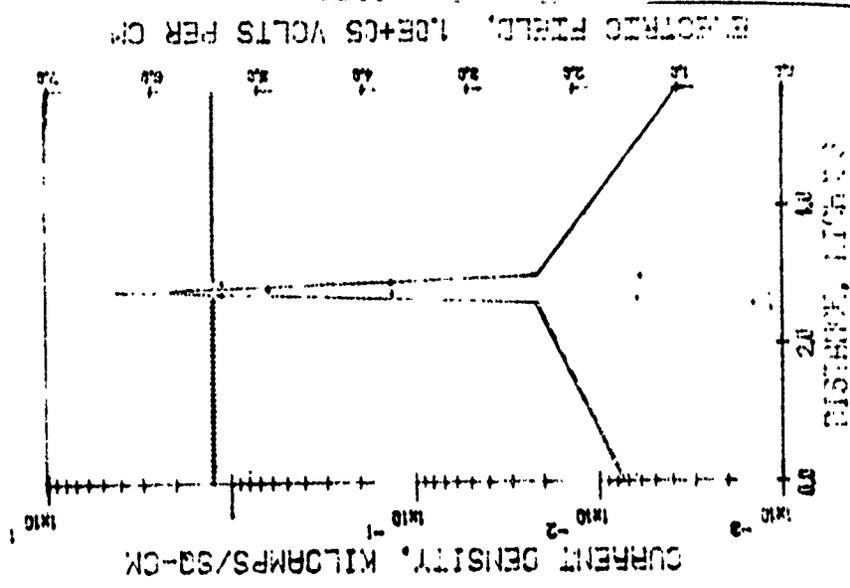
FIG. 42 (a) DOUBLE-READ DOPING PROFILE AND (b) DC SOLUTION AT T = 500°K AND J_{dc} = 1250 A/cm^2.

(b)

ELECTRIC FIELD, 1.0E+05 VOLTS PER CM

CURRENT DENSITY, KILOAMPS/SQ-CM

DISTANCE, MICRONS

$N_A = N_D = 1.396 \times 10^{17}$

Q_c(ON BOTH SIDES) = 2.792 × 10^{12} cm^{-2}

E_{to}(n-SIDE) = 2.346 × 10^5 V/cm

E_{to}(p-SIDE) = 2.332 × 10^5 V/cm

$N_D = 5 \times 10^{15}$

$N_A = 3.41 \times 10^{15}$

x, μm

2.62 2.82 3.02   5.68

(a)

Table 10

Large-Signal Results for the Double-Read Diode of Fig. 42a

with $T = 500°K$ and $f = 10$ GHz

V_{RF} (V)	G ($\mho/cm^2$)	B ($\mho/cm^2$)	η (%)	V_{dc} (V)	J_{dc} (A/cm^2)	P_{RF} (W/cm^2)
10	-58.003	51.029	2.09	112	1240	2.9×10^3
20	-48.057	88.187	6.96	111	1240	9.6112×10^3
30	-37.325	101.32	12.05	110	1260	16.796×10^3
40	-29.556	107.9	17.27	109	1260	23.644×10^3
50	-23.779	111.77	22.55	107	1240	29.723×10^3
60	-19.9	113.85	27.70	104	1240	35.818×10^3
65	-18.141	114.71	30.14	102	1250	38.321×10^3
70	-16.222	115.78	32.37	99.7	1230	39.741×10^3
75	-15.835	115.68	36.26	96.7	1270	44.534×10^3
76	-14.782	116.52	36.17	95.8	1230	42.69×10^3
77	-14.89	116.28	35.6	95.6	1300	44.138×10^3
78	-12.491	118.58	34.04	94.3	1180	37.997×10^3
80	-10.382	120.01	29.14	92.0	1240	33.22×10^3
82			-65.84		1240	
75	-12.15	119.05	36.13	95.1	994	34.17×10^3
75	- 8.6966	122.13	34.72	93.6	753	24.458×10^3
75	- 4.9939	125.3	31.17	92.1	489	14.045×10^3
75	-17.794	113.7	33.57	98.2	1520	50.044×10^3
76	-19.93	110.54	31.25	98.8	1860	57.554×10^3
75	-19.727	111.46	32.21	99.2	1740	55.479×10^3
75	-18.539	112.92	33.08	98.6	1600	52.138×10^3
75	-16.448	115.15	34.55	97.6	1370	46.257×10^3
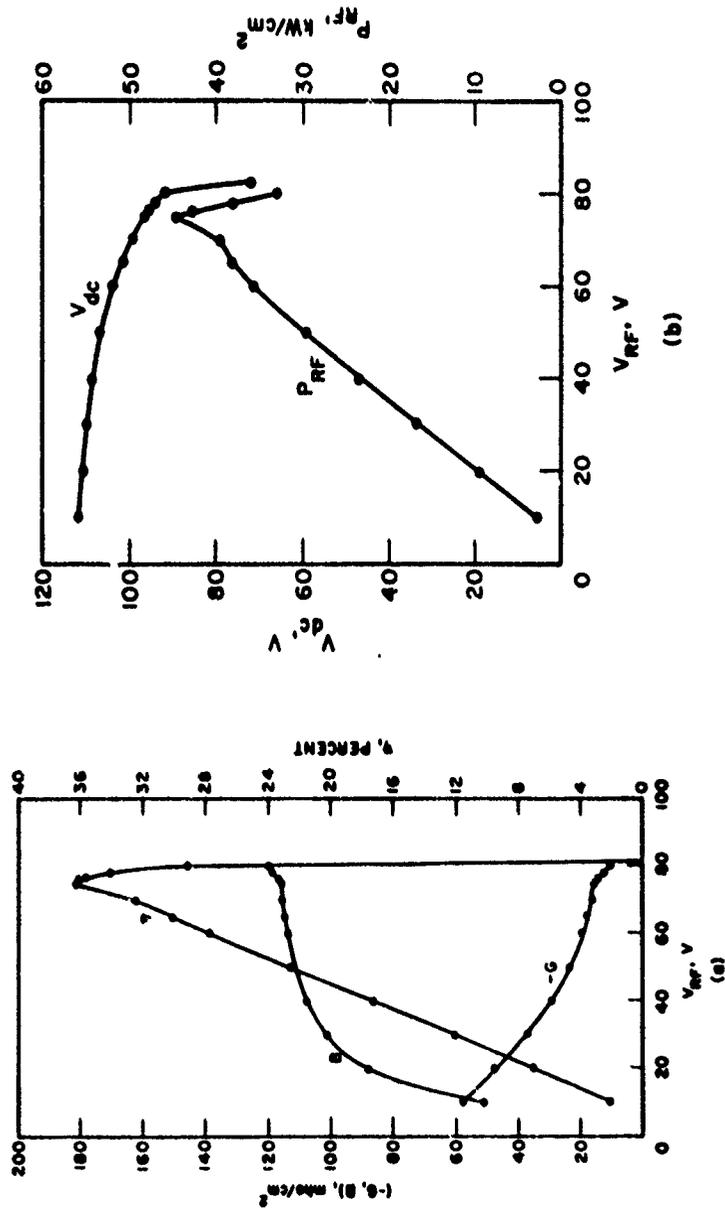
FIG. 43 LARGE-SIGNAL RESULTS FOR THE DOUBLE-READ STRUCTURE OF FIG. 42a WITH T = 500°K, f = 10 GHz AND $J_{dc} \approx 1250$ A/cm².

that the efficiency and negative conductance curves for this device are very well behaved. Figure 43b shows that the dc operating voltage decreases approximately 14 percent from $V_{RF} = 0$ to the maximum efficiency point. Figure 44 shows the computed large-signal efficiency as a function of dc current density for constant V_{RF}. It is seen that excellent efficiency is obtained over a broad range of current density. Figure 45 shows the device waveforms for the most efficient large-signal simulation with $\eta = 36.26$ percent. It is seen that the electron pulse is efficiently collected resulting in a very small current at 90 degrees in the cycle. Figure 46 shows the electric field profile and particle concentrations at two times in the cycle; Fig. 46b is just before the pulse is collected. The p-side is always punched through during the cycle due to the space charge of the generated hole pulse. The generated electron pulse is larger than the background doping, as it should be for efficient precollection. Figure 46a shows that the device is nearly drained out by the end of the cycle.

In the next structure of Fig. 47a, E_{to} was reduced to 1.8×10^5 V/cm on both sides so that the diode is not punched through on the n-side, as shown by the dc solution of Fig. 47b. Based on the hybrid simulation results, it is expected that decreasing E_{to} will decrease the efficiency of the device. The simulation results shown in Table 11 confirm that the efficiency drops from over 36 percent for the punch-through case to 26.41 percent for the nonpunch-through case. Figure 48 shows the waveforms for the $V_{RF} = 49$ V solution; the current at 90 degrees is considerably larger than for Fig. 45 because the n-side is longer and the pulse is not entirely collected
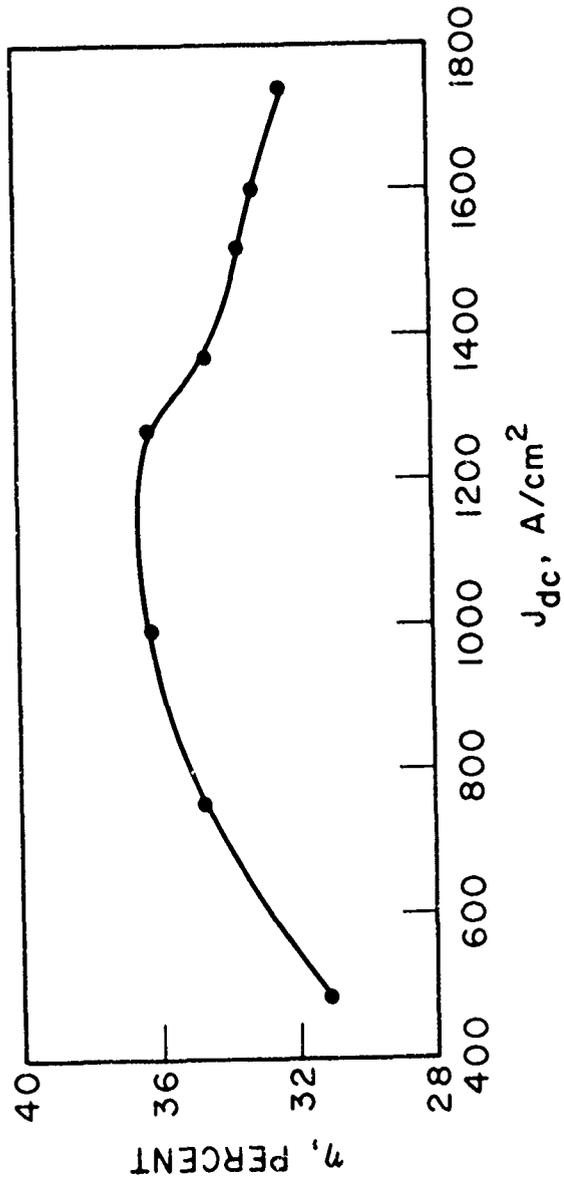
FIG. 44 EFFICIENCY AT f = 10 GHz AND V_{RF} = 75.0 V FOR DIFFERENT CURRENT DENSITIES FOR THE DOUBLE–READ STRUCTURE OF FIG. 42a.

DOUBLE DRIFT

VRF=75.

JDC=1270. A/CM**2

FREQUENCY = 10.0 GHZ
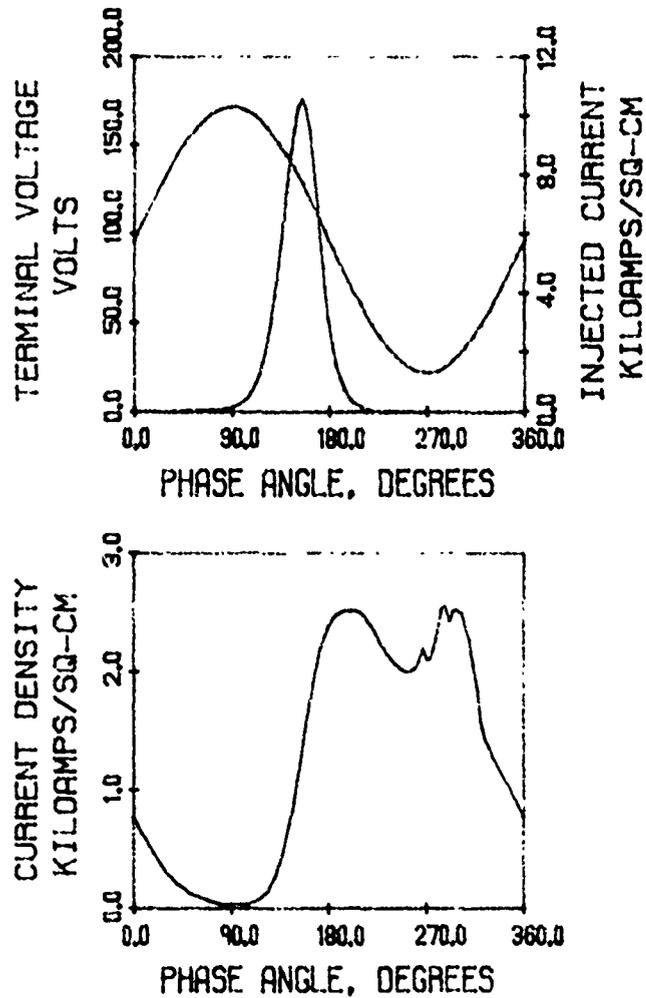
FIG. 45   LARGE-SIGNAL SOLUTION FOR THE DOUBLE-READ STRUCTURE

OF FIG. 42a WITH T = 500°K AND f = 10 GHz RESULTING

IN 36.26-PERCENT EFFICIENCY.

PHASE = 0.00 DEGREES
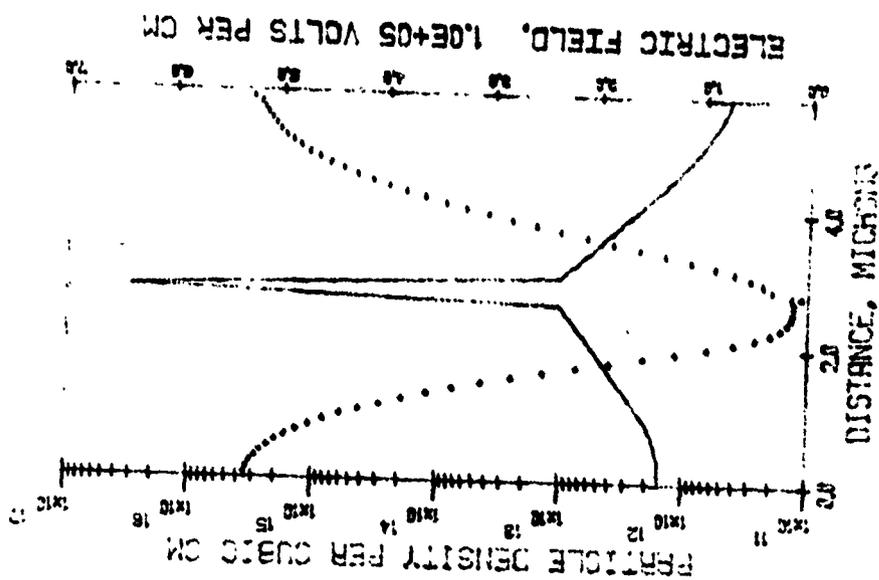
PHASE = 262.80 DEGREES
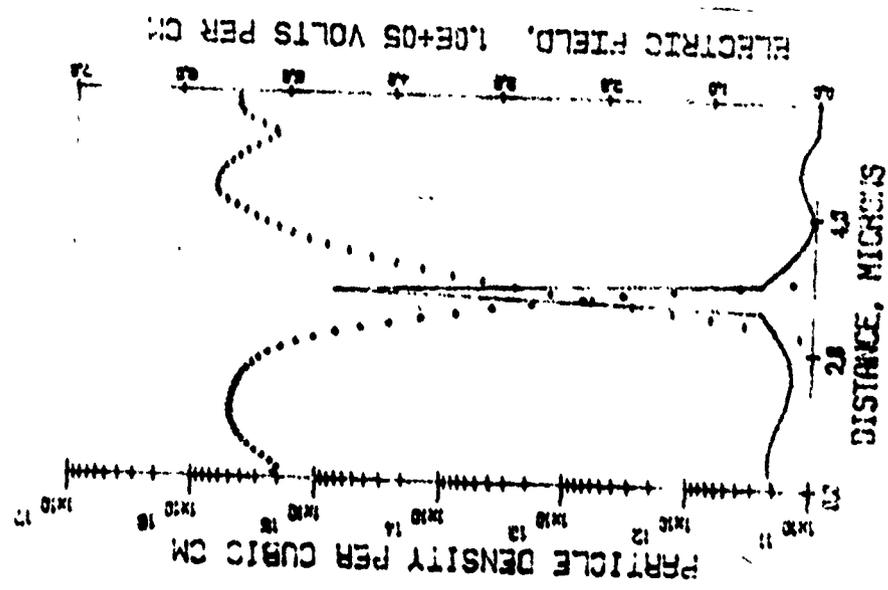
FIG. 46   DIODE STATE AT TWO DIFFERENT TIMES DURING THE LARGE-SIGNAL SOLUTION OF FIG. 45.
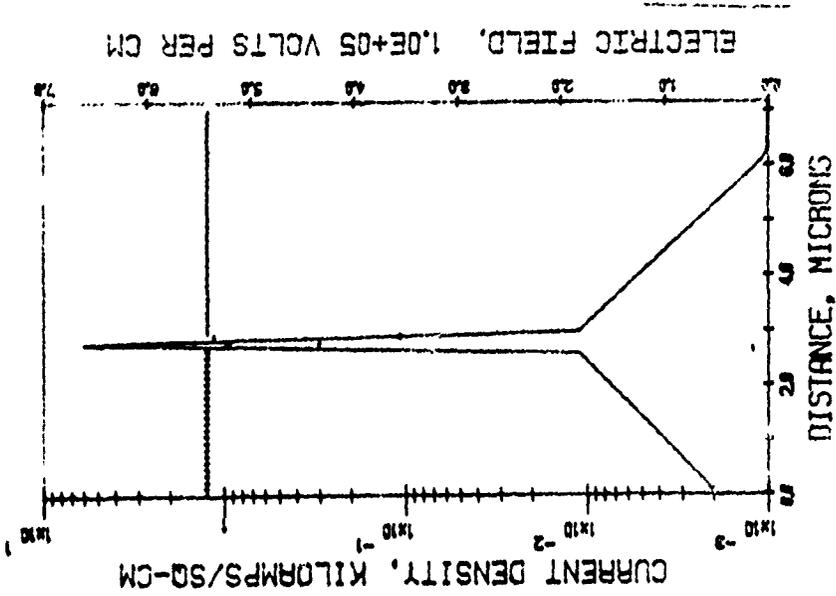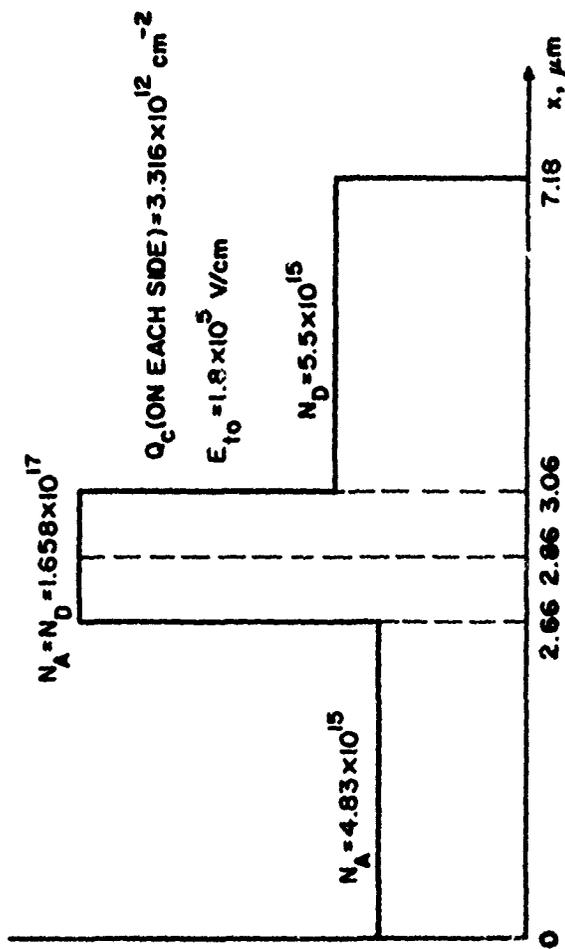
FIG. 47 (a) DOUBLE-READ DOPING PROFILE WITH REDUCED E_{to} AND (b) DC SOLUTION AT

$T = 500°K$ AND $J_{dc} = 1250$ A/cm².

Table 11

Large-Signal Results for the Double-Read Structure of Fig. 47a

at $T = 500°K$ and $f = 10$ GHz

V_{RF} (V)	G ($\mho/cm^2$)	B ($\mho/cm^2$)	η (%)	V_{dc} (V)	J_{dc} (A/cm^2)	P_{RF} (W/cm^2)
5.0	-51.758	45.874	0.68	76.5	1250	646.93
40.0	-21.252	106.38	18.67	73.9	1230	17.001×10^3
42.0	-20.527	106.7	19.68	73.8	1250	18.105×10^3
44.0	-19.544	107.64	20.58	73.6	1250	18.918×10^3
46.0	-19.233	108.85	22.46	73.6	1240	20.348×10^3
48.0	-20.151	111.04	26.02	71.7	1240	23.214×10^3
49.0	-19.637	111.48	26.41	71.6	1250	23.575×10^3
50.0	-18.808	112.12	26.45	71.6	1240	23.51×10^3

DOUBLE DRIFT

VRF=49.

JDC=1250. A/CM**2

FREQUENCY = 10.0 GHZ
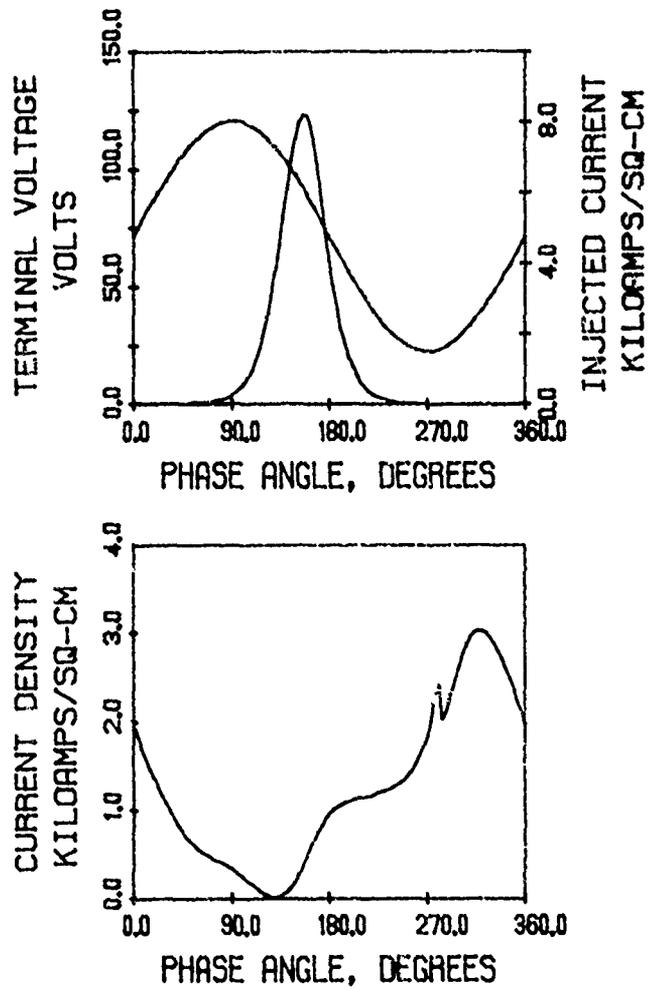
FIG. 48 LARGE-SIGNAL SOLUTION FOR THE DOUBLE-READ STRUCTURE
OF FIG. 47a WITH T = 500°K RESULTING IN 26.41-PERCENT
EFFICIENCY.

at the end of the previous cycle. Also the V_{RF}/V_{dc} ratio is smaller
than for the punch-through case which contributes to lower efficiency.
The n-region can be shortened by decreasing E_{to} further which would
reduce the current during the first half of the cycle; however, the
V_{RF}/V_{dc} ratio would also be further reduced and the efficiency would
still be well below that obtainable from the punched-through device.

5. Incorporation of Dynamic Temperature Effects in IMPATT Simulations

Up to now it has been assumed that the diode temperature
remains constant as V_{RF}, J_{dc} and f are varied in the large-signal
IMPATT simulations. This is not quite true since the diode temperature
is given by

$$T = 300 + (1 - \eta)V_{dc}J_{dc}R_{th} , \qquad (20)$$

where T is the temperature in °K, η is the fractional efficiency,
V_{dc} is the dc operating voltage, J_{dc} is the dc operating current in
A/cm^2, and R_{th} is the diode thermal resistance in $(°K-cm^2)/W$.
It is seen that as the efficiency and dc parameters of the large-
signal solution vary, the diode temperature will also change.

That this effect should be included in the IMPATT simulation
became apparent when a series of large-signal runs were carried out
at constant dc operating voltage. The structure of Fig. 21a was
previously simulated for J_{dc} varying between 900 and 1000 A/cm², as
shown in Table 6. At the maximum efficiency point, the dc operating
voltage was 61.9 V. The large-signal IMPATT program was modified to
run at constant dc voltage and this structure was again simulated for
different RF voltages but with V_{dc} = constant = 61.9 V. Therefore in
this mode of operation, J_{dc} adjusts itself to whatever value is

consistent with the given voltage drive. Table 12 shows the results obtained and Fig. 49 shows a plot of efficiency and negative conductance vs. V_{RF}. It is seen that the diode does not begin to conduct until $V_{RF} = 40$ V is reached. However all the simulations in Table 12 were run at a constant temperature of $T = 500°K$; this is obviously not consistent with Eq. 20 since below $V_{RF} = 40$ V the device is not dissipating power and should therefore be at room temperature.

At this point, the program was modified as follows. The capability of reloading the diode material parameters was incorporated. The A and b coefficients in the ionization rate expression given in Table 1 were assumed to vary linearly with temperature between the values given at 300°K and 500°K based on the results of Hall and Leck.[8] The low-field mobilities were assumed to vary as

$$\mu(T) = \mu_o (300/T)^n , \qquad (21)$$

where μ_o is the value at 300°K in Table 1, T is the temperature in °K and n is an exponent chosen so that $\mu(500°K)$ agrees with the value in Table 1. All the other material parameters in Table 1 were assumed to vary linearly with T such that the values at $T = 300°K$ and $T = 500°K$ agree with the values given in Table 1.

The algorithm may be described as follows. At the start of the simulation a material parameter temperature T_p and thermal resistance R_{th} are assumed and an RF solution is generated at T_p yielding values for η, V_{dc} and J_{dc}. T is then calculated according to Eq. 20; in general, $T \neq T_p$. At this point the material parameters are reloaded at a new temperature T'_p and a new RF solution at T'_p

-93-

Table 12

Large-Signal Results for the Diode of Fig. 21a Using a Constant

Dc Voltage of 61.9 V and T = 500°K

V_{RF} (V)	G ($\mho/cm^2$)	B ($\mho/cm^2$)	η (%)	f (GHz)	J_{dc} (A/cm²)	P_{RF} (W/cm²)
40.0	~0.0			10.0	~0.0	
45.0	− 2.255	217.49	16.35	10.0	226	2.2832x10³
47.0	− 4.1614	217.09	21.47	10.0	346	4.5962x10³
49.0	− 7.425	215.4	27.13	10.0	531	8.9136x10³
51.0	−14.861	210.0	34.80	10.0	897	19.326x10³
51.0	−17.623	196.04	38.34	9.5	966	22.919x10³
52.0	9.1273	171.55	− 4.43	10.0	4500	−12.34x10³
53.0	30.809	135.45	−11.01	10.0	6350	−43.27x10³
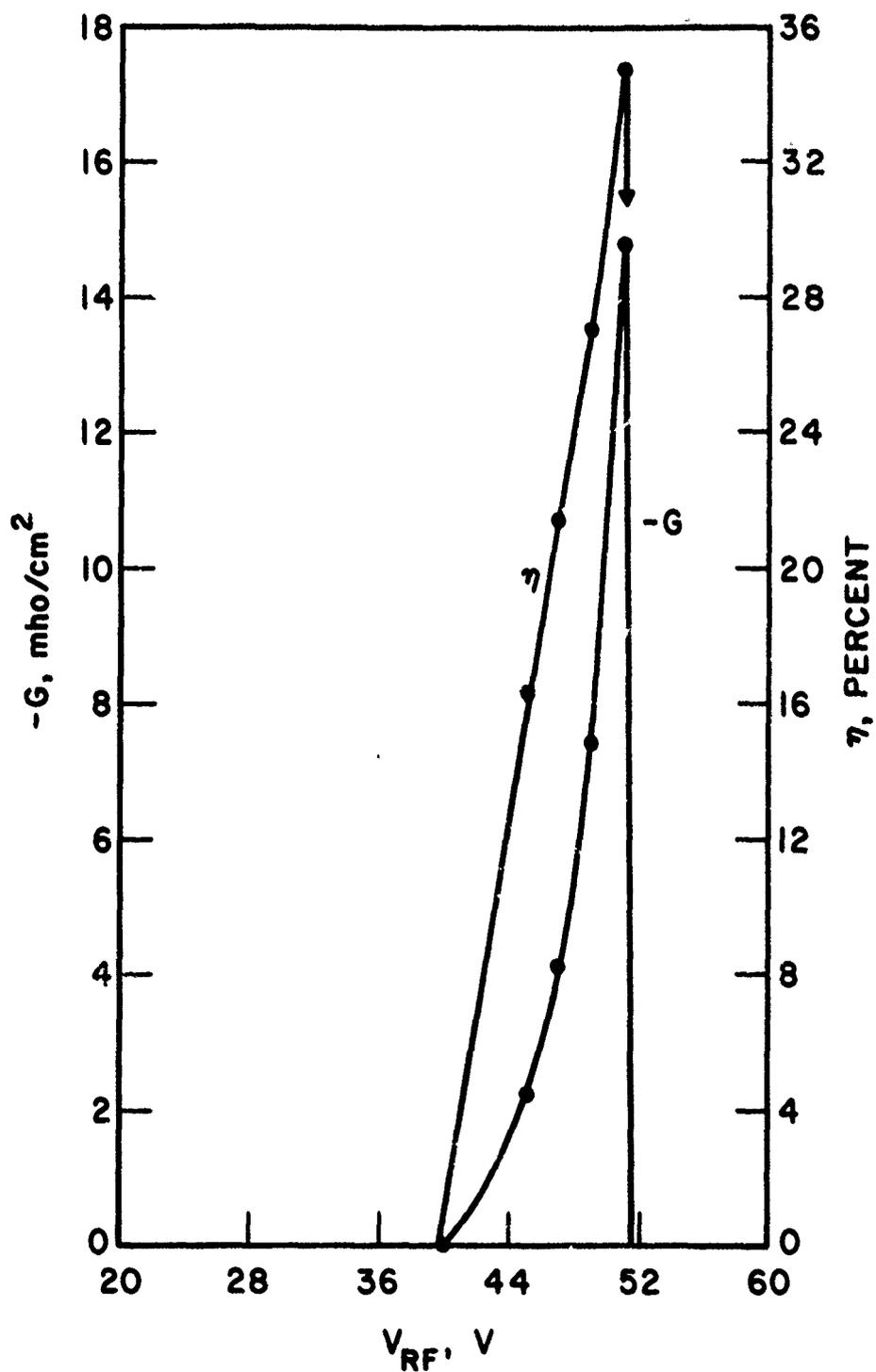
FIG. 49   LARGE-SIGNAL RESULTS FOR THE DIODE OF FIG. 21a

AT T = 500°K, f = 10 GHz AND V_{dc} = 61.9 V.

yields η', V'_{dc} and J'_{dc}. T' is calculated next as follows:

$$T' = 300 + (1 - \eta')V'_{dc}J'_{dc}R_{th} , \tag{22}$$

where in general $T' \neq T'_p$. Now from the parameter

$$\frac{\Delta T}{\Delta T_p} = \frac{T' - T}{T'_p - T_p} \tag{23}$$

a measure is obtained of how the temperature according to Eq. 20 varies as a function of device temperature T_p. If T is assumed to vary linearly with T_p, the following expression is obtained:

$$T_v(T_{pv}) = \left(\frac{T - T'}{T_p - T'_p}\right)T_{pv} + \frac{T'T_p - TT'_p}{T_p - T'_p} , \tag{24}$$

where T_v and T_{pv} are variables representing the temperature calculated according to Eq. 20 and the material parameter temperature, respectively. If Eq. 24 is set equal to T_{pv}, a new material parameter temperature T''_p is obtained which is a guess (assuming linearity in the T vs. T_p relation) of the required device temperature:

$$T''_p = \frac{TT'_p - T'T_p}{T - T' - T_p + T'_p} . \tag{25}$$

The material parameters are reloaded at T''_p and a third RF solution is calculated yielding η'', V''_{dc} and J''_{dc}. The following is then calculated:

$$T'' = 300 + (1 - \eta'')V''_{dc}J''_{dc}R_{th} . \tag{26}$$

Most of the time it is found that $T'' \cong T''_p$ to within an acceptable tolerance and the simulation is terminated. If $T'' \neq T''_p$, the process is continued until a thermally consistent solution is obtained.

For example, the structure of Fig. 15a is considered which was previously run at constant $T = 500°K$ and constant $J_{dc} \approx 1200$ A/cm^2. The best efficiency (see Table 5) was obtained for $V_{dc} = 66.1$ V and $V_{RF} = 51.9$ V. A series of simulations with constant $V_{dc} = 66.1$ V was carried out for this structure with variable temperature. The diode thermal resistance was chosen to be consistent with the optimal solution just mentioned, i.e.,

$$R_{th} = \frac{500 - 300}{(1 - \eta)V_{dc}J_{dc}} = \frac{200}{(1 - 0.3418)(66.1)(1160)} \tag{27}$$

so that the solution for $V_{RF} = 51.9$ V should yield $T = 500°K$ and $\eta = 34.18$ percent as before.

Table 13 shows the results up to the maximum efficiency point; Fig. 50 shows plots of these results at $f = 10$ GHz which show that the device heats up from approximately $450°K$ at dc to $500°K$ at maximum efficiency. These curves are in sharp contrast with those of Fig. 49 where the temperature was constant at $T = 500°K$. It is seen that entirely erroneous results may be obtained if the temperature variation is not included. From Fig. 50a it is seen that operating the diode at constant V_{dc} considerably flattens out the negative conductance curve which would be advantageous for amplifier applications. However, as shown in Fig. 50b the dc current increases very rapidly near the maximum efficiency point so that probably some sort of current limiter would be required to prevent burnout.

The structure of Fig. 15a was next simulated at constant $J_{dc} \approx 1200$ A/cm^2 but with variable temperature. The diode thermal resistance cannot be chosen consistent with the maximum efficiency

Table 13

Large-Signal Results for the Diode of Fig. 15a

with $f = 10$ GHz, $V_{dc} = 66.1$ V and

$R_{th} = 3.963 \times 10^{-3}$ ($^{\circ}$K-cm^2/W)

V_{RF} (V)	G ($\mho$/cm^2)	B ($\mho$/cm^2)	η (%)	J_{dc} (A/cm^2)	T ($^{\circ}$K)	P_{RF} (W/cm^2)
5.0	-56.895	183.1	1.76	610	457.7	0.7111x10^3
10.0	-44.336	189.92	5.24	640	456.4	2.2167x10^3
15.0	-33.617	194.95	8.93	641	456.4	3.7819x10^3
20.0	-28.13	197.0	12.63	674	455.0	5.626x10^3
25.0	-23.895	198.29	16.3	693	455.0	7.467x10^3
30.0	-21.382	198.9	19.65	741	456.5	9.622x10^3
40.0	-17.59	200.43	24.97	852	468.7	14.072x10^3
45.0	-16.938	200.96	27.62	939	477.5	17.149x10^3
48.0	-16.255	201.69	28.53	993	484.7	18.725x10^3
50.0	-16.017	202.05	29.38	1030	491.9	20.021x10^3
51.9	-19.42	199.92	34.18	1160	500.0	26.155x10^3
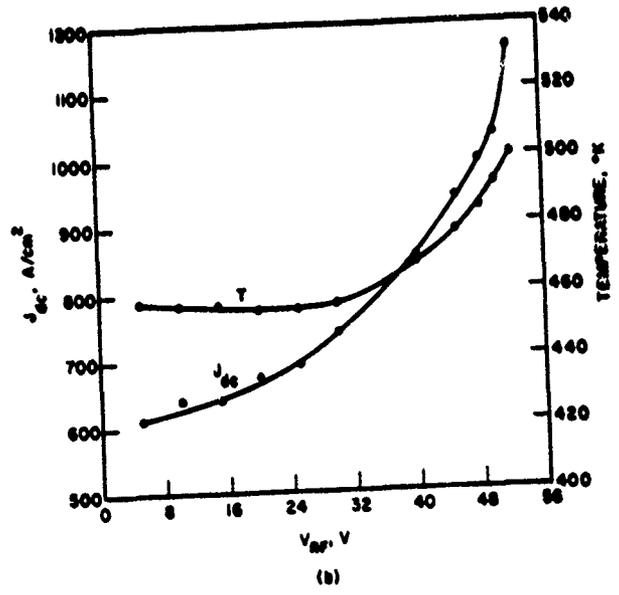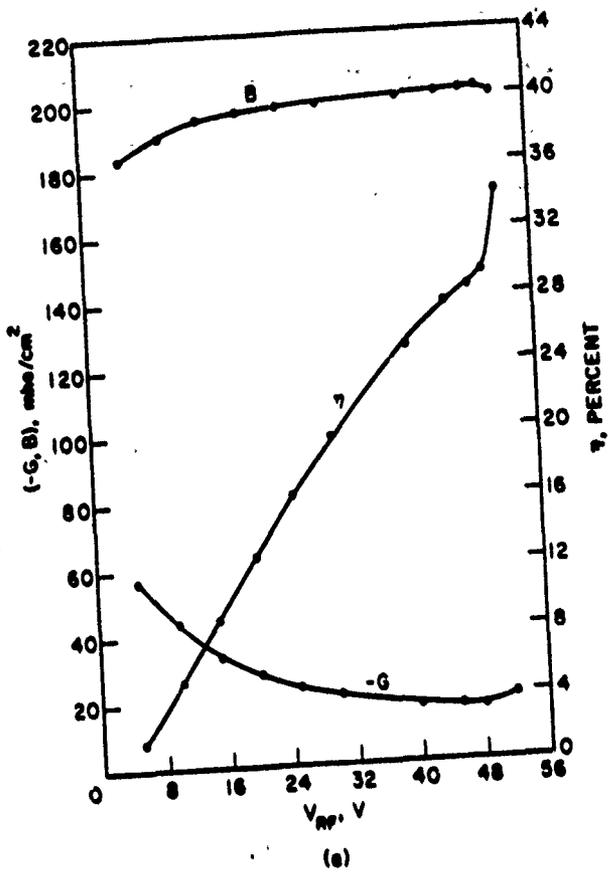
FIG. 50   LARGE-SIGNAL RESULTS FOR THE DIODE OF FIG. 15a WITH

$f = 10$ GHz, $V_{dc} = 66.1$ V AND $R_{TH} = 3.963 \times 10^{-3}$ ($^{\circ}$K-cm^2/W).

solution as before, since for constant current bias the diode heats up as V_{RF} is reduced so that it would burn out using the R_{th} for the simulations of Table 13. (The diode heats up because the efficiency in Eq. 20 decreases and there is still significant dc power flowing.) Instead, the thermal resistance was chosen consistent with the dc solution at $T = 500°K$ so that

$$R_{th} = \frac{500 - 300}{(1200)(77.36)} = 2.1544 \times 10^{-3} \ (°K\text{-}cm^2/W) \ . \qquad (28)$$

Table 14 shows the simulation results and Fig. 51 presents plots of these results. These curves should be compared with those of Fig. 17 for the same J_{dc} but constant $T = 500°K$. The maximum efficiency is approximately the same, but the efficiency curve of Fig. 51a is much better behaved than that of Fig. 17a due to the temperature variation. Figure 51b shows that the device cools down with increasing V_{RF} when constant current bias is used since the efficiency is increasing. For high-efficiency GaAs IMPATTs, it is quite important to design the thermal resistance properly. Since V_{dc} significantly increases with decreasing V_{RF} and η significantly decreases, Eq. 20 predicts that the diode can easily burn out below the optimum V_{RF} value if R_{th} is too large. For example, this diode burns out using constant current bias if the R_{th} used for the constant voltage bias case, $3.96 \times 10^{-3} \ (°K\text{-}cm^2/W)$, is used instead of $2.154 \times 10^{-3} \ (°K\text{-}cm^2/W)$.

Table 14

Large-Signal Results for the Structure of Fig. 15a

with $f = 10$ GHz, $J_{dc} \approx 1200$ A/cm^2

and $R_{th} = 2.154 \times 10^{-3}$ ($^{\circ}$K-cm^2/W)

V_{RF} (V)	G ($\mho$/cm^2)	B ($\mho$/cm^2)	n (%)	J_{dc} (A/cm^2)	V_{dc} (V)	T ($^{\circ}$K)	P_{RF} (W/cm^2)
5.0	-103.67	155.31	1.41	1190	77.2	500	1.296x10^3
10.0	- 73.839	179.59	4.11	1190	75.5	490	3.692x10^3
15.0	- 59.054	184.85	7.72	1180	72.7	473.3	6.643x10^3
20.0	- 49.955	187.52	11.51	1220	71.0	461.9	9.991x10^3
25.0	- 42.162	190.08	15.82	1200	69.1	451.9	13.175x10^3
30.0	- 37.902	189.44	21.23	1210	66.1	435.33	17.056x10^3
35.0	- 34.311	187.39	27.45	1240	61.8	417.35	21.015x10^3
36.0	- 32.99	187.25	28.94	1220	60.4	412.35	21.377x10^3
37.0	- 31.389	187.45	30.85	1180	58.9	407.35	21.486x10^3
38.0	- 32.225	185.19	33.55	1220	57.0	400.35	23.266x10^3
39.0	- 29.919	187.68	34.09	1180	56.6	400.35	22.753x10^3
40.0	- 27.738	189.83	33.49	1200	55.2	395	22.19x10^3
41.0	- 25.21	192.99	32.64	1190	54.6	395	21.188x10^3
42.0	- 22.587	196.51	30.91	1190	54.2	395	19.922x10^3
43.0	- 21.173	198.48	30.17	1190	54.7	400	19.574x10^3
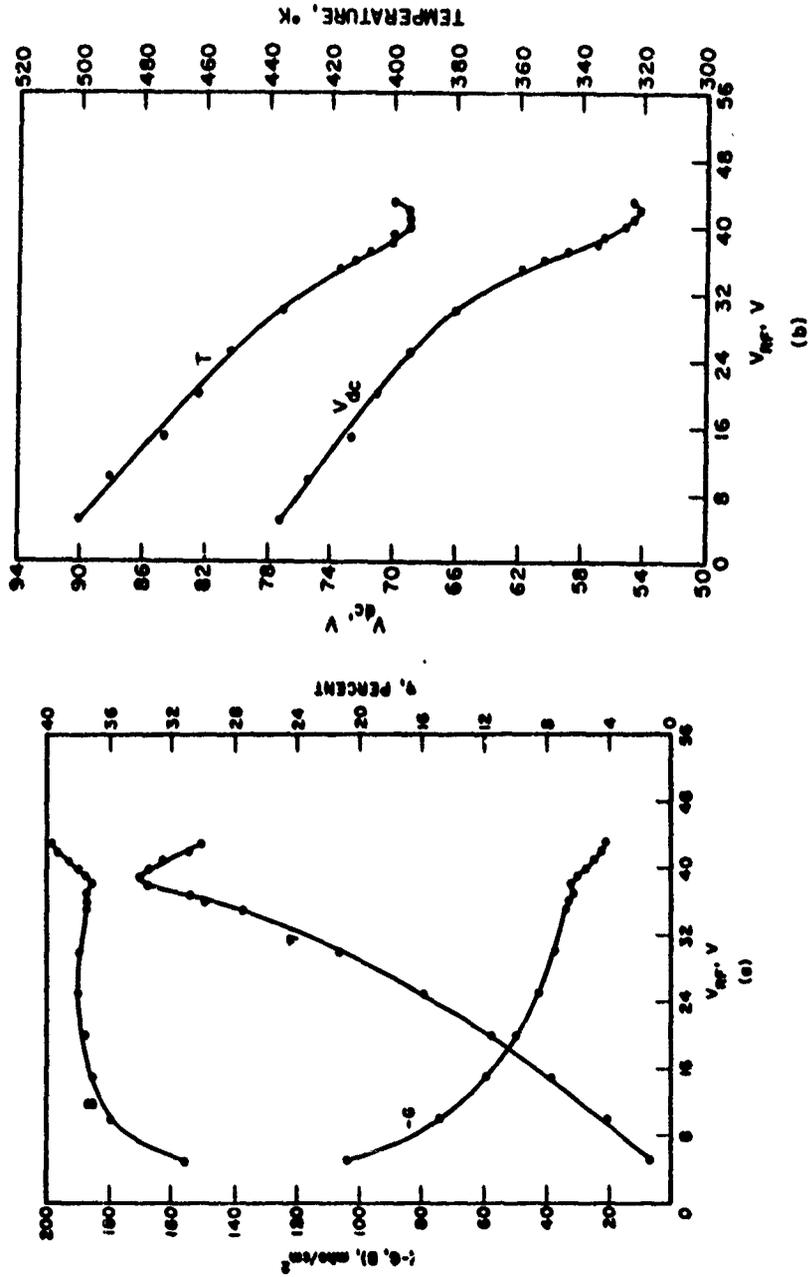
FIG. 51 LARGE-SIGNAL RESULTS FOR THE STRUCTURE OF FIG. 15a WITH f = 10 GHz, J_{dc} ≃ 1200 A/cm^2
AND R_{TH} = 2.154 x 10^{-3} (°K-cm^2/W).

6. Effects of Material Parameters

The simulations presented in this report so far have used the ionization rates determined by Hall and Leck[8] and the particle velocities from the references presented in Bauhahn's report.[6] Recently, new measurements of ionization rates and hole velocity in GaAs were published by Raytheon.[9] Table 15 shows the new material parameters based on the Raytheon results. If the ionization rate expression is evaluated and compared with the values given in Table 1, it is found that the ionization rates published by Raytheon are slightly lower than the Hall and Leck rates. For example, at $T = 300°K$, $E = 1000$ kV/cm, the Hall and Leck ionization rate is 1.478×10^5 cm^{-1}, whereas the Raytheon ionization rate is 1.202×10^5 cm^{-1}. To study the effect of the lower ionization rates, the values in Table 15 were incorporated in the simulation and a one-sided, high-low diode very similar to the structure of Fig. 6 was simulated. Previously, a maximum efficiency of 27.9 percent was obtained using the Hall and Leck rates; using the rates reported by Raytheon, a maximum efficiency of 27.25 percent was obtained. This comparison indicated that the reduction in ionization rates has a negligible effect on the calculated results.

More significant is the lower hole saturated velocity in Table 15. Of course, for one-sided diodes, incorporation of these values has negligible effect on the results. However, for double-drift diodes the length of the p-side must be reduced in order to obtain similar results. Comparison with Table 1 shows that the widths of all the p-layers simulated so far would be reduced by a factor of approximately 0.8 if Raytheon's saturated hole velocity is incorporated.

Table 15

Material Parameters for GaAs Based on Raytheon's Results

$$\alpha_n(E) = \alpha_p(E) = A \exp \left[-(b/E)^2 \right]$$

T (°K)	A (cm^{-1})	b (V/cm)	v_{psat} (cm/s)
300	1.612 x 10^5	5.42 x 10^5	8.0 x 10^6
500	1.838 x 10^5	6.47 x 10^5	5.2 x 10^6

7. Power Output from IMPATT Devices

The simulations in this report were carried out for normalized (per unit area) cases, so that absolute impedance and power levels have not been specified. In this section, achievable thermal resistances for single- and double-drift IMPATTs are used to estimate the power output from various devices already studied. It is important to note that the results presented here are at the maximum efficiency points for the various structures. Higher power outputs (i.e., under pulsed conditions) can be achieved if very short pulses are utilized and where device heating is not a problem.

Table 16 presents a summary of the cases considered in this section. In the diode type column, SD denotes single drift and DD denotes double drift; PT and NPT denote punch through and nonpunch through, respectively. DR denotes double Read and HYB denotes hybrid. For each structure, large-signal results for the maximum efficiency point are given. In Table 16, the diode area is chosen such that the negative resistance exhibited by the diode is - 1 Ω for each case; this is because we are assuming a circuit load resistance of 1 Ω which is reasonable in practice. Hence the output powers given in Table 16 are the maximum which could be achieved for this value of load resistance if the required thermal resistance can be obtained. θ_R is the required thermal resistance for CW operation so that the device temperature does not exceed 200°C.

For the one-sided, uniformly doped IMPATT structure of Fig. 4, an area of 2.73×10^{-4} cm^2 corresponds to a device negative resistance of - 1 Ω. If the external circuit can match the diode at this impedance level, the resulting CW RF power is 2.28 W and the diode

Table 16

Summary of Efficiency, Power Generation Capability and Other Parameters for Various

GaAs IMPATT Diode Structures. (f = 10 GHz)

Diode Type	G_D (℧/cm²)	B_D (℧/cm²)	A (cm²)	I_{dc} (A)	V_{dc} (V)	η (%)	P_{dc} (W)	P_{RF} (W)	P_{diss} (W)	θ_R (°C/W)	D (mils)	J_{dc} (A/cm²)
SD Uniform	-18.584	260.25	2.73×10^{-4}	0.265	55.9	15.4	14.818	2.282	12.536	15.95	7.34	971
SD HL NPT	-37.482	205.47	8.592×10^{-4}	1.1	44.0	27.9	48.4	13.5	34.9	5.73	13.02	1280
SD LHL PT	-17.44	196.24	4.493×10^{-4}	0.43	61.9	38.3	26.62	10.19	16.42	12.18	9.42	957
DD Uniform NPT	-7.238	112.88	5.657×10^{-4}	0.557	117	15.47	65.13	10.1	55.05	3.63	10.57	984
DD HYB NPT	-14.73	98.12	14.96×10^{-4}	2.20	104	18.72	228.7	42.82	185.9	1.076	17.18	1470
HYB DD Slightly PT	-17.8	106.5	1.527×10^{-3}	2.214	117.6	22.49	260.3	58.55	201.8	0.991	17.36	1450
HYB DD PT	-14.587	109.23	1.202×10^{-3}	1.754	107	27.67	187.65	51.92	135.73	1.474	15.40	1460
HYB DD Strongly PT	-11.832	111.46	9.418×10^{-4}	1.441	113	29.08	162.8	47.35	115.4	1.732	13.63	1530
DR PT	-15.835	115.68	1.162×10^{-3}	1.475	96.7	36.26	142.65	51.72	90.92	2.20	15.14	1270
DR NPT	-18.808	112.12	1.455×10^{-3}	1.804	71.6	26.45	129.2	34.17	95.03	2.105	16.94	1240

thermal resistance required for operation at 500°K is 15.95 ($^{\circ}$K/W). Examination of the thermal resistance curve in Sze[10] shows that this value of thermal resistance can be achieved.

For the one-sided, high-low, nonpunch-through diode for which large-signal results are presented in Table 2, the most efficient solution was with V_{RF} = 29.0 V, for which η = 27.9 percent. Again, matching to 1-Ω resistance, the resulting values are P_{RF} = 13.5 W (CW), A = 8.59 x 10^{-4} cm^2, R_{TH} = 5.73°K/W. According to Sze, this value of thermal resistance is reasonable.

Next, the one-sided, low-high-low, punch-through diode for which large-signal results are presented in Table 6 is considered. Going through the same procedure yields P_{RF} = 10.2 W (CW) and R_{TH} = 12.18°K/W at the most efficient point; this value of R_{TH} is reasonable according to Sze's curve. It is noted that the predicted CW power is less than for the previous high-low, nonpunch-through diode; this may counter one's expectation, since the efficiency for the punch-through diode is considerably higher. The discrepancy is explained by noting that the current density for the simulation of the nonpunch-through structure was J_{dc} = 1280 A/cm^2, while for simulation of the punch-through structure it was J_{dc} = 957 A/cm^2. If the punch-through structure were simulated at a higher J_{dc}, it would be capable of generating as much power as the nonpunch-through structure; also the R_{TH} requirement would be less stringent (higher) for the punch-through structure since the efficiency is higher (dissipated power is lower).

The simulations of Table 16 were not carried out with the goal in mind of evaluating the maximum power generating capabilities of

each structure, but rather of predicting maximum efficiencies obtainable at 10 GHz. Therefore a direct comparison of power levels is not always meaningful, as seen in the previous paragraph. The results in Table 16 do indicate the power expected for each structure under the particular conditions of the simulation.

Next, the power output from double-drift IMPATTs is considered. These diodes cannot typically be matched to $1-\Omega$ resistance because the required thermal resistance is unrealistically low for CW operation. The thermal resistance for double-drift diodes is given approximately by:[11]

$$R_{TH} = \frac{2}{\pi K_{hs} d} + R_{PKG} + \frac{4 \ell_1 T_1}{120 \pi d^2} + \frac{4 \ell_2 T_2}{300 \pi d^2} , \qquad (29)$$

where d is the device diameter in cm, K_{hs} is the thermal conductivity of the heat sink material in W/cm-^{O}K, R_{PKG} is the portion of the thermal resistance due to the package and bonding (^{O}K/W), ℓ_1 is the buffer or substrate thickness (cm), T_1 is the average temperature (^{O}K) of the buffer layer, ℓ_2 is the active layer thickness (cm) between the junction and the buffer layer, and T_2 is the average temperature (^{O}K) of the active layer.

For these calculations, the thermal conductivity of a diamond heat sink is taken as 11.7 W/cm-^{O}K and that of a copper heat sink is 3.9 W/cm-^{O}K.[11] Also, R_{PKG} is assumed to have the constant value of 2.1 ^{O}K/W.[11] It is assumed throughout that the buffer layer thickness $\ell_1 = 10^{-4}$ cm and that the average buffer layer temperature is $T_1 = 450^{O}$K. The active layer is assumed to be the p-layer and the thickness ℓ_2 is reduced by the factor 0.8 from the values specified in the figures,

consistent with the recent measurement[9] of saturated hole velocity in GaAs discussed in Section 6. The average temperature in the active layer is assumed to be $T_1 = 500^{\circ}K$.

The first term in Eq. 29 is the spreading term, which occurs at the interface between the diode and heat sink. This component of the thermal resistance can be reduced by using multiple mesa arrays or ring geometries.[12] Figure 52 illustrates the reduction of the spreading term which is possible by using a ring geometry.[11] In these calculations if a ring structure is used, it is assumed to reduce the spreading term by the factor 0.55, which is readily achievable according to Fig. 52.

For example, if the active region length $l_2 = 2.5 \times 10^{-4}$ cm is chosen, Fig. 53 presents R_{TH} as a function of device diameter for different heat sink materials and device geometries. First, the uniformly doped, nonpunch-through double-drift structure is considered for which large-signal results are given in Table 7. The most efficient solution obtained at 10 GHz is $\eta = 15.47$ percent, $V_{dc} = 117$ V and $J_{dc} = 984$ A/cm². The reduced p-layer thickness for this structure is $l_2 = 3.0 \times 10^{-4}$ cm. Since the operating temperature is $500^{\circ}K$,

$$500 \overset{\geq}{=} 300 + (1 - 0.1547)(117)(984)\pi(d^2/4)R_{TH} \quad . \qquad (30)$$

It is noted from Table 16 that if the device is matched to 1 Ω circuit resistance, a thermal resistance of $3.63^{\circ}K/W$ is required with a diode diameter of 10.57 mils; however, Fig. 53 shows that at this diameter, a thermal resistance of $3.63^{\circ}K/W$ is not achievable. To find the expected power output, Eqs. 29 and 30, which constitute two equations
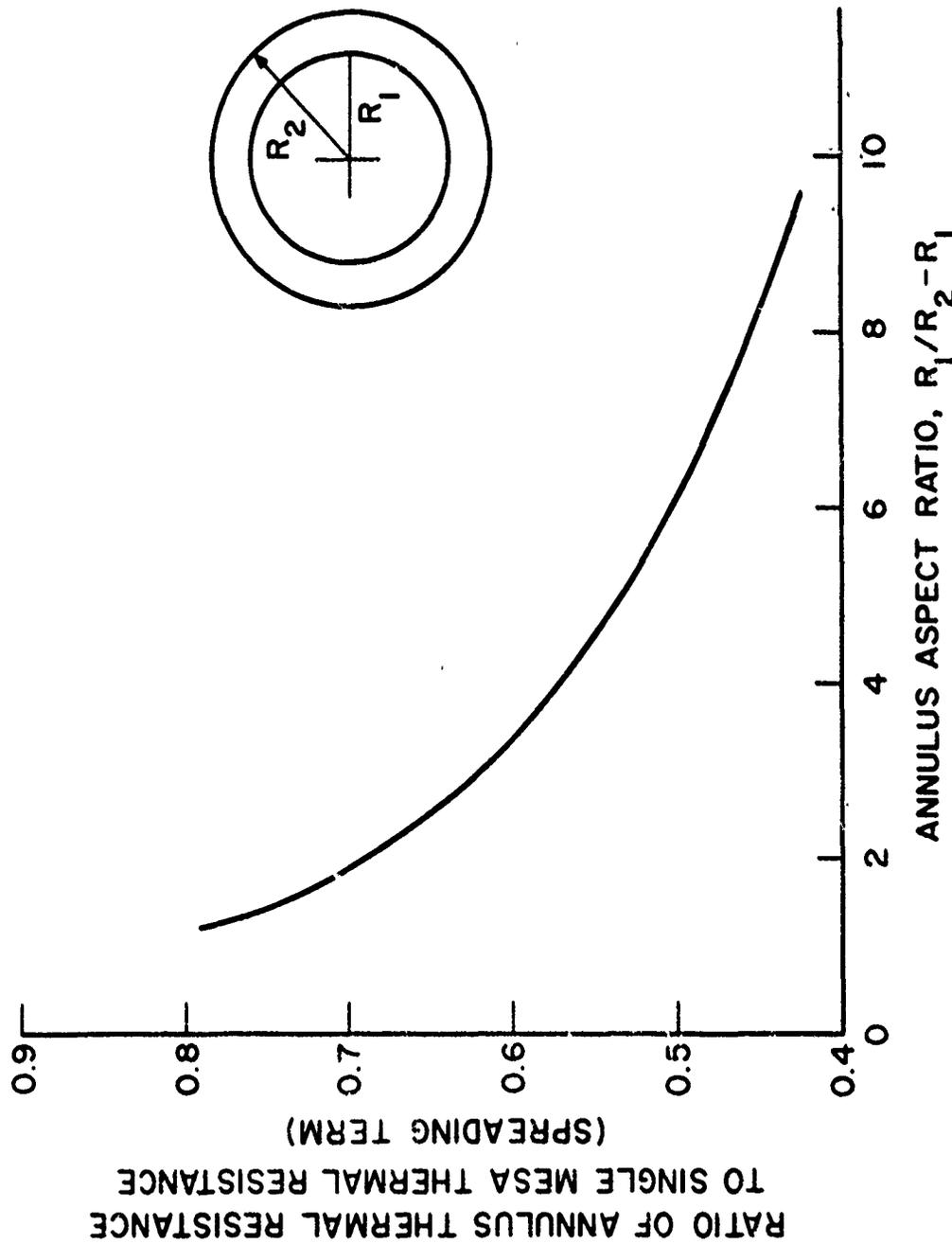
FIG. 52   THERMAL RESISTANCE RATIO OF ANNULAR MESA CONFIGURATION TO SINGLE MESA OF SAME TOTAL

AREA VS. ANNULUS ASPECT RATIO.   (FREY[12])
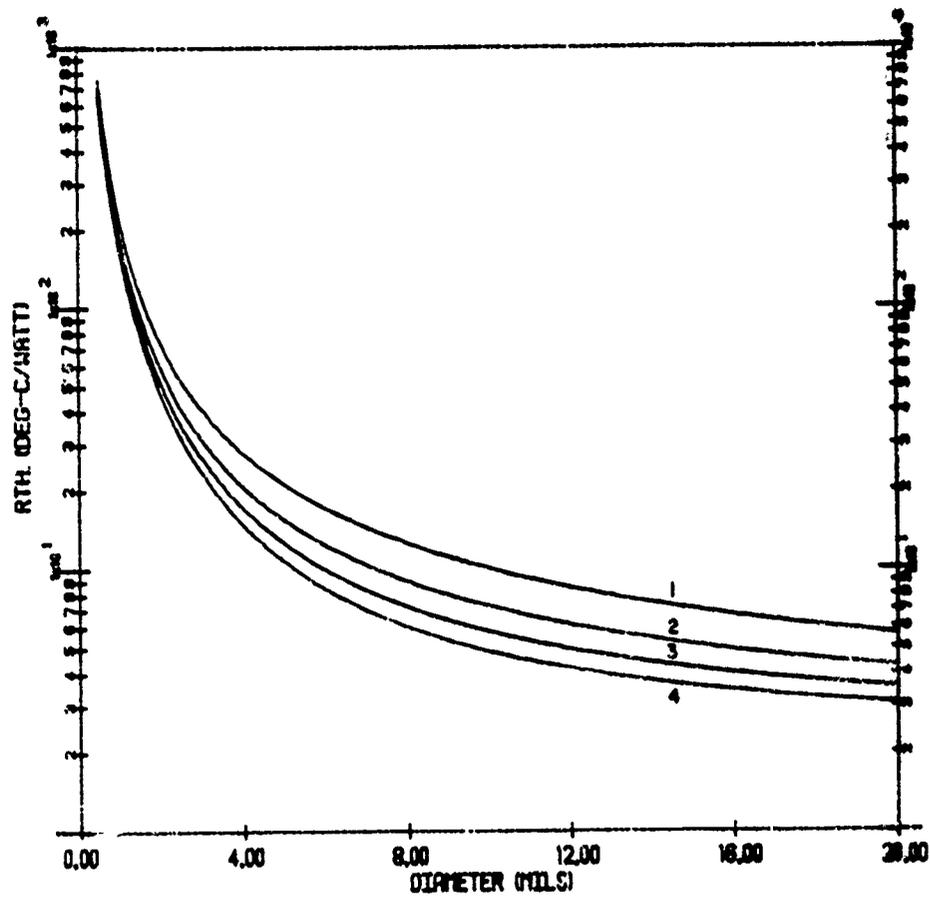
FIG. 53 R_{TH} FOR DOUBLE-DRIFT GaAs DIODES VS. DIAMETER FOR

(1) COPPER HEAT SINK, CIRCULAR GEOMETRY; (2) COPPER

HEAT SINK, RING GEOMETRY; (3) DIAMOND HEAT SINK,

CIRCULAR GEOMETRY; AND (4) DIAMOND HEAT SINK, RING

GEOMETRY. ($\ell_2 = 2.5 \times 10^{-4}$ cm AND $\ell_1 = 10^{-4}$ cm)

for the two unknowns R_{TH} and d, are solved simultaneously. The maximum expected power is obtained with the equality sign in Eq. 30.

Table 17 shows the maximum expected RF power for the double-drift structures for different heat sink materials and mesa geometries. For the uniform double-drift diode under the most favorable conditions, 5.91 W CW output power is expected, or nearly twice the power achievable with the uniform, single-drift diode.

Next, the nonpunch-through, hybrid double-drift diode of Fig. 28a is considered. The solution for this device yielded $\eta = 18.72$ percent, $V_{dc} = 104$ V, and $J_{dc} = 1470$ A/cm². The reduced p-layer thickness used in Eq. 29 is $\ell_2 = 2.4 \times 10^{-4}$ cm. The equation corresponding to Eq. 31 for this device is:

$$500 \overset{\geq}{=} 300 + (1 - 0.1872)(104)(1470)\pi(d^2/4)R_{TH} . \qquad (31)$$

Simultaneous solution of Eqs. 29 and 31 yields the maximum expected generated powers shown in Table 17.

From these results, it appears that there is hardly any advantage to using a hybrid nonpunch-through structure instead of a uniform structure. However, it is again stressed that these two structures were driven with considerably different dc current densities, and the goal was to find the maximum efficiency point rather than the maximum power point. It is quite possible that using a lower J_{dc} for the double-drift hybrid simulation would result in higher expected P_{RF}; this is explained with reference to Eq. 31. If J_{dc} is decreased by some factor and everything else remains the same, the device area could be increased by the inverse factor, which would result in the

Table 17

Maximum Power Output for Double-Drift Diodes for Different Heat Sink
Materials and Geometries. (f = 10 GHz)

Diode Type	J_{dc} (A/cm^2)	P_{RF} (W) (Copper, Circular)	P_{RF} (W) (Copper, Ring)	P_{RF} (W) (Diamond, Circular)	P_{RF} (W) (Diamond, Ring)	η (%)
DD Uniform NPT	984	0.967	2.32	3.93	5.91	15.47
DD HYB NPT	1470	0.8203	2.096	3.80	6.10	18.72
DD HYB Slightly PT	1450	0.874	2.28	4.23	6.96	22.49
DD HYB PT	1460	1.72	4.25	7.45	11.56	27.67
DD HYB Strongly PT	1530	1.51	3.84	6.94	11.08	29.08
DR PT	1270	5.18	11.33	17.8	25.0	36.26
DR NPT	1240	4.19	8.68	13.07	17.66	26.45

same P_{RF}. However in the region of Fig. 53 where R_{TH} decreases rapidly with diameter, the area could be increased much more than by the inverse factor, resulting in a greater P_{RF}. Of course, the situation is complicated by the fact that η, V_{dc}, etc., change as J_{dc} is varied. The important point is that the values given in Table 17 are not to be interpreted as the maximum possible CW power points, but rather as typical values obtained from simulations near the maximum efficiency point.

A similar procedure was carried out for three punch-through double-drift hybrid structures at different levels of punch through--the slightly punched through hybrid of Fig. 33a, for which E_{to} = 1.7 x 10^5 V/cm; the punch-through hybrid of Fig. 34a, for which E_{to} = 2.23 x 10^5 V/cm; and the strongly punch-through hybrid of Fig. 37a, with E_{to} = 2.68 x 10^5 V/cm. From the results given in Table 17, it is seen that it is advantageous to design the hybrid to be punched through. In fact, nearly twice the power of the nonpunch-through hybrid can be obtained by the punch-through hybrid.

Next, two double-Read structures were examined--the punch-through structure of Fig. 42a and the nonpunch-through structure of Fig. 47a. It is seen that the punch-through double-Read structure is capable of generating more power than any other structure considered at 10 GHz. It may be surprising to compare the generated power for the nonpunch-through double Read with that of the punch-through hybrid. The efficiencies are about equal, but the double Read can generate significantly more RF power. This is explained by noting from Table 16 that V_{dc} = 107 V for the punch-through hybrid and V_{dc} = 71.6 V for the nonpunch-through double-Read structure. Since

V_{dc} is significantly smaller for the double Read, it can operate with a larger area than the punch-through hybrid. Since R_{TH} rapidly decreases with area, the ratio of the device areas is much larger than the V_{dc} ratio; hence, the double Read can operate at higher power levels.

8. Summary and Conclusions

The properties of various types of doping profiles for both single- and double-drift GaAs IMPATT diodes operating near 10 GHz have been investigated. From the results given in Table 17, the structures may be rated as follows, in order of increasing power generating capability and efficiency: single-drift uniform nonpunch-through, single-drift Read nonpunch-through, single-drift Read punch-through, double-drift uniform nonpunch-through, double-drift hybrid nonpunch-through, double-drift hybrid punch-through, double-Read nonpunch-through, and double-Read punch-through. It is hoped that these results will provide proper guidelines for designing such devices. Tables 16 and 17 provide a summary of the power levels which can be expected from the various structures considered here.

REFERENCES

1. Blakey, P. A., Culshaw, B. and Giblin, R. A., "Efficiency Enhancement in Avalanche Diodes by Depletion-Region-Width Modulation," _Electronics Letters_, vol. 10, No. 21, pp. 435-436, 17 October 1974.

2. Kuvås, R. L. and Schroeder, W. E., "Premature Collection Mode in IMPATT Diodes," _IEEE Trans. on Electron Devices_, vol. ED-22, No. 8, pp. 549-558, August 1975.

3. Constant, E., Mircea, A., Pribetich, J. and Farrayre, A., "Effect of Transferred-Electron Velocity Modulation in High-Efficiency GaAs IMPATT Diodes," _J. Appl. Phys._, vol. 46, No. 9, pp. 3934-3940, September 1975.

4. Bauhahn, P. and Haddad, G. I., "IMPATT Device Simulation and Properties," _IEEE Trans. on Electron Devices_, vol. ED-24, No. 6, pp. 634-642, June 1977.

5. Pribetich, J., Chive, M. and Constant, E., "Design and Performances of Maximum-Efficiency Single- and Double-Drift-Region GaAs IMPATT Diodes in the 3-18-GHz Frequency Range," _J. Appl. Phys._, vol. 49, No. 11, pp. 5584-5594, November 1978.

6. Bauhahn, P. E., "Properties of Semiconductor Materials and Microwave Transit-Time Devices," Ph.D. Dissertation, The University of Michigan, 1977.

7. Blakey, P. A., Culshaw, B. and Giblin, R. A., "Criterion for the Optimum Punchthrough Factor of Gallium-Arsenide IMPATT Diodes," _Electronics Letters_, vol. 12, No. 11, pp. 284-286, 27 May 1976.

8. Hall, R. and Leck, J. H., "Temperature Dependence of Avalanche Breakdown in Gallium Arsenide P-N Junctions," _Int. J. Electronics._ vol. 25, No. 6, pp. 539-546, 1968.

9. Steele, S. R., Johnson, K. K., Lauterwasser, B. D., Bar as, A. D. and Holway, L., Jr., "P-Type Gallium Arsenide Epitaxial Growth," Tech. Report No. AFAL-TR-79-1144, Raytheon Company, Waltham, MA, October 24, 1979.

10. Sze, S. M., _Physics of Semiconductor Devices_, John Wiley and Sons, Inc., New York, p. 256, 1969.

11. Microwave Associates, Burlington, MA, Private communication.

12. Frey, J., "Multimesa Versus Annular Construction for High Average Power in Semiconductor Devices," _IEEE Trans. on Electron Devices_, vol. ED-19, No. 8, pp. 981-985, August 1972.